2009

Mineralogy and micromorphology of an Atacama Desert soil, Chile: A model for hyperarid pedogenesis

Michael S. Howell
University of Nevada Las Vegas

MINERALOGY AND MICROMORPHOLOGY OF AN ATACAMA DESERT SOIL, CHILE: A MODEL FOR HYPERARID PEDOGENESIS

by

Michael S. Howell

Bachelor of Science
Old DominionUniversity
2004

A thesis submitted in partial fulfillment
of the requirements for the

Master of Science Degree in Geoscience
Department of Geoscience
College of Sciences

Graduate College
University of Nevada, Las Vegas
August 2009

ABSTRACT

Mineralogy and Micromorphology of and Atacama Desert Soil, Chile: A Model for Hyperarid Pedogenesis

by

Michael S. Howell
Dr. Brenda Buck, Examination Committee Chair
Associate Professor of Geoscience
University of Nevada, Las Vegas

The Atacama Desert is the oldest and driest desert on Earth. Hyperarid soils in this desert are dominated by rare (or exclusive) salt minerals and assemblages. Previous research details salt origins and abundance, however pedogenic processes involved in salt distribution are not adequately explained. Therefore, the main goal of this investigation was to identify and document evidence for hyperarid pedogenesis (via salt mineralogy and soil micromorphology) at a field site, Oficina Ercilla, located ~80 km northeast of Antofagasta, Chile within the Central Depression and hyperarid core of the Atacama Desert. This study presents an interpretational model for hyperarid pedogenesis, which supports the *salt heave* hypothesis proposed by Buck et al. (2006). Hyperarid pedogenesis incorporates many known pedogenic processes (e.g. eolian deposition, clast shatter, pressure solution). However, salt heave processes dominate with a self sustaining feed-back loop initiated and perpetuated by long term influx and retention of salt minerals.

TABLE OF CONTENTS

LIST OF FIGURES

LIST OF TABLES

ACKNOWLEDGMENTS

I would first like to acknowledge financial contributions made by the Bernada E. French scholarship fund through the UNLV Geoscience department, the James P. Adams scholarship through the UNLV Graduate College, the Travel Grants through the UNLV Graduate and Professional Student Association, the GSA Graduate Research Grant through the Geological Society of America, and the AAPG Grant-in-Aid through the American Association of Petroleum Geologists. Without these monetary contributions this research project would have suffered tremendously, so I thank all of you sincerely.

To Dr. Brenda Buck, my advisor, thank you for taking me on as somewhat of a non-traditional student and allowing me to pursue a unique project that has enriched my curiosity of the natural world and improved my skills as a scientist. To my remaining committee members, Dr. Debbie Soukup, Dr. Henry Sun, and Dr. Brian Hedlund, thank you for your expertise and agreeing to be part of this project. Additionally, to my entire committee, thank you for being patient and sticking with me during my extended tenure as a Master's student, I will always remember your kind cooperation.

Many thanks to the UNLV Geoscience department faculty, students, and staff, who have made my time in this Masters program a success through all of the hard times and learning experiences. Special thanks to Dr. Rod Medcalf, Dr. Clay Crow, Dr. Andrew Hanson, and Maria Figueroa for your individual efforts that have ultimately led to the completion of this degree. To my friends, Colin Robins, Josh Boxell, Amy Brock, Jan

Morton, Carl Swenberg, and Mandy Williams, thank you for your support both directly and indirectly influential to the completion of this project. Colin, I will never forget your over-the-top hospitality and I hope to repay you somehow, if possible, in the coming years. I would also like to thank both Dr. Jason Rech and Joel Prellwitz from Miami University for their expertise and help during and after our collective trip to the Atacama Desert; along with Dr. Alex Robinson and Dr. Mike Murphy from the University of Houston for their assistance while finishing some analyses in Texas.

In closing, I would like to thank my family whose support, both loving and financial, were critical in the pursuit of this degree. I acknowledge my mother who inspired and instilled in me a need for continued education even in my youth. However, my overwhelming gratitude is extended to my wife, who has remained a pillar of support throughout this project. I know I never would have completed this without you, Kim, so I dedicate this thesis to you.

CHAPTER I

INTRODUCTION AND BACKGROUND

Introduction

Significance

The Atacama Desert of northern Chile (and southern Peru) (Figure 1.1) is both the oldest and driest desert on Earth (Ericksen, 1981; Rech et al., 2006; Clarke, 2006). Recent studies suggest that this area has been at least semi-arid since the late Triassic (>200Ma) (Clarke, 2006) or late Jurassic (150Ma) (Hartley et al., 2005). The magnitude and scale of aridity is variable, and has certainly fluctuated since the Triassic, but a large area (~50,000 mi^2/130,000 km^2) is presently experiencing hyperarid conditions in northern Chile. Moisture throughout the Atacama varies with elevation, but its driest region receives <3 mm of precipitation per year (Rech et al., 2003; Rech et al., 2006). However, this average is calculated using rare rainfall data over decades and does not imply precipitation every year. The combination of extreme and sustained aridity (hyperaridity) certifies the Atacama as the most arid end member of all existing drylands on the planet.

Drylands worldwide are becoming more degraded over time with increased desertification by climatic and/or anthropogenic forces (Dregne, 1986). These regions where globally prolific arid and semi-arid soils reside, account for an astounding 36% of (ice-free) land surfaces (Buol et al., 1997), a third of which are made up of Aridisols

Figure 1.1. Location map of the Atacama Desert (hashed area) in northern Chile and southern Peru.

specifically (Brady and Weil, 2004). Aridisols are soils formed in dry climates, therefore common in deserts. They are characterized by (1) an aridic moisture regime (dry for half the growing season, moist for less than three consecutive months), low organic matter, and one or more diagnostic pedogenic (illuvial) horizons of weatherable or soluble minerals at less than one meter depth (Brady and Weil, 2004), or (2) a salic horizon and saturation within one meter of the surface for at least one month in normal years (Soil Survey Staff, 2006). Desertification studies suggest that arid regions will become more extensive and common based on present trends in global climate and increasing population (Dregne 1986, Figure 1.2), hence increasing the considerable land area presently occupied by Aridisols. This presents an immediate concern for the public/scientists worldwide and validates the need for (improved) land management practices and continued research in arid regions.

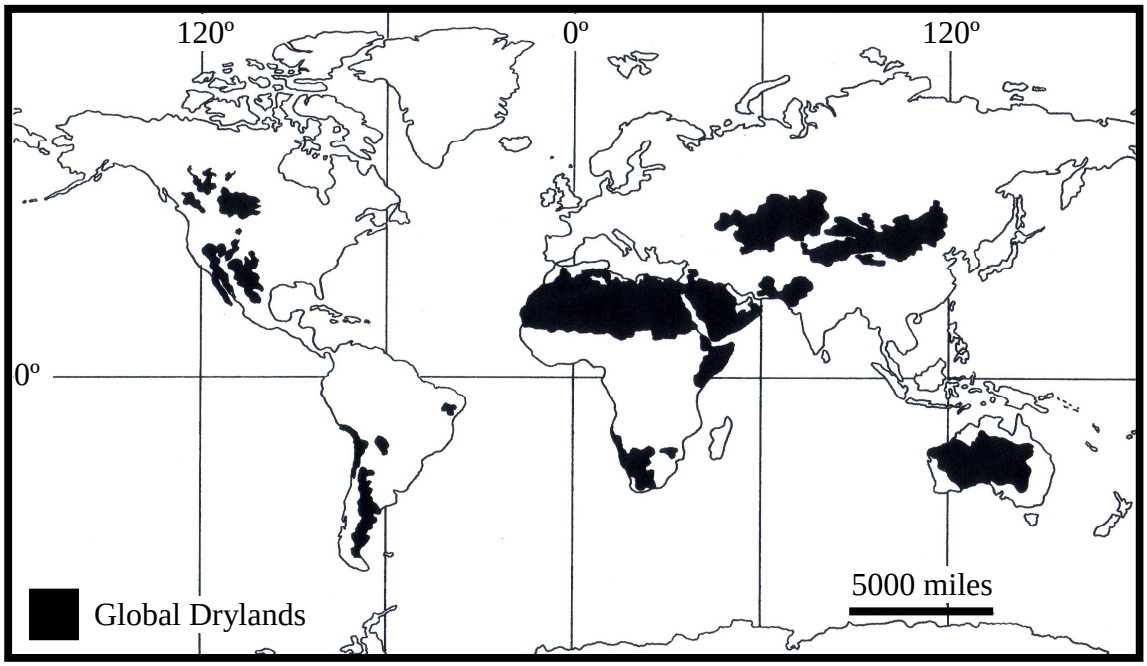

Figure 1.2. Global Desertification Vulnerability Map, gray areas are presently dry lands. (from www.usda.gov/use/worldsoils/mapindex/desert.html)

Research of Aridisols is significantly less compared to other soil orders. This is a reflection of historical objectives that have had an agricultural bias in the field of pedology. As a result, far fewer pedogenic studies have been performed in extremely arid regions around the world, and therefore, many pedogenic processes in arid environments have not been adequately researched, documented, or understood. This along with the potentially menacing desertification effects in the future stresses the need for further Aridisol studies that focus on pedogenic processes. Despite the scarcity of Aridisol investigations, noteworthy research has revealed several soil processes unique to arid regions.

One of these unique and primary soil formation processes is the accumulation of soluble minerals and/or silicate dust. Previous studies have attributed these mineral accessions to the influx of atmospheric/eolian dust (Peterson, 1980; Reheis et al., 1989;

Dan, 1990; Harden et al., 1991; Simonson, 1995; Amit and Yaalon, 1996). Dust additions are passively trapped by some form of topographic low at the soil surface, such as bar and swale surfaces or between adjacent surface clasts on alluvial fans. Precipitation events that follow, although infrequent and/or seasonal, assist accumulation by either translocating/ illuviating dust particles deeper into the soil profile (Birkeland, 1999; Brady and Weil, 2004) or creating a cohesive crust at the surface (Cooke, 1970).

The same dust accumulation processes also lead to another process and unique attribute of arid pedogenesis, the contemporaneous development of vesicular (Av) horizons and desert pavements (McFadden et al., 1987; McFadden et al., 1998; Anderson et al., 2002). These are observed in both hot and cold deserts (Claridge and Campbell, 1981). Av horizons are characterized by fine eolian sediment comprised of silt, clay, and sometimes salt, which facilitate an abundance of non-connected vesicular voids. Although the formation of vesicles is not fully understood, they are likely a result of rapid wetting / drying episodes, which preserve gas vesicles that failed to release to the atmosphere (Springer, 1958; Evenari et al., 1974, Buol et al., 1989, Anderson et al., 2002). The formation of an Av horizon begins with the formation of a desert pavement composed of surface clasts derived from subaerially exposed parent material/ bedrock (e.g. Wells et al., 1985), modified by physical weathering at the surface (McFadden et al., 1987; 1998). Surface clasts weather into smaller clasts resulting in an increased particle density and more developed surface armor or desert pavement (Cooke, 1970; McFadden et al., 1987). A laminar surface crust, composed of eolian sediment, adheres to the underside of desert pavement clasts following a precipitation event(s) (Cooke, 1970; Anderson et al., 2002). Av horizons are cumulate so as continual eolian inputs deliver

airborne dust, pedogenic modification via vesicle formation and possibly expansion/ contraction processes (depending on wind-blown materials added,e.g. salt and clay) ultimately lead to accretion (McFadden et al., 1998; Anderson et al., 2002). It is also important to note that the desert pavement stabilizes the eolian derived materials (Cooke, 1970); therefore the disruption of the desert pavement can quickly result in the eolian erosion of the Av (Quade et al., 2001; Schaetzl and Anderson, 2005). With time, this coevolution and coexistence of Av horizons and desert pavements translates into a vertically accreting soil profile where tightly packed pavement clasts are lifted as vesicular surface horizons thicken with eolian inputs of soluble minerals and silicate dust (Cooke, 1970; Yaalon and Ganor, 1973; Gile, 1975; Wells et al., 1987, 1995; McFadden et al., 1987; McFadden et al., 1992; McFadden et al., 1998; Anderson et al.,2002).

The establishment of Av horizons/desert pavements greatly affects infiltration of meteoric water (McFadden et al., 1986). As vesicular horizons thicken they often develop a pronounced platy structure as clay or other fine sediment, salt, or air in soil voids shrink-swell with rain events (McFadden et al., 1986; McFadden et al., 1987; McFadden et al., 1998). When Na^+ is present, columnar peds are formed. Columnar peds are bound by fine soil cracks that assist infiltration and at times transmit loose, single grain, eolian silt, sand, and salts into the subsurface. Water wicks into the ped interiors enriching them in illuviated clay, calcium carbonate, or other soluble minerals. Over time these mineral additions promote a continuous B horizon (McFadden et al, 1987; McFadden et al., 1998). Thickening of the Av also affects water penetration and mineral illuviation in underlying horizons. The continual addition of fine eolian material results in more surface area to retard meteoric water infiltration. This in turn leads to

decreased wetting depths that continually shallow with accreting Av horizons (Yair, 1987; Shaetzl and Anderson, 2005).

The reduced infiltration of limited/seasonal meteoric water by Av horizons/desert pavements and high evaporation rates in arid regions results in increased mineral precipitation versus leaching in soil profiles. Consequently, mineral additions illuviated from the surface or adjacent soil horizons accumulate at a maximum (albeit decreasing) depth of wetting dictated by vesicular surface horizon thickness and other local soil forming factors (i.e. climate, organic matter, relief, parent material, time). Common constituents in these illuvial soil horizons consist of clay minerals, calcium carbonate, gypsum, and other soluble salts such as halite (Gile et al, 1966; Bachman and Machette, 1977; Machette, 1985; Gile et al., 1987; McFadden et al., 1991; Harden et al., 1991; Eswaran and Zi-Tong, 1991; Amit et al., 1993; McFadden et al, 1998; Birkeland, 1999; Buck and Van Hoesen, 2002; Brady and Weil, 2004).

Over time these soluble minerals are vertically distributed throughout the profile. Mineral solubility controls the depth at which each mineral precipitates and dictates its position with respect to other soluble minerals. Horizonation is often correlative to this segregation by solubility. Additionally, the position and composition of soluble minerals in a soil profile can determine whether moisture is descending from the surface water inputs or ascending from groundwater. The most soluble minerals will migrate with the furthest reaches of meteoric water and accumulate at that depth within the soil profile (Brady and Weil, 2004; Buck et al, 2006). The exception to this general rule is overprinting as a result of a changing soil forming factor(s), which alters the depth of

wetting and permits minerals of different solubilities to occur at the same position within a profile (Harden et al., 1991).

Extended periods of aridity, and systematic translocation of soluble minerals to the maximum depth of wetting, will inevitably lead to well cemented or indurated horizons. Over geologic time spans ($10^2 – 10^6$ years), these horizons reflect specific morphologies linked (diagnostic) to the predominate indurating mineral such as calcium carbonate (Gile et al., 1966; Bachman and Machette,1977; Machette, 1985; Monger et al., 1991; Monger and Daugherty, 1991; Brock and Buck, 2009), gypsum (Harden et al., 1991; Eswaran and Zi-Tong, 1991; Buck and Van Hoesen, 2002), and halite (Amit et al., 1993; Amit and Yaalon, 1996). Since these minerals accumulate through time they can be used to interpret relative ages of geomorphic surfaces.

Other ancillary processes that contribute to arid pedogenesis are also described in these and other previous studies. Processes include thermally-induced clast shattering (McFadden et al., 2005), salt-induced clast shattering (Amit et al., 1993; Amit and Yaalon, 1996), and pressure solution (Monger and Daugherty, 1991; Brock and Buck, 2005). All of these known processes that contribute to the current understanding of arid pedogenesis, primary and ancillary, were interpreted primarily by intensive mineralogic and soil macro/micromorphologic investigative techniques. Based on their success at revealing soil processes in previous research, these techniques are also utilized in this study to elucidate processes responsible for hyperarid soil genesis in the Atacama Desert.

The Atacama Desert, as the arid/hyperarid end member of the planet, is the best natural laboratory to study pedogenesis under extreme and sustained aridity. However, research still has not adequately identified pedogenic processes that define soils in this

hyperarid desert. Identifying and documenting soil processes occurring in the Atacama Desert will provide a valuable analogue to better evaluate: (1) soil formation in the arid regions of Earth; and Mars (McKay et al., 2003), (2) paleosols in the rock record, and (3) potentially local nitrate (and other soluble salt) mining. In addition, what is learned in the Atacama Desert will help manage the global desertification problem by providing a link between what is already known about arid soil processes and how they are modified with increased and sustained aridity.

Purpose of Study

Although there have been 25+ years of research associated with the nitrate-rich soils of the Atacama Desert, no study has focused on soil processes. Therefore, the intention of this study is to understand and identify the pedogenic processes that define soils in the hyperarid core of the Atacama Desert. In order to reveal these hyperarid soil formation processes, the primary goals of this study were to: (1) select a study site representative of the oldest/most mature soil profile, (2) document geomorphic/landform attributes (3) describe and sample soil horizons/pedofeatures, (4) identify minerals and mineral assemblages with depth/horizon, (5) capture macro and microscopic verification of key and/or ancillary pedogenic processes in a hyperarid soil profile, (6) compile this information to construct a theoretical genesis model for hyperarid pedogenesis, (7) compare these processes to other known soil processes, and (8) test the hypothesis that the abundant salt minerals found in the Atacama soils provide a dominate force in hyperarid soil processes by a mechanism termed *salt heave* (Buck et al., 2006).

Background & Study Area

Geography

The Atacama Desert (Chile) is located along the western edge of South America (approximately between 18° S - 30° S, Figures 1.3 and 1.4). It is bounded along its western flank by the Pacific Ocean, which is also highlighted by the Coastal Cordillera (Cordillera de la Costa) with a maximum elevation of ~3000 m a.s.l. (Mortimer and Sarič, 1975; Ericksen, 1981). Its eastern boundary is defined by the Andes Mountains (≥5000 m a.s.l.) and adjacent front ranges (~4000 m a.s.l.) to the west of them termed the Cordillera Central (north) and Cordillera de Domeyko (south) (Mortimer and Sarič, 1975; Ericksen, 1981). Between these two ranges lies a NS trending valley (1000-2000 m a.s.l.), the Central Valley (Depression), that extends ~1000 km and can span >60 km wide. The Central Depression, also known as the Pampa del Tamarugal in the north, is segmented by the NE-SW trending transverse Baquedano Valley (Mortimer and Sarič, 1975; Ericksen, 1981, Figure 1.4), which is ~10 km wide and ~100 km long. The significant elevation, and subsequent relief, delineating the Atacama Desert provides the distinct physiography that leads to its unique and extreme climate.

Climate

The climate in the Atacama Desert is variable depending on location. Generally, it is hyperarid (<5 mm/yr precipitation) in the Central Depression, but grades into an arid region (<20 mm/yr precipitation) to the west and arid/semiarid regions (10-200 mm/yr precipitation) towards its eastern boundary with increasing elevation (Rech et al., 2003; Figure 1.5). The level of aridity in the Central Depression of the Atacama is so extreme that it approaches the limits of hyperaridity described by UNEP (United Nations

Figure 1.3. Location and approximate limits of the Chilean Atacama Desert. Antofagasta, Chile and Baquedano nitrate district (residing in the Baquedano Valley) noted for landmarks. (Satellite image courtesy of NASA / JPL-Caltech; modified using Adobe Illustrator).

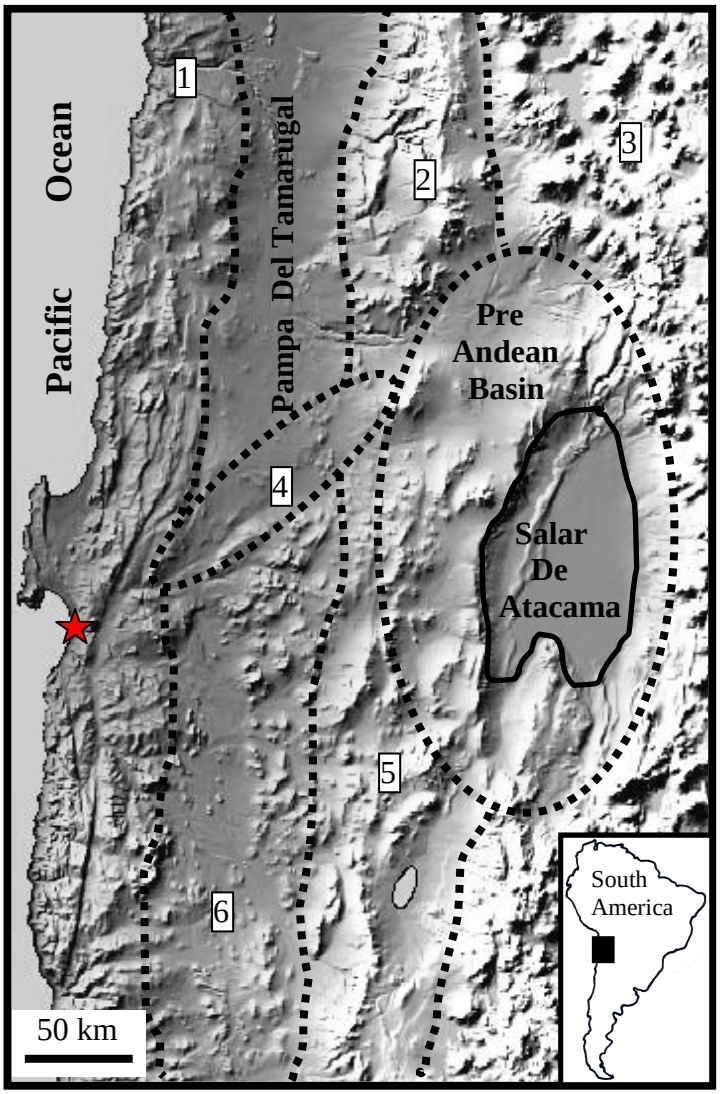

Figure 1.4. Satellite image of northern Chile near Antofagasta, Chile (red star). Dashed lines indicate approximate boundaries of: **1)** Coastal Cordillera, **2)** Cordillera Central, **3)** Andes Mountains, **4)** Baquedano Valley, **5)** Cordillera De Domeyko, and the **6)** Central Depression (Pampa Del Tamarugal in the north) as noted in the text, along with other notable landmarks. (Satellite image courtesy of NASA / JPL-Caltech; converted to black and white with Adobe Photoshop).

Environment Programme). UNEP uses a ratio called the Aridity Index (AI) to assign a numeric value to the magnitude of aridity. AI is determined using this calculation: Average Annual Precipitation/Potential Evapotranspiration (P/PET). An area must have an AI of <0.05 for hyperarid classification. Atacama precipitation satisfies this parameter with as much as 20-40 mm/yr with reported PET values of 1-2 mm/day (Mintz and Walker, 1993). Though, the hyperarid core of the Atacama Desert typically receives <3 mm/yr of precipitation (Rech, 2006; Figure 1.5), which computes to an AI of <0.01. However, this measurement is somewhat deceptive as measurable precipitation only occurs two out of every five years (Miller, 1976; Rundel et al., 1991) so this average rainfall does not imply annual rainfall. In fact, rain events in the hyperarid core often span decades (Miller, 1976; Ericksen, 1981) or centuries (Harris, 2003). Specifically, rain events of 1mm or more may only occur once every 5-20 years, with rainfall exceeding 1cm only a few times in a century (Ericksen, 1981). These low precipitation values are attributed to both the Humboldt Current and the Andean rain-shadow effect preventing moisture inputs from the Pacific Ocean and the Amazon Basin respectively (Houston and Hartley, 2003). The coastal range also acts as a barrier that prevents most of the rare moisture inputs from the Pacific Ocean and temperature inversion-induced fogs, *camanchaca*, from reaching the Central Valley (Ericksen, 1981, Rech et al., 2003). Mean temperature in the Central Depression is about 17°C (63°F), but averages 21+°C (70°+F) in its warmest month, February. The Central Depression also has a greater daily temperature fluctuation and lower relative humidity than adjacent highlands. Between July and September, diurnal temperatures can vary nearly 30°C (86°F) as night temperatures approach freezing (Ericksen, 1981). Although generally lower in the

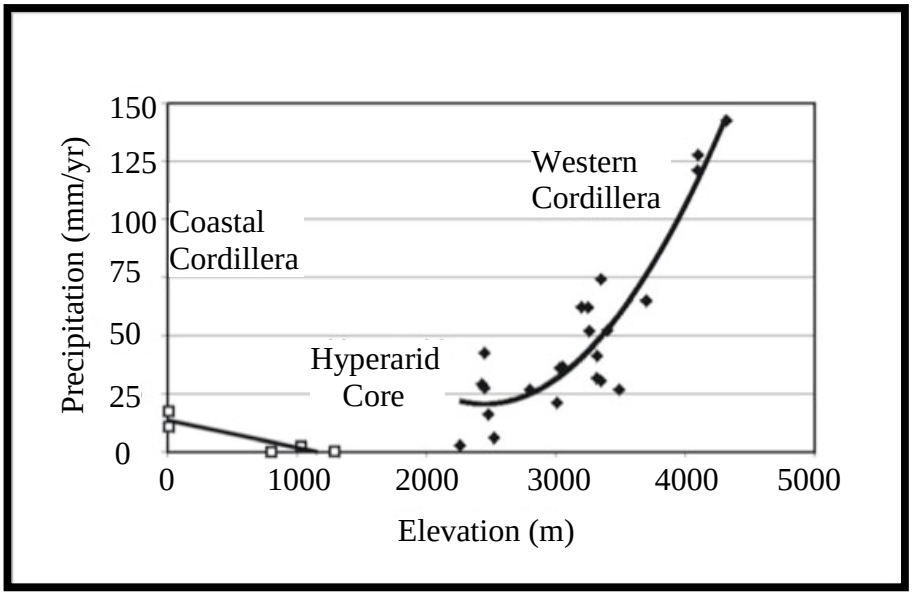

Figure 1.5. Atacama Desert precipitation vs. elevation data from west to east with geographic references. Data acquired via personal communication with Dr. Jason Rech (University of Miami, OH).

Central Depression, relative humidity (RH) measurements can fluctuate diurnally as well. Near the coast, RH values can fluctuate up to 100% (Cáceres et al., 2007). However, these findings were influenced by coastal marine fogs noted above and do not necessarily represent RH values throughout the Central Depression. Given this unique and extreme climate, the Atacama has also been studied as a possible analogue to the Martian surface (Mckay et al., 2003) along with the Dry Valleys of Antarctica (Bockheim, 2002; Sletten et al., 2003).

Vegetation

Vegetation in the Atacama Desert also differs depending on location as a reflection of climate variability. Spanish moss and hardy shrubs are found in areas near the coast that have fog moisture inputs or infrequent precipitation from the Pacific Ocean. Mesquite trees and salt grasses are also found in pampas with shallow water tables or near the

groundwater-supported salars of the Central Depression (Ericksen, 1981). However, the hostile climate of the hyperarid core incites more commonly a barren landscape as it prevents the occurrence of vascular plants (Ericksen, 1981; Rech et al.,2006) and only a limited occurrence of soil microbes (Cameron et al., 1966; Ericksen, 1981; Lester et al., 2007).

Geology

The geology of the Atacama Desert is complex due to the extensive regional history of tectonism and magmatism spanning from the Paleozoic to the present (Ramos, 1988; Padilla et al., 2001). This >500 m.y.o history has defined five distinct physiographic provinces: (West to East at Antofagasta) Coastal Range, Central Depression, Cordillera de Domeyko, Preandean Basin, and Andean Cordillera (Figure 1.6). The present hyperarid climate adds another variable to the complexity as it has been sustained over geologic time spans (Ericksen, 1981; Rech et al., 2006), and a source of error with mapping and relative dating of landforms because the extreme climate has promoted low erosion rates and little alteration of rocks emplaced/deposited throughout the Cenozoic (Mortimer et al., 1974:1975).

Evolution of northern Chile, where most of the Atacama Desert presently resides, essentially began in the Paleozoic. Initially, this western margin of Gondwana was a passive margin where continental crust met oceanic sediments. In the Mesozoic, this margin became an active subduction zone as the Nazca plate began its plunge beneath the South American plate. This initiated the formation of a magmatic arc from the Mid-Triassic to Late-Jurassic, which is presently represented by the Coastal Range province (Coastal Cordillera). The Central Depression province, along with a portion of the

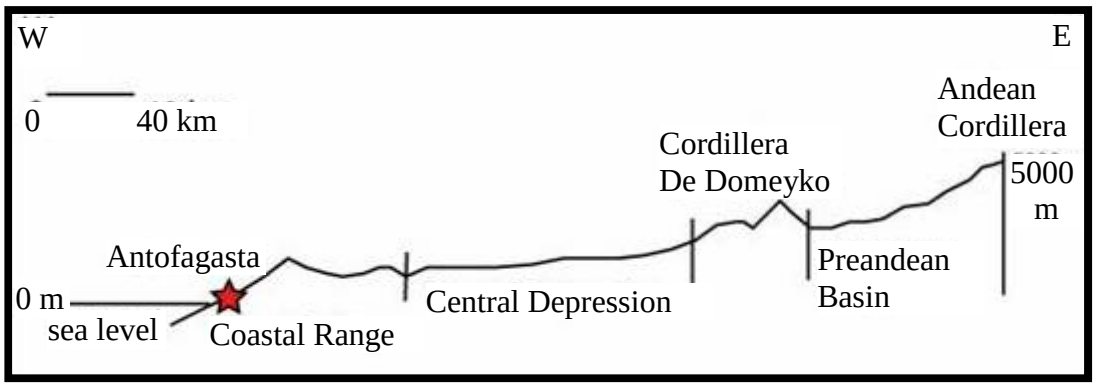

Figure 1.6. Physiographic provinces from west to east at Antofagasta (modified from Padilla et al., 2001).

Cordillera de Domeyko, represents the area that an associated extensional back-arc basin formed during this same time period. From the Cretaceous through the Cenozoic three more magmatic arcs developed. These rocks are found along the eastern margin of the Cordillera de Domeyko in a younger-eastward trend; Paleogene emplacement of intrusive bodies is also temporally/spatially associated with these magmatic arc events (Padilla et al., 2001). Transpressional and compressional tectonism, active since the Cretaceous, have consumed the back-arc basins associated with these events as extensional structures were reversed with plate movement. These regional events are also involved in the uplift of the Coastal, Central, and Andean Cordillera from Oligocene to present (Mortimer and Sarič, 1975; Ericksen, 1981, Padilla et al., 2001).

Coastal Range and Andean uplift resulted in sedimentation within the Central Depression until the mid-Miocene. Alluvial and fluvial sediments were shed from both volcanic and plutonic bedrock on eastern and western slopes (Ericksen, 1981). Volcanic rocks are dominated by andesite, dacite, and rhyolite compositions; plutonic lithologies reflect higher percentages of tonalite and granodiorite respectively (Ericksen, 1981;

Winter, 2001). The sediments derived from these rocks are generally lumped into what is called the Rhyolite Formation (Mortimer et al., 1974) in the Pampa del Tamarugal (Figure 1.4), but the extensive alluvial fan deposits throughout the Central Depression are sometimes referred to as "Atacama gravels" (Nishiizumi et al., 2005). The uplift on both flanks of the Central Depression is not only the catalyst for the deposition of these sediments. It is also a major contributor in the transition to the present hyperarid climate.

Hyperaridity

The age of onset of hyperaridity in the Central Depression is still controversial. Several studies have inferred age ranges from late-Oligocene to late-Pliocene. Cosmogenic ^{21}Ne dating of surface clasts in northern Chile suggests hyperaridity has been sustained since 25 Ma (Dunai et al., 2005). Rech et al. (2006) infer an Early to Mid-Miocene (19-13 Ma) inception based on stratigraphic relationships of paleosols with dated ignimbrites (9.4-8.3 Ma). Alpers and Brimhall (1988) have also proposed a Mid-Miocene (15-13 Ma) age using K-Ar dating techniques of hydrothermal minerals in conjunction with dated volcanic ash-bed markers in soil profiles. A Late-Pliocene age was reported using Miocene to Pliocene sedimentation data (Hartley and Chong, 2002). Cosmogenic dating (^{10}Be) was also employed by Nishiizumi et al. (2005), which supported a Late-Pliocene commencement of hyperaridity. Despite the wide array of ages, the antiquity of aridity (even if only 3-4 Ma) is evident and has provided a unique setting where eolian processes have dominated over alluvial/fluvial processes for a significant amount of geologic time.

Arid Processes and Geomorphology

The sustained hyperarid regime has permitted only minimal physical and chemical

weathering of bedrock and the sediments shed from them. Landforms in the Central Depression reflect only minor alteration since the initiation of hyperaridity (Ericksen, 1981). Recent studies that have addressed erosion rates suggest that alluvial surfaces are actually more stable than bedrock ridges (Nishiizumi et al., 2005). This has allowed excellent geologic preservation along with a unique mineralogical retention in these lower surfaces since the Miocene (Mortimer et al., 1974; Ericksen, 1981).

Eolian processes have played a major role in rounding the landscape as wind-transported dust and sediment round/fill any remnant hills, gullys, and valleys produced from a previous wetter climate (Ericksen, 1981). As a result the landscape has undergone substantial volumetric expansion (Ewing et al., 2006) as an unparalleled amount of silicate dust and high concentrations of soluble minerals including nitrates, sulfates, chlorides, iodates, and perchlorates have been preserved in soils and bedrock (Ericksen, 1981). The limited precipitation and fluvial processes combined with this extensive eolian/atmospheric deposition has resulted in a retention/surplus of dust/soluble minerals unmatched in other arid regions. Geomorphically, this translates into a landscape of smoothed topography with gently sloping alluvial fans, pampas, playas, and minimal stream incisions or terracing (Ericksen, 1981).

Soils

Soils forming on these geomorphic surfaces have accumulated some of the richest deposits of salt in the world. The largest accumulation of nitrate along with exclusive salt species and salt mineral assemblages are globally recognized as well (Ericksen, 1981, Figure 1.7). Soil profiles in the Central Depression are reported to have an average of 26-40% salt, with single horizons containing >99% (Buck et al., 2006; Prellwitz, 2007).

HALIDES:
- Halite, $NaCl$

NITRATES:
- Soda niter (Nitratine), $NaNO_3$
- Niter, KNO_3
- Darapskite, $Na_3(SO_4)(NO_3) * H_2O$
- Humberstonite, $K_3Na_7Mg_2(SO_4)_6(NO_3)_2 * 6H_2O$

IODATES AND CHROMATES:
- Lautarite, $Ca(IO_3)_2$
- Brüggenite, $Ca(IO_3)_2 * H_2O$
- Dietzeite, $Ca_2(IO_3)_2(CrO_4)$
- Tarapacaite, K_2CrO_4
- Lopezite, $K_2Cr_2O_7$

BORATES:
- Ulexite, $NaCaB_5O_9 * H_2O$
- Probertite, $NaCaB_5O_9 * 5H_2O$
- Ginorite, $Ca_2B_{14}O_{23} * 8H_2O$
- Hydroboracite, $CaMgB_6O_{11} * 6H_2O$
- Kaliborite, $HKMg_2B_{12}O_{16}(OH)_{10} * 4H_2O$

SULFATES:
- Thenardite, Na_2SO_4
- Glauberite, $Na_2Ca(SO_4)_2$
- Bloedite, $Na_2Mg(SO_4)_2 * 4H_2O$
- Kieserite, $MgSO_4 * H_2O$
- Epsomite, $MgSO_4 * 7H_2O$
- Gypsum, $CaSO_4 * 2H_2O$
- Anhydrite, $CaSO_4$
- Bassanite, $2CaSO_4 * H_2O$

Figure 1.7. Summary of saline minerals found in Chilean nitrate deposits (from Ericksen, 1981).

These salts are attributed to atmospheric (Ericksen, 1981;Böhlke et al. 1997; Michalski et al., 2004; Oyarzun and Oyarzun 2007), eolian (Ericksen, 1981; Rech et al., 2003; Bao et al., 2004; Bao 2005), and groundwater origins (Ericksen, 1981). As a result of interest in the nature and source of the saline minerals, research has increased significantly over the past 25+ years.

Many historic studies have offered insight into the primary origins of these indurating salt minerals. Ericksen (1981, 1983) summarized previous theories for possible sources

of nitrate and other saline constituents. Proposed nitrate sources include (1) decomposed vegetation from cutoff inland arms of the sea (Forbes, 1861; Noellner, 1867; Flagg, 1874; Müntz, 1887; Müntz and Marcano, 1885) or continental saline lakes (Sieveking, 1887), (2) nitrification and leaching of seabird guano near saline lakes (J.C. Hillinger, 1860), inland arms of the sea (Penrose, 1910), and salars (Gautier, 1894), or windblown ammoniacal particulate matter and gas from guano deposits (Ochsenius, 1887-88, 1888, 1903; Brüggen, 1928, 1938), (3) decay of land plant and animal remains (Plagemann, 1897-98) or plant materials in soils (Newton, 1896), (4) nitrification and fixation of atmospheric nitrogen by soil bacteria (Gale, 1912, 1917; Brüggen, 1938), (5) atmospheric nitric acid reactions with igneous rocks (Pissis, 1878; Sundt, 1904, 1911, 1917, 1921; Wetzel, 1924, 1926, 1928, 1932, 1961; Knoche, 1930, 1939), (6) accumulations from volcanic gases or leaching of volcanic rocks (de Kalb, 1916; Feista, 1922, 1966; Steinman, 1925; Whitehead, 1920; Ericksen, 1961), or accumulation of nitrate from various sources in subsurface saline waters / brines associated with salars (Singewald and Miller, 1916; Mueller, 1960, 1968) or in soils (Hofseth, 1931; Claridge and Campbell, 1968; Ericksen, 1975, 1979). Sources of saline minerals other than nitrate include (1) evaporation of shallow marginal waters and windblown spray associated with inland arms of the sea (Darwin, 1890), (2) capillary migration from subsurface water / brine from salars into soil and fractured bedrock (Miller, 1916; Mueller, 1960), (3) atmospheric fallout/washout along with subsequent reactions of atmospheric inputs with soils (Pissis, 1878), (4) accumulation from saline-rich mudflows (Wetzel, 1924, 1926, 1928, 1932, 1961), and (5) volcanic emanations or soluble minerals within volcanic rocks (Ericksen, 1961, 1981) This composite list verifies the immense scientific interest and

wealth of ideas regarding the origin of these anomalous salt deposits over the past two centuries. However, principal sources are generally accepted to be (1) sea spray/aerosols from the Pacific Ocean, (2) volcanic rocks and emanations of Andean volcanoes, (3) photochemical reactions in the atmosphere, (4) eolian transported salt minerals eroded from saline soils, evaporite deposits, and salars in the Atacama Desert, and (5) reactions/transformation of soils/rocks with atmospheric ions (wet and dry deposition) or soil microorganisms (Ericksen, 1981).

One or more of these origins contribute to the prevalence of each of the salts or saline groups (i.e. Nitrates, Halides, Sulfates, Iodates, Borates, and Chromates) in the Chilean nitrate deposits (Figure 1.7). Recent studies using O isotopes suggest that the bulk of the nitrate salts are accumulated from dry deposition as a result of tropospheric and stratospheric photochemical reactions (Böhlke et al., 1997; Michalski et al., 2004). Oyarzun and Oyarzun (2007) believe that atmospheric fixation induced by large scale volcanic activity during the late Miocene explains the abundance of nitrate. These studies support the conclusions in Ericksen (1981), but Ericksen (1981) also suggests nitrate formation via oxidation of ammonia and nitrogeneous organic materials derived from Pacific Ocean sea spray. Nitrate may also have been formed in soils via nitrification of ammonia/ammonium or nitrogen fixation by photoautotrophic bacteria and blue-green algae (Ericksen, 1981).

Origins for halogens including chlorides, perchlorates, iodates, and bromides have also been linked to composite sources. Chloride represented solely by the mineral halite is largely attributed to sea spray from the Pacific Ocean. However, it is also supplied by volcanic emanations or groundwater fed salars associated with the nearby Andes and

Andean groundwater (Ericksen, 1981). The anamolous amount of perchlorate (albeit trace amounts) found in the Atacama Desert soils has entrigued scientists for decades. Reactions between chlorine gas and ozone in the troposphere and at the soil surface have previously been suggested for the creation of perchlorate in the Atacama (Ericksen, 1981; Ericksen, 2004; Orris, 2005). Recent studies in the arid southwestern US (Texas and New Mexico) also support perchlorate enrichment in soils and groundwater via atmospheric deposition (Rajagopalan et al., 2006; Plummer et al., 2006). Iodates (lauterite and brüggenite) are attributed to oxidation of iodine via photochemical reactions in the troposphere and at the soil surface. Iodine is supplied by organic material transported in sea spray or from gaseous iodine formed by photochemical oxidation of iodide at the surface of the Pacific Ocean (Ericksen, 1981). The presence of bromides are likely the result of marine aerosols as well. However, unlike iodide photochemical oxidation of bromide results in a gaseous form of bromine which is subsequently lost to the atmosphere and leads to anomalously low bromine content in the Atacama Desert and a lack of salt minerals containing bromine (Ericksen, 1981, Figure 1.7).

Sulfate salts (i.e. gypsum, bassanite, anhydrite, thenardite, glauberite, bloedite, kieserite, epsomite, Figure 1.7) are abundant throughout the nitrate deposits, which along with nitrate and halite dominate saline constituents (Ericksen, 1981). Rech et al. (2003) offer a composite model of both marine fogs and eolian salar materials as sulfate salt sources based on S and Sr isotope analyses. Bao et al. (2004) and Bao (2005) use O isotopes to conclude that dry fog inputs are a significant source of sulfates in inland zones; these sulfates are linked to oxidized sulfur gases that are attributed to biological emissions from the Pacific Ocean or gaseous emissions from volcanism. These studies

support Ericksen's (1981) conclusions of seawater and volcanic origins, but Ericksen (1963, 1981) also suggests that additional sulfate may be derived from soluble sulfate minerals leached from volcanic rocks subsequently reworked via eolian processes and/or Andean groundwater.

Borates, largely represented by the mineral ulexite, are primarily attributed to volcanic origins. This is evidenced by abundant ulexite in salars in the Andean highlands, where saline minerals are derived from volcanic emissions and hot springs along with leached volcanic rocks nearby (Ericksen, 1981). Furthermore, salars at lower elevations within the Atacama Desert are enriched locally with ulexite by Andean drainage (Ericksen, 1963).

Chromate and dichromate salts (dietzeite, tarapacaite, and lopezite, Figure 1.7) occur in trace amounts within the nitrate deposits. The presence of chromate is likely due to chromium present in sedimentary rocks (shales) near the deposits (Krauskopf, 1967; Connor and Shacklette, 1975; Ericksen, 1981). Trivalent chromium found in these shales may have oxidized to hexavalent chromium leading to the formation of the mobile chromate ion (Rankama and Sahama, 1950; Ericksen, 1981). Some soil chromate may also be formed from the decay of organic matter in sea spray or terrestrial plants (Ericksen, 1981). The presence of iodate in dietzeite is also suggestive of sea spray influences. The formation of dichromate is caused by the subsequent alteration of chromate, which was observed in vugs of chromate-rich nitrate ore (Ericksen, 1981).

Cations (i.e. sodium, potassium, calcium, and magnesium) available to form salt compounds have also been attributed to similar origins as the anions (i.e. nitrate, chloride, sulfate, etc.) present in the nitrate deposits. These alkali and alkaline-earth elements are

derived from sea spray, airborne Andean volcanic particulates, and eolian transported dust from saline soils, salars, and playas within the Atacama Desert (Ericksen, 1981).

With the exception of perchlorate, many of the salt minerals (or their ionic components, Figure 1.7) discussed are found worldwide terrestrially or in the atmosphere, however the unique hyperarid environment has allowed for their anomalously abundant deposition and retention (Ericksen, 1981; Ewing et al., 2006). The almost rainless climate since the mid Miocene (Ericksen, 1981; Rech et al., 2006) has caused a long term accumulation throughout the Atacama Desert (Ericksen, 1981; Buck et al., 2006; Ewing et al., 2006). Eolian processes that have effectively rounded the landscape have redistributed dissolved/leached soluble salts, previously destabilized and/or mobilized by sporadic and sometimes heavy rain events. Subsequently, the salts were redeposited on ancient flat, shallow sloped, or gently undulating land surfaces such as alluvial fans, where later precipitation dissolved and translocated them below the surface. Over geologic time scales this has enriched soils forming on these geomorphic surfaces with airborne soluble salts, or soluble ions that have reacted in soils to form salt, to levels unmatched elsewhere on Earth (Ericksen, 1981).

Previous investigations have also recognized/documented relationships between soil horizons and the salt mineralogy. Ericksen (1981, 1983) loosely describes soil horizonation using 5 locally termed soil layers: chuca, costra, caliche, conjelo, and coba. The chuca is approximately 30 cm thick and composed of unconsolidated surface horizons, which includes a basal friable thenardite and/or humberstonite layer if present. Below the chuca lies the costra layer. It is usually 0.5-2 m thick, but unlike the chuca it is moderately to firmly cemented by saline minerals. Firmly cemented nitrate ore, caliche,

with thicknesses of 1-3 m rests beneath the costra. The caliche can also contain veins or basal layers of a white nitrate-rich material called caliche blanco. Depending on the location, the caliche may grade into conjelo or coba. The conjelo is a firmly cemented layer, capable of thicknesses of 2 meters or more, with lesser amounts of nitrate than the caliche. Coba is simply unconsolidated alluvial parent material (Ericksen, 1981). Ericksen (1981, 1983) also describes features termed *sand dikes* and *dessication polygons.* However, a pedogenic process (es) linking the mineralogy to soil horizonation and these surface/subsurface elements is not presented.

Salt Heave

Salt heave is a recently proposed pedogenic process that provides a viable mechanism to explain the unique attributes of these Atacama soils. Salt heave is caused by: (1) precipitation/dissolution (enhanced by hydration/dehydration), and (2) differential thermal expansion/contraction of salt minerals (Buck et al., 2006). These salt properties incite volumetric changes in soil materials that occur daily, (possibly diurnally), or with infrequent precipitation events (Buck et al., 2006). Buck et al., (2006) hypothesizes that unusually high concentrations of salt minerals in the Central Depression enhance these volumetric fluctuations into a physical heaving mechanism and dominate pedogenic process. Over extended periods of time ($10^3 – 10^{6+}$ years), salt heave is also thought to be responsible for the trans-horizon cracks that form patterned ground (Buck et al., 2006) previously described as *sand dikes* and *desiccation polygons* by Ericksen (1981, 1983). This study will test the salt heave hypothesis further by focusing on a soil profile located within the hyperarid core of the Atacama Desert, which shares similar salt mineralogy and surface/subsurface features observed in previous studies by Ericksen (1981, 1983).

Study Site (Oficina Ercilla)

In order to better understand the pedogenic processes occurring in the most extreme environment on Earth, this research project focuses on one of the most hyperarid and nitrate-rich portions of the Atacama Desert, the Ercilla Valley. The Ercilla Valley is a subsidiary basin to the Baquedano Valley (Figure 1.4). It is a NNE-SSW trending valley with approximate dimensions of 15 km long and 5 km wide. This study specifically focuses on a soil profile, Oficina Ercilla (OE), located near the southern terminus of the Ercilla Valley approximately 80 km NE of Antofagasta, Chile. OE is also about 20 km north of of Baquedano and Highway 5 along rural road B-330 (23 07' 30" S, 69 51' 41" W) at approximately 1400 m.a.s.l. (Figure 1.8). The landscape in the Ercilla Valley is consistent with the description by Ericksen (1981) of alluvial type nitrate deposits. Bedrock ridges are rounded by eolian modification, which has blanketed most of the hills, gullys, and valleys created during a previous wetter climate(s) with airborne dust and sediment (Figure 1.9 and 1.10). Most of the geomorphic surfaces are smooth and gently sloping except where historic mining has left an abrupt scarp at lower levels of hillslopes, slope breaks, and relatively flat upper fan surfaces (Figure 1.10B) where nitrate is known to be in the greatest abundance (Ericksen, 1981). These alluvial fan landforms are composed of "Atacama gravels" characterized by poorly sorted sediments including silt, sand, gravel, and large cobbles/boulders (Figure 1.9). Deposition of the Atacama gravels occurred from the Oligocene into the Miocene, ceasing ~13-15 Ma at the transition from an arid to hyperarid climate in the mid-Miocene (Mortimer and Saric, 1975; Ericksen, 1981; Nishiizumi et al., 2005). OE was heavily mined for nitrate in the late 19th and early 20th century and has been subjected to some recent activity as well. A

nearby cemetery indicates mining from at least 1901-1915 at this site specifically (Figure 1.10A). Historic mining has left behind several continuous 500-1000+ m exposures of indurated soil and exploration pits along the gently sloping geomorphic surfaces at OE (Figure 1.10B). At least three geomorphic surfaces are present at this location including an older upper fan surface (where most of the nitrate mining occurred), a lower (inset) fan surface, and a presently dry fluvial terrace(s), but time constraints prevented sufficient investigation/ mapping of these and potentially other surfaces.

The study site is located on the uppermost geomorphic surface (upper fan), along the east side of the valley, and positioned medially on an alluvial fan dipping ~6° to the west. At higher elevations, or where previous mining has tapped into bedrock, altered volcanic outcrops are readily identified (Figure 1.10A). The soil-hosting alluvium at OE also consists of mostly volcanic or hydrothermally altered volcanic rocks. These rocks are poorly sorted subrounded to subangular clasts supported/cemented by a matrix of salt, silt, and sand. Clasts/gravels typically range from 1 to 12 cm in length and were noted in the field as fine grained aphanitic to porphorytic rhyolite, andesite, or tuff. However, some granitic clasts are present. Sporadic surface clasts/gravels only reflect volcanic (rhyolite) origins on the upper fan surface and ranged from 0.5 to 50 cm in lenth. Erratic granodiorite cobbles-boulders exist on the surface of the lower fan and fluvial terrace(s), which were used for cosmogenic dating by Prellwitz (2007). The surface is void of visible flora and fauna. However, anthropogenic disturbances, such as tailings piles and vehicle ruts, from mining activities are still strongly visible due to lack of biologic processes and limited precipitation (Figure 1.11B). The closest consistent rain data comes from Antofagasta, which reports a precipitation average of 1.7 mm annually

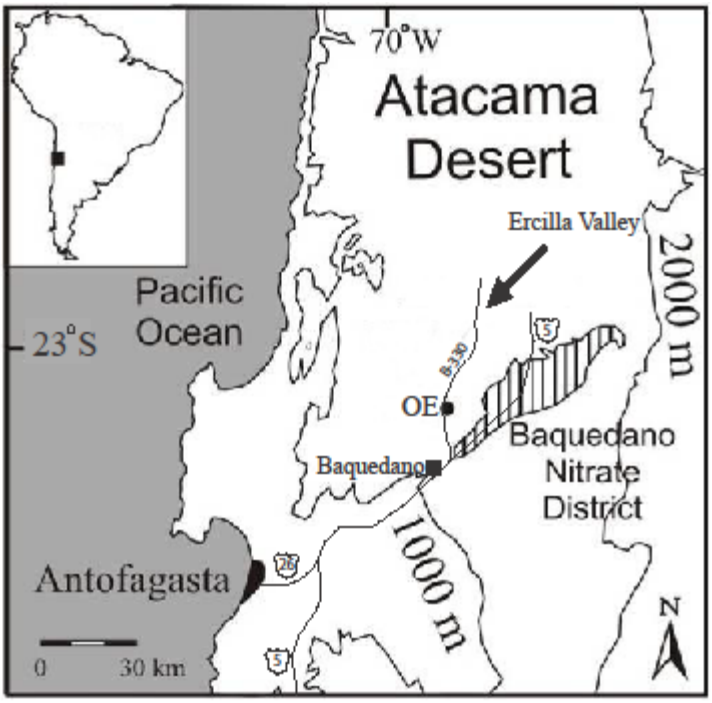

Figure 1.8. Location map of OE site, modified from Prellwitz (2007).

Figure 1.9. Field photo of "Atacama gravels" along road cut (B-330) near OE.

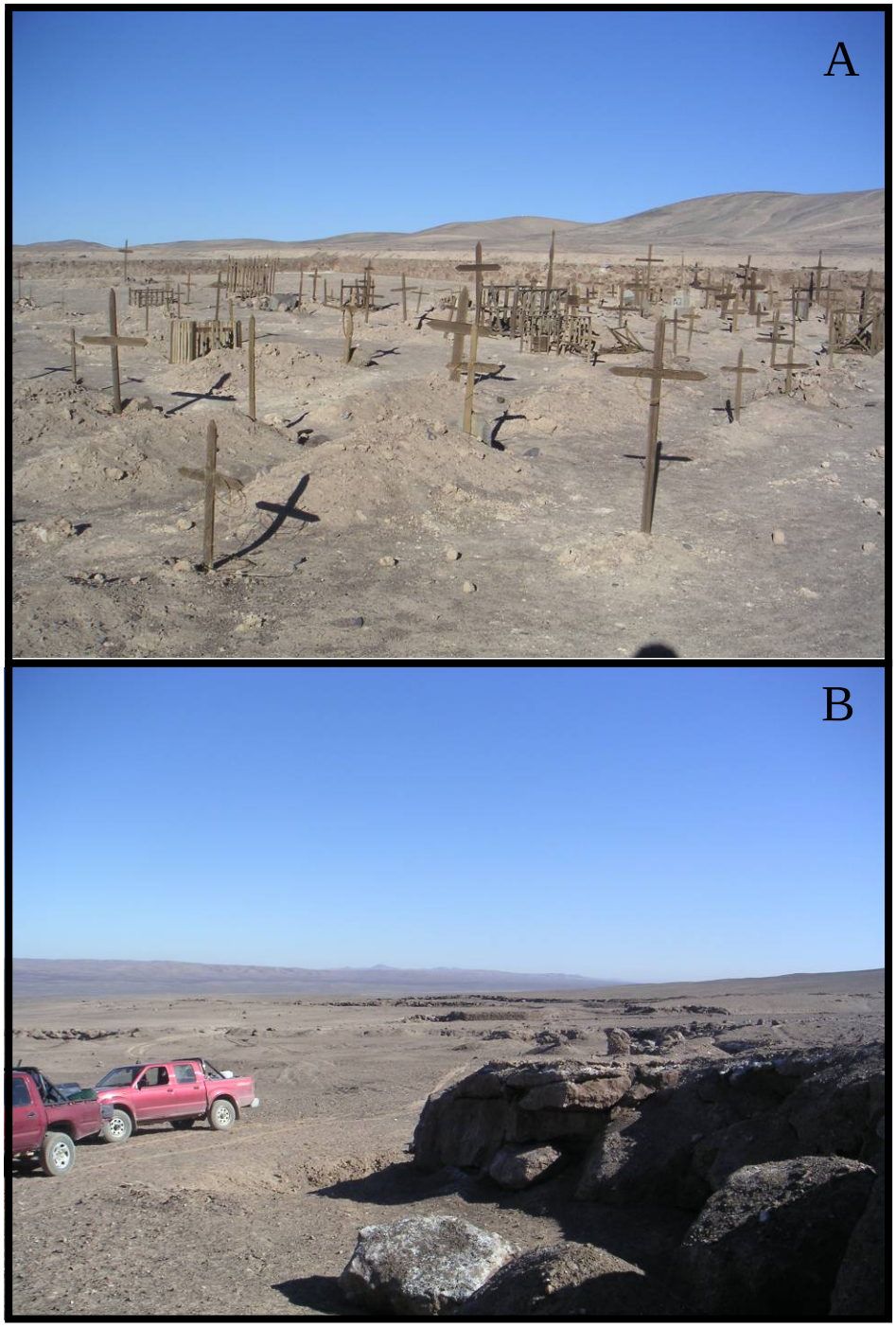

Figure 1.10. A) Cemetery for nitrate miners near OE site, circa 1901-1915. **B)** OE site soil outcrop left by historic nitrate mining.

(Dirección Meteorológica De Chile, 2006). Limited rain data from Baquedano recorded from 1975 to 1989 averages 4.15 mm annually. However, 42 mm of the 62.2 mm measured rainfall occurred in January 1975 (data acquired via personal communication with Dr. Jason Rech, Miami University). Furthermore, eight of the fifteen years of this rain data had no measurable rainfall. This supports previous comments that average precipitation does not imply annual precipitation and the apparent rainfall may be inflated by the genuine lack of data. Precipitation at OE is likely much less than 1.7 mm or 4.15 mm due to the distance inland and topographic relief between the site and Antofagasta or Baquedano as well as all sources of moisture. However, there is field evidence for at least one rain event since the cessation of mining in the form of runoff gullies along tailings piles and mud drapes on outcrops. As a result of soil induration at OE, the soil profile was described and sampled at remnant mining exposures (Figure 1.12).

Figure 1.11. A) Altered volcanic bedrock exposure on ridge near OE site, rock hammer for scale (red arrow). B) Horse remains and preserved modern / historic vehicle ruts near OE site.

Figure 1.12. Sampling OE soil on nitrate mining outcrop with electric saw / generator.

CHAPTER II

METHODOLOGY

Soil Profile Selection and Sampling

Profile Selection

The Oficina Ercilla (OE) soil profile was selected for analysis based upon a combination of characteristics: (1) It is on the uppermost and oldest geomorphic surface in the valley, and would be the most likely soil profile to represent the maximum duration of soil formation. (2) Following a day of reconnaissance by truck and on foot this site also provided the most prolific (>1000 m) and accessible exposures to ≥3 m depth, which would have been otherwise impossible to observe without the historic nitrate works. (3) The presence and abundance of visible salt accumulation, distinct soil horizonation, vertical fissures, and patterned ground were more compelling at this site as well. These attributes also closely reflected descriptions by Ericksen (1981, 1983), which were considered useful for geologic/pedologic comparisons and mineralogic proxy. (4) Anthropogenic disturbance/destruction from historic/modern mining activity was also less extensive leaving adjacent areas with intact unconsolidated (surficial) soil horizons. The profile was described along a ~20 m section of an exposure measuring 3.18 m vertically (a remnant of historic mining) according to standard USDA techniques outlined in Schoenberger et al. 2002 and soil color by Munsell Color Chart.

However, this single exposure is representative of the overall geomorphic surface as horizonation was viewed and consistently traced along the >1000m outcrop (Figure 1.11B) verified during field reconnaissance.

Sampling

Sampling methodology was two-fold used both conventional and site-inspired sampling techniques. Conventional methods were used to characterize soil, collecting samples vertically from the surface to the maximum depth of exposure based on measured thicknesses/depths of individual horizons. However, the heterogeneity of salt and silicate mineral accumulation throughout the soil profile at OE is visually apparent due to contrasting soil color, texture, and structure between and within characterized horizons. This as well as obvious trans-horizon soil cracks containing laminae of both salt and silicate minerals instigated additional sample collection in order to study pedogenic processes responsible for these soil attributes. Therefore, horizontal and vertical sampling transects or duplicate samples were collected within all soil horizons to confirm the noticeable mineral and textural variability. Similarly, vertical and horizontal laminae of interest in soil cracks were sampled along horizontal/vertical transects to elucidate any spatial trends in crack mineralogy/ texture and/or differences between mineralogy/ texture in cracks versus soil horizons. Additional samples were also collected from random infilled cracks/veins to determine the specific mineralogy of “pure” white powdery salt(s) commonly impregnating/marbling indurated horizons.

Field sampling yielded a total of 13 OE samples, which included multiple samples from each described horizon, vertical/horizontal laminae, and visible salt accumulations. Extremely cemented samples were extracted using an electric saw, equipped with a

diamond impregnated blade and run by a gas-powered generator, to allow the collection of fresh samples ~4-5 cm deep into the face of outcrops. Samples from indurated horizons were collected from the outcrop exposures to acquire specimens from maximum observed depths (Figure 1.13). Individual soil samples from indurated horizons were marked to indicate orientation, wrapped in tissue, secured with duct tape and then sealed in a zip lock bag. Semi-intact peds from the surficial horizons were collected similarly. Bulk samples from unconsolidated horizons were collected in large zip lock bags or metal sample tins, also sealed in zip lock bags, to prevent contamination or salt alteration during transport back to the laboratory.

Laboratory Analyses

Laboratory analyses were divided into untreated and pretreated tests. Until these analyses were underway all samples were stored in conditions as similar to the field as possible. Untreated analyses include: (1) pH, (2) EC, (3) a salt hydration-temperature experiment for one horizon, (4) petrographic inspection of soil thin sections, (5) SEM/EDS of the same soil thin sections, and (6) XRD of bulk mineralogy. No water was used during sample preparation for these analyses unless inherent in the method used (i.e. analyses 1 – 3). Pretreated analyses include: (1) XRD of clay mineralogy and (2) textural analysis. These tests required the use of RO water to remove soluble salts before analyses ensued. Soluble salts were removed using methods detailed in Soukup et al., (2008) with the aid of a Fisher Scientific Accumet AB30 conductivity meter in the Environmental Soil Analytical Laboratory (ESAL) located on the campus of the University of Nevada, Las Vegas (UNLV).

pH and Electrical Conductivity

Both pH and EC were determined following the guidelines in the NRCS Soil Survey Laboratory Methods Manual and the analyses were performed in the UNLV ESAL. Measurements for each horizon were acquired with a 1:1 saturated paste using NRCS Soil Survey Laboratory methods (Soil Survey Staff, 2004): 4F2 (Saturated Paste) (Bohn et al., 1979; Rhoades, 1982; U.S. Salinity Laboratory Staff, 1954), 4C1a2a1 (pH) (Foth and Ellis, 1988; McLean, 1982; Soil Survey Staff, 1999), 4F2c (EC extraction) (Holmgren et al., 1977; U.S. Salinity Laboratory Staff, 1954), and 4F2b1 (EC measurement) (U.S. Salinity Laboratory Staff, 1954) except for one horizon, the Bz horizon discussed in the next chapter. This horizon's pH and EC was measured immediately after hydration as the overwhelming salt content (>99%) undermined the effectiveness of the fore mentioned method. pH was recorded using a Thermo Orion 720A+ pH meter directly inserted into the saturated paste/hydrated sample. EC was recorded using a Fisher Scientific Accumet AB30 conductivity meter.

Salt Hydration-Temperature Experiment

As a result of observations during EC analyses, the Bz horizon was additionally subjected to a hydration-temperature experiment. A 10 g sample of the soil horizon was rehydrated with 10 mL of RO water, gently stirred until mixed with a thermometer while noting the temperature change. The timed experiment started at hydration and ended at 60 minutes. Temperature measurements were recorded at 10s, 30s, 45s, and 60s for the first minute. Between minutes 1 and 5, temperature was recorded at 30s intervals. After the fifth minute, measurements were taken at 5 minute intervals until the final 60 minute

reading. 5 runs of the experiment were performed, and then graphically translated in spreadsheet form.

Microscopic Techniques

Petrography

Nineteen subsamples were chosen, primarily based on the presence of visible salt and soil fractures of varying orientations, but all horizons were sampled/ prepared for microscopic analyses. In order to prepare for petrographic analyses: 14 billets were sent to National Petrographic Services in Houston, TX for thin section fabrication (with strict instructions not to use water at any stage of sample preparation). Three thin sections were made in house, for samples considered too fragile for shipping, using Spurr low-viscosity embedding media. Thin sections were examined primarily on a Nikon Eclipse LV100POL polarized light microscope equipped with a Nikon DS-Fi1 digital still camera and supporting NIS imaging software. Photographic documentation focused on salt mineralogy/assemblages, soil fabric, and other pedogenic features (i.e. cracks) to aid Scanning Electron Microscopy/Energy Dispersive X-ray Spectroscopy (SEM/EDS) and interpretation of pedogenic processes. Thirteen samples were also point counted on a 1mm by 1mm grid spacing to obtain 400 counts. Points were grouped by specific (if possible) salt minerals, argillans, voids, soil micromass, or parent material grains. Additionally, in some instances petrographic observations were used contemporaneously with SEM/EDS analyses to positively identify salt minerals.

SEM/EDS

All seventeen thin sections prepared as part of petrographic analyses were also examined using SEM/EDS analyses. Six additional grain mounted samples were analyzed for two unconsolidated horizons (Byz and Bz discussed below). These were mounted to a brass cylinder using carbon tape. All samples were first coated with gold for 30-60 seconds using a Cressington 108 Auto sputter coater then transferred to the SEM/EDS equipment. These analyses were performed in the UNLV EMIL laboratory with a JEOL-5600 SEM equipped with an Oxford ISIS EDS system, which was updated to the Oxford INCA EDS system during the latter stages of this study. 510 digital images along with 422 EDS elemental spectrums were acquired. However, EDS analyses were used prolifically while scanning samples without necessarily saving a digital copy of the elemental spectrum. This would account for at least the apparent difference in the amount of images versus elemental analyses, but an additional 200 EDS analyses would not be unreasonable. All of the SEM/EDS data was collected while employing the SEM's backscattered electron (BSE) detector in order to emphasize compositional variation in salt mineralogy.

X-Ray Diffraction (XRD)

XRD analyses were performed by step scanning using a PANalytic X'Pert PRO diffraction system in the UNLV XRD Lab. CuKα radiation (K-alpha1= 1.54060 Å, K-alpha2=1.54443Å) was used at 40 kV, 40 mA. Step intervals range from 0.0170˚ (bulk mineralogy) to 0.0080˚(clay analyses) 2θ with a step-counting time of ~0.25 ms to achieve a 15 minute run time. A 10 mm X-ray beam mask along with 0.5˚ antiscatter and

0.25˚ divergence slits were used to focus the beam during analyses. Diffraction patterns were generated from a 6˚ - 75˚ 2θ range for bulk mineralogy and a 4˚ - 40˚ 2θ range for clay minerals.

Bulk Mineralogy (including salts)

Sixteen subsamples, from various depths, were analyzed using this method. XRD data for bulk mineralogy was obtained using the powder method. The subsamples were collected as a bulk mass or extracted with dental scraping tools from the original 15 OE samples. After grinding by hand with mortar and pestle they were transferred into a 1.6cm diameter powder mount utilizing ~0.5g of each sample. Diffraction patterns were imported into X'Pert High Score software where sample mineralogy was determined by matching diffraction profile peaks via auto-identify and user-defined database queries. The percentage generated for each of the minerals in the samples is a semi-quantitative estimate associated with relative intensity ratios (RIR), established in the software database, that are used in conjunction with the amount of a given mineral per volume of sample.

Clay Mineralogy

Eight samples, from various depths, were analyzed for clay mineralogy. XRD data for clay mineralogy was obtained using pretreated clay slurries mounted on frosted glass slides. Pretreatment first entailed fractionation, which was performed using methods detailed in Soukup et al., (2008). Each sample was then split; each half was treated with either 1N KCl or 1N $MgCl_2$ solutions. After K-treated samples were mounted to glass slides, XRD data was collected at 25°C and after heating to 350°C and 550°C for 2 hours in a muffle furnace. XRD data was collected from Mg-treated samples at 25°C and after

ethylene glycolation in a heated dessicator (65˚C) under vacuum for 2 hours (Harris and White, 2008). XRD data for each sample was then imported into X'Pert High Score software where diffraction profile peaks were stacked to evaluate peak shifts with each treatment. Clay mineralogy was identified using known diagnostic d-spacing measurements, compiled from Dixon and Schulze (2002), the USGS (United States Geological Survey) website, and the AXAA (Australian X-ray Analytical Association) website.

Texture Analysis

Particle size analysis was performed on a total of 25 samples extracted from multiple depths and subsurface features of the OE profile. Samples were rinsed three times in the UNLV ESAL with RO water and monitored with a Fisher Scientific Accumet AB30 conductivity meter to ensure salts were not present to flocculate fines and influence textural classification. Therefore, the Bz horizon was not analyzed because it is comprised of >99% salt. Each sample was sieved to obtain the ≤2mm (fine earth) fraction. Particle size was determined using a Malvern Instruments Mastersizer 2000 with Hydro sample dispersion unit equipped with a continuously variable stirrer and ultrasonic probe. Samples were dispersed in RO water and particle size measured by laser diffraction. Sand, silt, and clay fractions were then used to attain USDA texture classification. A visible estimate of gravel in soil outcrops was used in conjunction with texture class to determine particle size distribution (Shoeneberger et al., 2002).

CHAPTER III

SOIL PROFILE DESCRIPTION AND RESULTS

This chapter presents a combined set of field observation/descriptions, while visiting the Ercilla Valley in October 2005, and the data acquired from subsequent laboratory analyses discussed in Chapter II. Results from mineralogic, macro/micromorphologic, and other laboratory analyses are detailed by soil horizon. Summaries of horizon (bulk) data from the OE soil profile are given in Tables 1-7.

Landform & Surface Description

The OE soil profile is located medially on an alluvial fan dipping ~6° to the west (Figure 3.1). Exposed soil outcrops and surface lithologies reveal that the parent material is alluvial gravel composed mostly of volcanic or hydrothermally altered volcanic lithologies. These sediments are poorly sorted with subrounded to subangular fine-grained aphanitic to porphorytic clasts of rhyolite, andesite, or tuff (1 to 12 cm in length) supported/ cemented by a matrix of salt, silt, and sand. However, some subrounded clasts are granodioritic in the subsurface. Surface clasts/ gravels (0.5 to 50 cm in lenth) only reflect volcanic lithologies on the upper fan surface and form a non-interlocking desert pavement (Figures 3.1 & 3.2). Pavement coverage is variable, but ranges from 0 to 35%. The surface was also highlighted by polygonal networks of large soil cracks (10 to 20 cm

TABLE 1. SUMMARY OF SOLUBLE SALTS IDENTIFIED IN OE PROFILE

Mineral	Chemical Composition	Density (g/cm^3)	Solubility* ($g/kg\ H_2O$)
Calcium Carbonate	$CaCO_3$	2.71	0.0066
Gypsum	$CaSO_4*2H_2O$	2.32	2.05-2.08
Bassanite	$CaSO_4*0.5H_2O$	2.7	2.05-2.08
Anhydrite	$CaSO_4$	2.96	2.05-3.11
Glauberite	$Na_2Ca(SO_4)_2$	2.8	118
Eugsterite	$Na_4Ca(SO_4)_3*2H_20$	2.5	269
Thenardite	$NaSO_4$	2.7	281
Halite	NaCl	2.17	360
Nitratine	$NaNO_3$	2.26	920
Darapskite	$Na_3(NO_3)(SO_4)*H_2O$	2.2	-†

* Composite list of values from Alpers et al. (2000) and Lide (2008), in DI water.
† Denotes no data

TABLE 2. pH / EC DATA SUMMARY FOR OE PROFILE

Horizon	Depth (cm)	Description	pH	EC (mS/cm)
Avz	0-2	loose	8.03	14
Byz	2-11	loose	8.31	20
Bz	11-15	loose	9.08	42
Bzm1	26-34	EE1 massive	7.64	84
Bzm1	26-34	EE1 horiz. laminae	7.57	84
Bzm2	75	EE2-2 massive	7.21	87
Bzm2	75	EE2-2 horiz. laminae	7.15	85
Bzm2	126-138	EE1 massive	7.26	82
Bzm2	126-138	EE1 vert. crack	7.44	88
Bzm2	153	EE3-1 massive	7.07	81
Bzm2	153	EE3-1 vert.crack	7.26	83
Bzm2	292	EE4 vert. crack	7.16	80
Bzm2	300-305	EE1 massive	7.18	68

TABLE 3. SALT PERCENTAGE AND TEXTURE OF OE PROFILE BY HORIZON

Depth (cm)	Soil Horizon	Soil crack*	% Salt †	Texture Analysis			
				%clay	*%silt*	*%sand*	*USDA classification*
1	Avyz	no	13	17	43	40	loam
6	Byz	V	33	-§	-	-	-
6	Byz	no	71	12	56	31	silt loam
13	Bz	no	99	-	-	-	-
34	Bzm1	no	51	16	52	32	v. gravelly silt loam
58	Bzm2	no	41	7	60	33	v. gravelly silt loam
75	Bzm2	no	53	9	61	29	v. gravelly silt loam
80	Bzm2	H	55	10	40	50	v. gravelly loam
89	Bzm2	no	37	5	59	36	v. gravelly silt loam
132	Bzm2	V	37	6	56	37	v. gravelly silt loam
132	Bzm2	no	38	9	38	53	v. gravelly sandy loam
146	Bzm2	no	33	4	51	45	v. gravelly silt loam
153	Bzm2	V	47	18	53	29	v. gravelly silt loam
153	Bzm2	V	35	7	69	24	v. gravelly silt loam
153	Bzm2	V	44	6	63	31	v. gravelly silt loam
155	Bzm2	no	29	6	61	33	v. gravelly silt loam
183	Bzm2	no	31	8	72	21	v. gravelly silt loam
232	Bzm2	no	34	6	55	39	v. gravelly silt loam
235	Bzm2	no	19	4	35	61	v. gravelly sandy loam
235	Bzm2	no	23	7	66	26	v. gravelly silt loam
252	Bzm2	V	46	8	63	29	v. gravelly silt loam
252	Bzm2	V	51	15	63	22	v. gravelly silt loam
265	Bzm2	no	19	8	51	41	v. gravelly silt loam
293	Bzm2	V	50	6	70	24	v. gravelly silt loam
293	Bzm2	V	24	5	59	35	v. gravelly silt loam
300	Bzm2	no	41	3	22	76	v. gravelly loamy sand
300	Bzm2	no	31	2	23	74	v. gravelly loamy sand

* Denotes samples from soil fractures; (no) not soil crack, (H) horizontal or (V) vertical cracks

† Data acquired from Prellwitz (2007) on same samples

§ "-" Denotes no data

TABLE 4. SUMMARY OF OE PROFILE POINT COUNT DATA BY HORIZON

Horizon	Position	Sample ID	Depth (cm)	Total Counts	Micro mass*	Grains†		Salt Minerals					Argillan	Void
						V	P	NaCl	$NaNO_3$	SO_4				
										Ca	Na	CaNa		
					Values in %									
Avyz	ped	OE Avyz	0-2	400	37§	13	17	0	0	0	0	0	0	33
Byz	ped/v. crack	OE Byz	2-11	400	7§	36	9	0	0	30	0	0	0	18
Bz	loose salt	–#	11-15	0	-	-	-	-	-	-	-	-	-	-
Bzm1	massive	OE Bzm	26-34	400	31	19	3	22	4	0	4	0	0	17
Bzm2	h. crack	OE2-2A	75	400	31	24	1	17	1	0	11	0	0	15
Bzm2	h. crack	OE2-1	80	400	34	30	1	14	0	0	8	0	0	13
Bzm2	massive/v. crack	OE3-3B	153	400	43	31	1	15	9	0	0	0	1	0
Bzm2	v. crack	OE3-1B	153	400	27	33	4	15	17	0	0.5	0	0.5	3
Bzm2	v. crack	OE3-1A	153	400	10	39	2	24	15	1	0	2	2	5
Bzm2	massive	OE2-3	155	400	4	62	4	13	3	6	0	3	3	2
Bzm2	massive	OE1	174-180	400	15	51	13	5	0	14	0	0.5	0.5	1
Bzm2	v. crack	OE4A	258	400	20	36	15	16	8	1	0	1.5	1.5	1
Bzm2	v. crack	OE4B	292	400	35	43	1	8.5	0	12	0	0	0	0.5
Bzm2	massive	OE1	300-305	400	22	25	47	3	2	0	0	0	0	1

* Undifferentiated salt cemented/indurated fine material acting as a supportive soil matrix

† Parent Material grains or clasts; V denotes volcanic origin; P denotes plutonic origin

§ Denotes micromass not cemented/indurated with salt

"-" Denotes no data

TABLE 5. SUMMARY OF SEM-EDS MINERALOGY AND MICROMORPHOLOGY OF OE PROFILE BY HORIZON

Horizon	Depth (cm)	Position	Mineralogy*	Crystal Habit and Size
Avyz	0-2	random	Gypsum & Halite†	no data
Byz	2-11	ped	Gypsum/Bassanite / Anhydrite	anhedral to euhedral, commonly skeletal, lenticular/prismatic (≤30μm crystals, ≥125μm clusters or snowballs) displacing soil matrix with no preferred orientation
Bz	11-15	random	Thenardite	subhedral to euhedral dipyramidal (20-200 μm)
			Glauberite	subhedral to euhedral tabular and prismatic (~30 μm)
			Eugsterite	subhedral to euhedral acicular (50-60μm) radiating clusters
Bzm1	15-38	massive	Halite	anhedral interstitial masses (>100 μm) to massive soil matrix cement
			Glauberite	anhedral masses (100-200μm) at grain boundaries and interstitial space
			Thenardite	anhedral masses (100-200μm) at grain boundaries and interstitial space
Bzm2	38-318	h.crack	Halite	anhedral masses (>100μm) to massive as interstitial cement or void coatings (<100μm thick), subhedral to euhedral cubic (<50μm)
			Nitratine	anhedral masses (>100μm), subhedral to euhedral rhomboidal (15-100μm)
			Glauberite	aggregates of anhedral to subhedral tabular (5-100μm), prismatic radiating clusters (20-40μm)
			Thenardite	subhedral to euhedral prismatic (<100μm), radiating prismatic clusters (100-200μm) near voids
		v.crack	Halite	massive as interstitial cement, fracture fills, and grain coatings (20-100μm thick), subhedral to
			Nitratine	subhedral to euhedral rhomboidal (20-50μm) as masses, in fractures, or along grain boundaries; anhedral masses (100-200μm); massive as interstitial cement, fracture fills, and grain coatings
			Anhydrite	alabastrine (<20μm) in interstitial space and fracture fills; fragmental (10-100μm)
			Calcium Carbonate	anhedral masses in interstitial space (>100 μm)
			Glauberite	anhedral to massive as interstitial cement
		massive	Halite	massive as interstitial cement, fracture fills, or grain coatings (<100μm thick); anhedral masses (~50μm) and subhedral to euhedral cubic (50μm) near voids
			Nitratine	subhedral rhomboidal (~10μm) in voids; subhedral to euhedral rhomboidal (15-20μm) in fractures; anhedral masses (<100μm); massive in interstitial space/void fills
			Glauberite	anhedral to massive as interstitial cement or grain coatings
			Anhydrite	alabastrine (<20μm) in interstitial space and fracture fills
			Thenardite	subhedral prismatic (<50μm) near voids

* Listed by visually estimated abundance per horizon position

† Implicated by field observation (taste), but not identified with SEM/EDS

TABLE 6. SUMMARY OF XRD MINERALOGY OF OE PROFILE BY HORIZON

Soil Horizon	Depth (cm)	Sample ID	Sample Description	Mineralogy Untreated Samples (%)													
				Halite	Gypsum	Bassanite	Anhydrite	Thenardite	Glauberite	Nitratine	Darapskite	Mg-Sulfate	Quartz	Plagioclase	Illite	Kaolinite
Avyz	1	OE-H	Horizon directly above samples EE-A through EE-D	*	4	-†	-	-	-	-	-	-	49	34	11	2
Byz	3	OE-E	White salt accumulation in ped adjacent to OE-F	-	1	91	-	-	-	-	-	8	-	-	-	-
Byz	5	OE-D	White salt accumulation in ped adjacent to OE-B	-	5	-	94	-	-	-	-	-	1	-	-	-
Byz	6	OE-F	Vertical laminae at ped boundary	-	18	23	-	-	-	-	-	-	31	17	11	-
Byz	6	OE-G	White salt accumulation in ped adjacent to OE-F	-	56	-	30	-	-	-	-	-	1	13	-	-
Byz	9	OE-A	Center of vertical laminae	-	6	61	-	-	-	-	-	-	8	25	-	-
Byz	9	OE-B	Vertical laminae at ped boundary	-	27	9	-	-	-	-	-	-	43	21	-	-
Byz	9	OE-C	Vertical laminae between OE-A and OE-B	-	17	53	-	-	-	-	-	-	9	20	-	-
Bz	12	OE-Q	Loose white salt horizon	-	-	-	-	96	4	-	-	-	-	-	-	-
Bzm1	18	OE-I	Horizontal laminae, upper	16	-	-	-	-	12	35	5	-	10	22	-	-
Bzm1	26	OE-J	Horizontal laminae, lower	20	-	-	-	-	14	48	2	-	2	14	-	-
Bzm1	26	OE-K	Horizontal laminae	27	-	-	-	-	15	52	-	-	1	5	-	-
Bzm2	92	OE-M	Vertical laminae at massive boundary, below OE-K	16	-	-	-	-	15	43	-	-	19	6	-	-
Bzm2	93	OE-N	Massive adjacent to OE-M	13	-	-	-	-	12	22	-	-	27	15	7	4
Bzm2	126	OE-P	Massive, adjacent to OE-O	8	-	-	-	-	8	22	-	-	36	17	7	1
Bzm2	137	OE-O	Vertical laminae at massive boundary	15	-	-	-	-	15	38	-	-	25	7	-	-
Bzm2	258	OE-L	White salt vein in vertical crack	2	-	-	93	-	3	1	-	-	1	-	-	-

* Suspected by taste, but below XRD detection limits

† "-" Denotes none present, or below XRD detection limits

TABLE 7. SUMMARY OF XRD CLAY MINERALOGY OF OE PROFILE BY HORIZON

Soil Horizon	Depth (cm)	Sample ID	Sample Description	Mineralogy Treated Samples*			
				Illite	Kaolinite	Smectite	Chlorite
Avyz	0-2	OE-Avyz	Loose, random sample	C	C	m	m
Byz	2-11	OE-Byz	Composite ped sample	C	C	m	m
Bz	11-15	-†	-	-	-	-	-
Bzm1	26-34	OE-Bzm1 massive	Massive sample	C	C	m	m
Bzm1	26-34	OE-Bzm1 h.crack	Horizontal laminae adjacent to Bzm1 massive sample	C	m	m	m
Bzm2	75	OE-Bzm2 h.crack	Horizontal laminae	m	m	m	m
Bzm2	153	OE-Bzm2 v.crack	Vertical laminae	m	m	m	m
Bzm2	292	OE-Bzm2 v.crack	Vertical laminae	C	m	C	m
Bzm2	300-305	OE-Bzm2 massive	Massive sample	C	m	C	m

* Relative abundance in clay fraction, C denotes common or prevalent, m denotes minor

† "-" Denotes no data; horizon contains >99% salt, no clay analysis performed

Figure 3.1. Mostly undisturbed OE fan surface, looking updip (E-SE) from distal perspective; rock hammer (red arrow) for scale. Note smoothed topography and faint expressions of patterned ground between rock hammer and ridgeline.

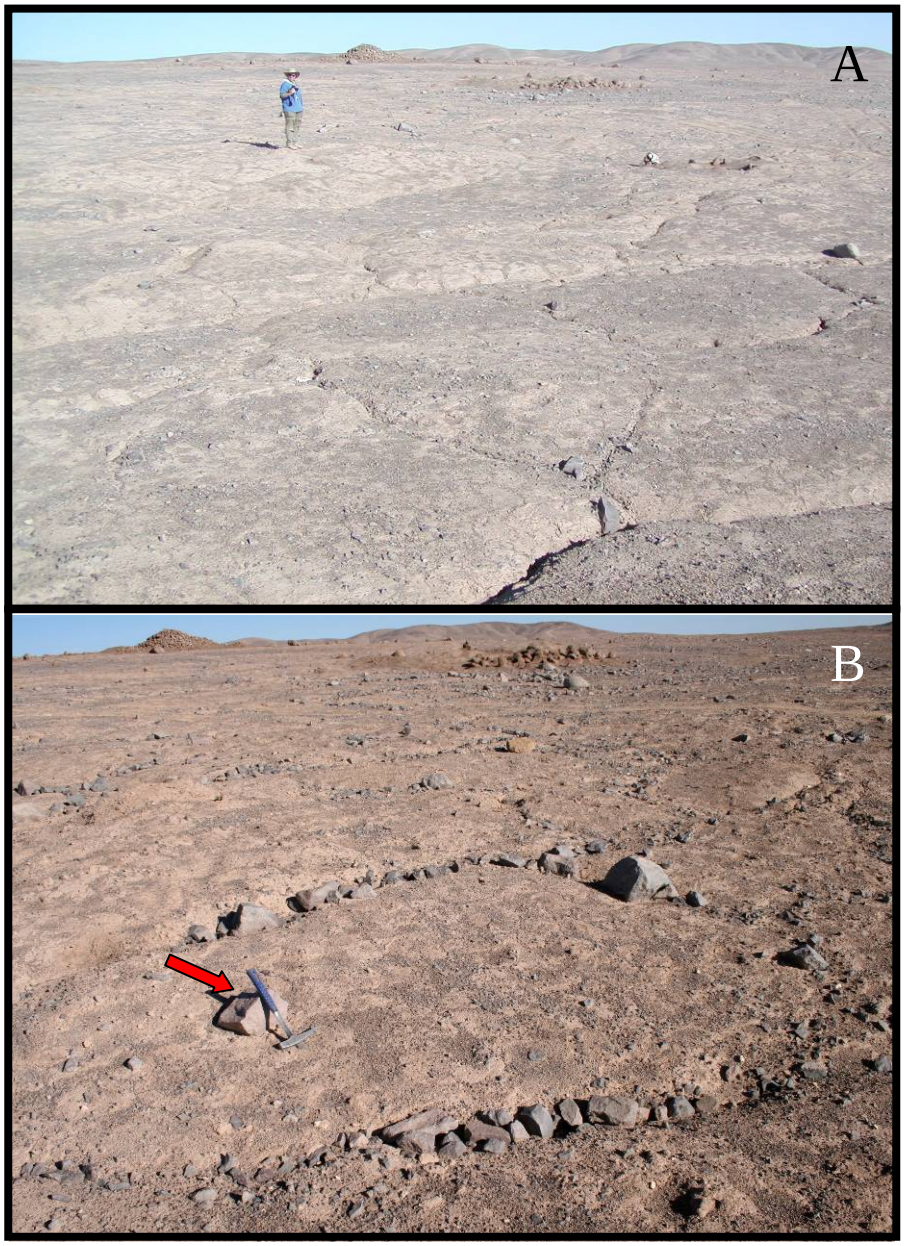

Figure 3.2. A) Undulating surface and patterned ground at inset, younger surface below OE site, advisor for scale. **B)** Patterned ground accented with large clasts/cobbles, rock hammer (red arrow) for scale. Also note early 20th century tailings piles in background of both photos.

width) infilled with salt, sediment, and surface clasts (Figure 3.2). Polygon dimensions range from 1 to 2m in diameter. Surface highs in the centers of soil polygons and surface lows at soil cracks bounding polygons exhibit surface microrelief (≤5 cm), which translates into a gently undulating soil surface from one soil polygon to the next. This adds a noticeable microtopographic complexity to the gentle westward slope of the fan surface, interrupted only by historic mining scarps or ancient drainage pathways obscured/rounded by eolian deposition.

Soil Profile Description

The OE profile was described to a depth of 318 cm. Visually estimated gravel percentage range between 35 and 60%. Therefore, horizons are predominately very gravelly silt loams (Table 3). Five horizons are designated as an Avyz, Byz, Bz, Bzm1, and Bzm2 respectively with depth based on field and laboratory observations (Figures 3.3-3.5, Table 9;Appendix). The upper 3 horizons contribute to a mostly unconsolidated (loose or friable) unit except in the Byz where incipient Stage III salt accumulation has a more resilient columnar soil structure (Figure 3.6). The underlying 2 horizons are a strongly indurated zone (Figures 3.5 & 3.7). Vertical cracks (10 to 20 cm wide) extend from the surface and cut through all horizons (Figure 3.4 & 3.8). These larger cracks correlate to the surficial cracks forming patterned ground (Buck et al., 2006). Smaller cracks (1 to 5 cm wide) penetrate only the unconsolidated horizons (15 to 25 cm depth, see Figure 3.6 A). All cracks narrowed with depth. Some fractures were also observed in vertical, sub-vertical, and horizontal orientations, which did not propagate from or transmit to the surface. Vertical and horizontal laminae of salt and sediment were

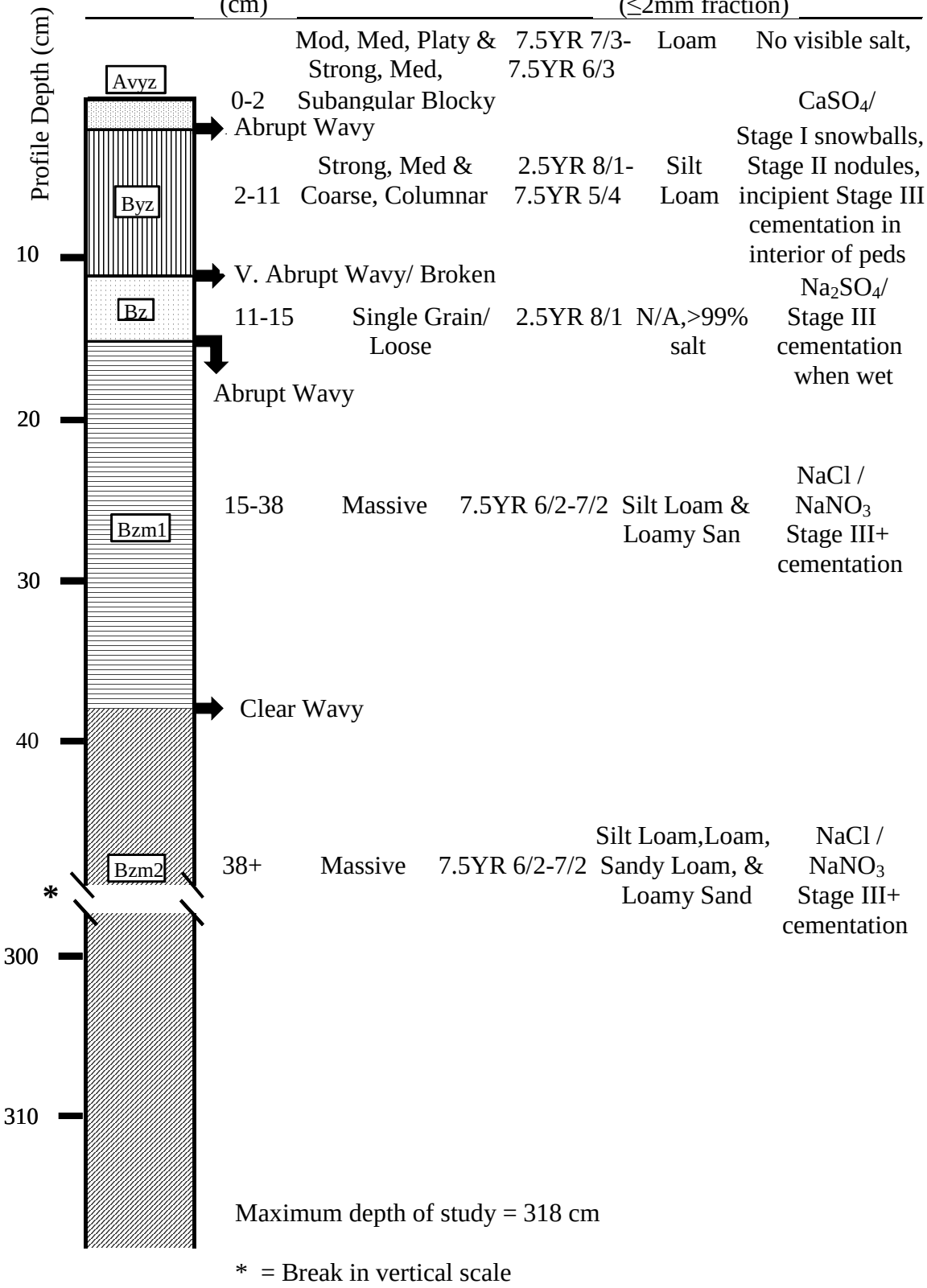

Figure 3.3. Soil profile at Oficina Ercilla and descriptions, also see Table 9 in Appendix.

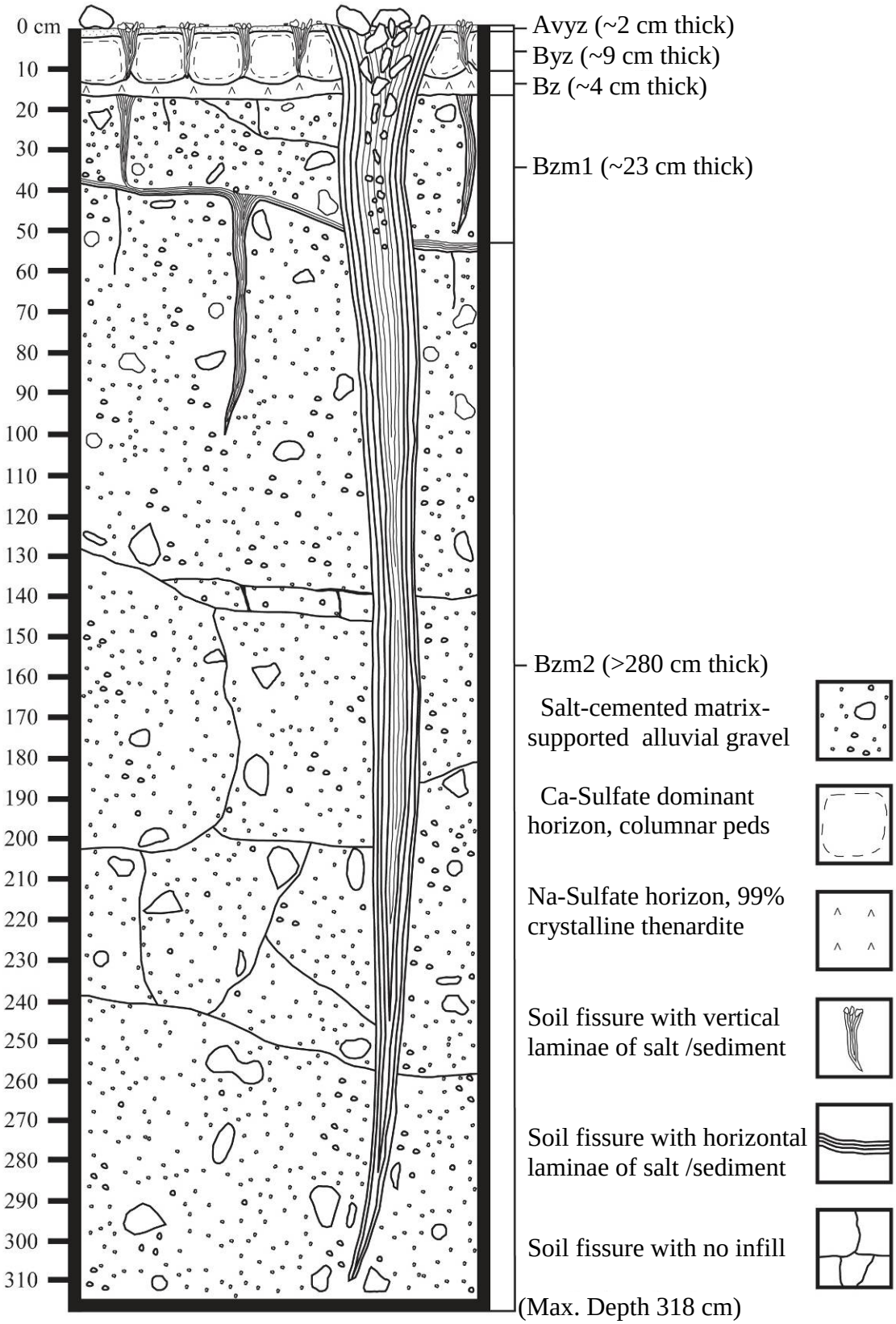

Figure 3.4. OE soil profile with horizonation description and explanation of features.

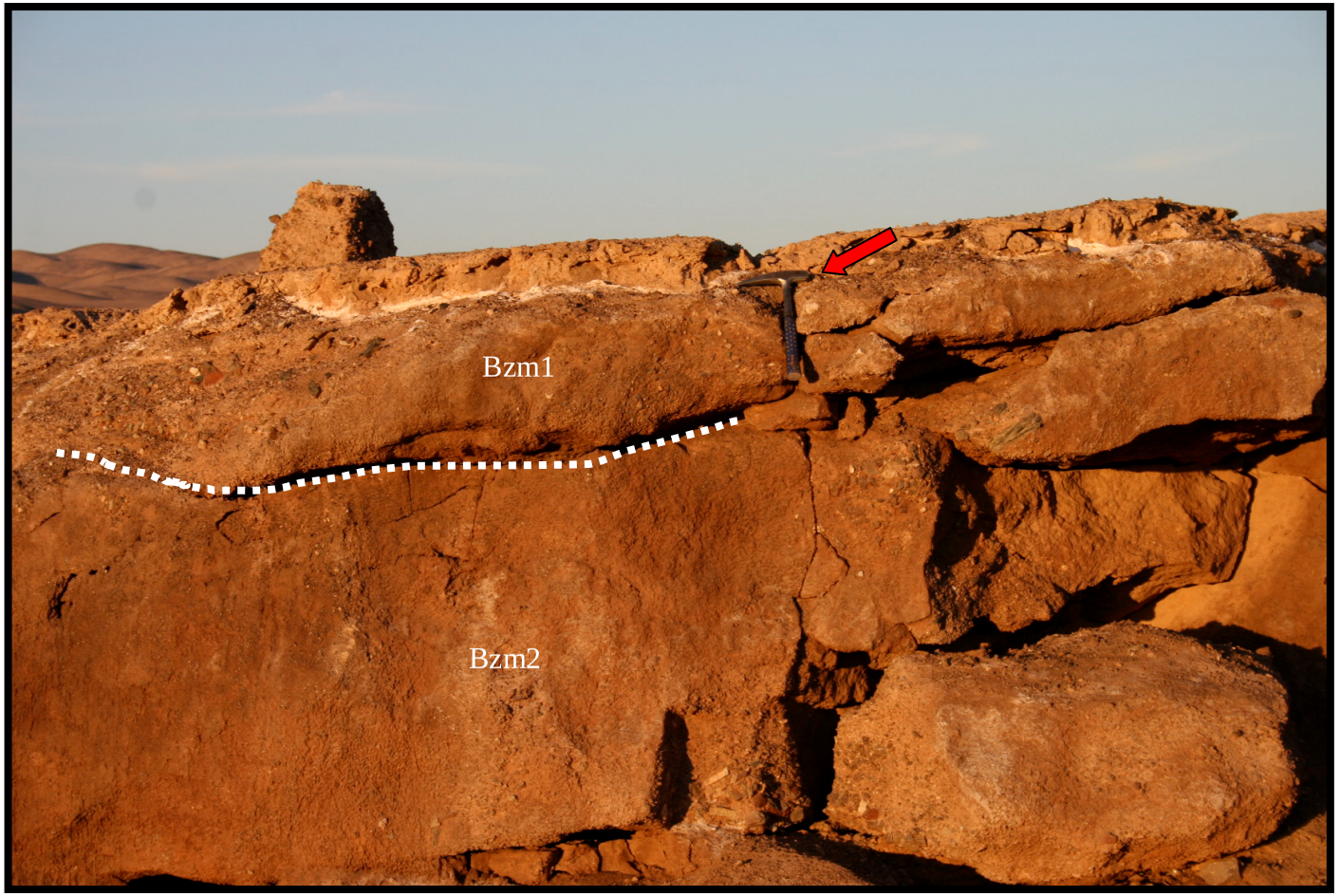

Figure 3.5. Field photo of soil profile at OE site. Note visible boundary (white salt layer) at unconsolidated and massive horizon contact. Rock hammer (red arrow) marking horizontal contact and for scale. Massive horizons are labeled with approximate horizon boundary (dashed white line), see figure 3.6A for unconsolidated horizon boundaries.

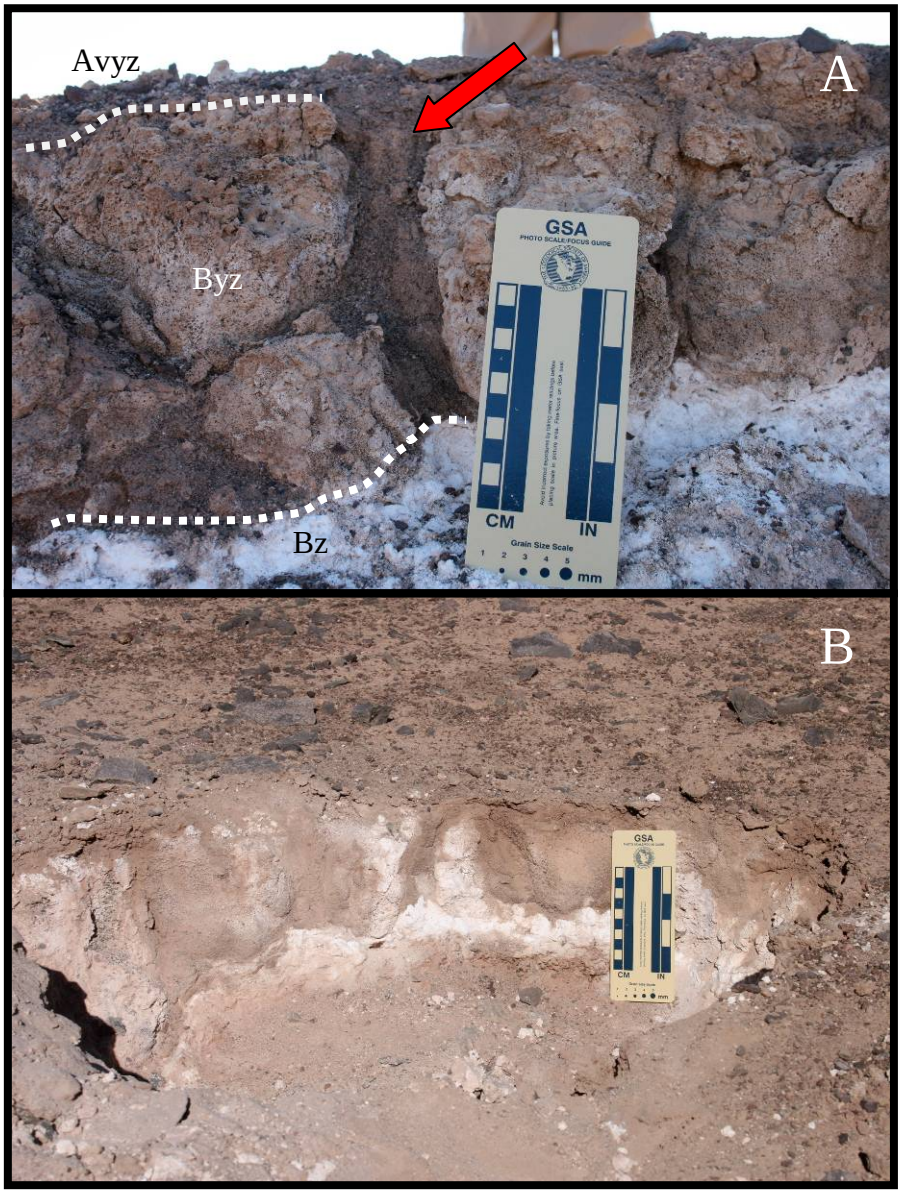

Figure 3.6. A) Close-up of upper three unconsolidated horizons from outcrop face with approximate horizon boundaries, note small vertical cracks infilled with laminae of sediment (red arrow). **B)** Unconsolidated horizons exposed in shallow pit exhumed for sampling; also note weak desert pavement on this undisturbed surface. GSA (10 cm) photo cards for scale.

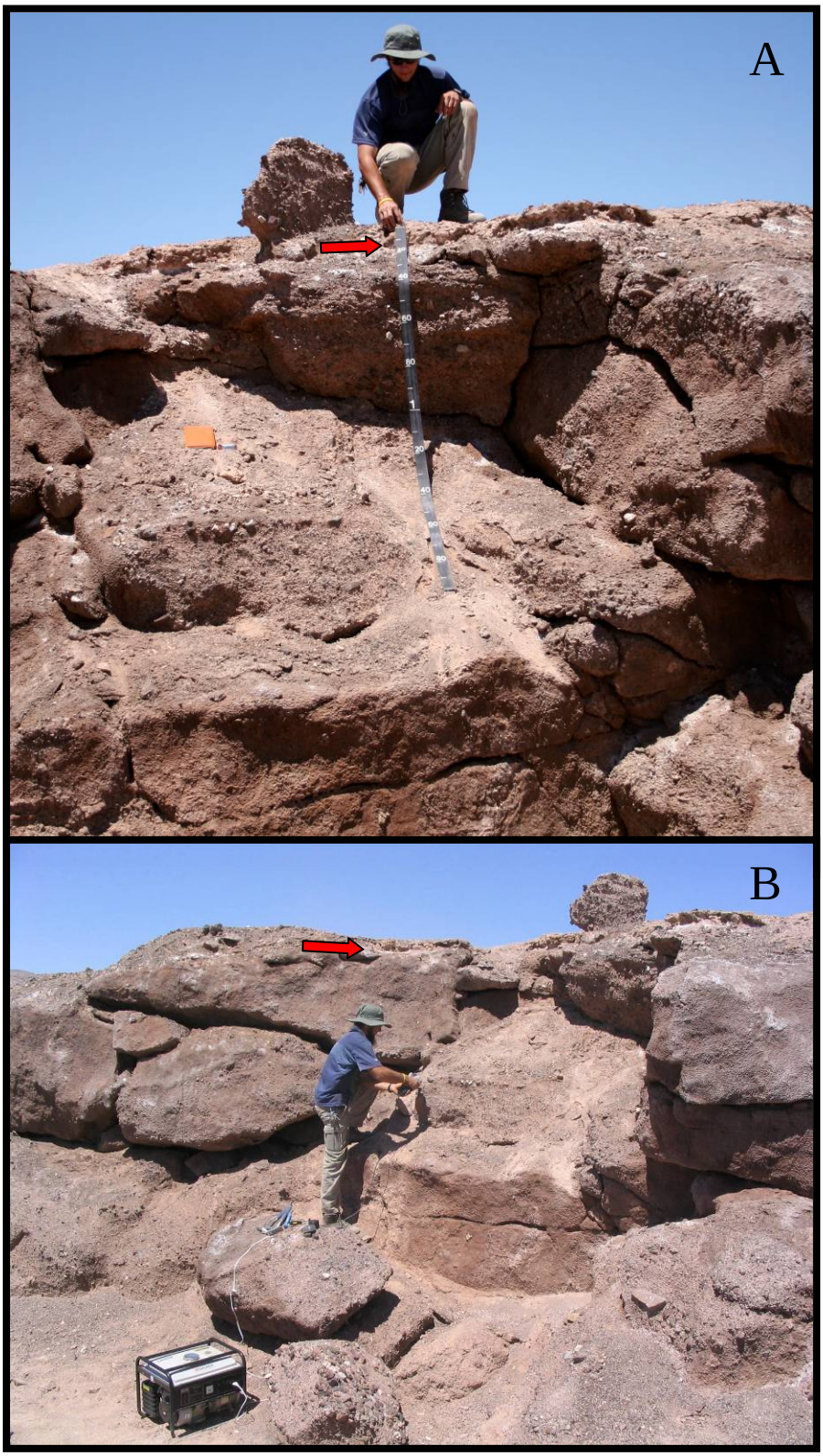

Figure 3.7. A) Measuring OE profile with 2 m tape. **B)** OE profile looking NE, author (1.87 m height) for scale. Massive horizons below red arrows.

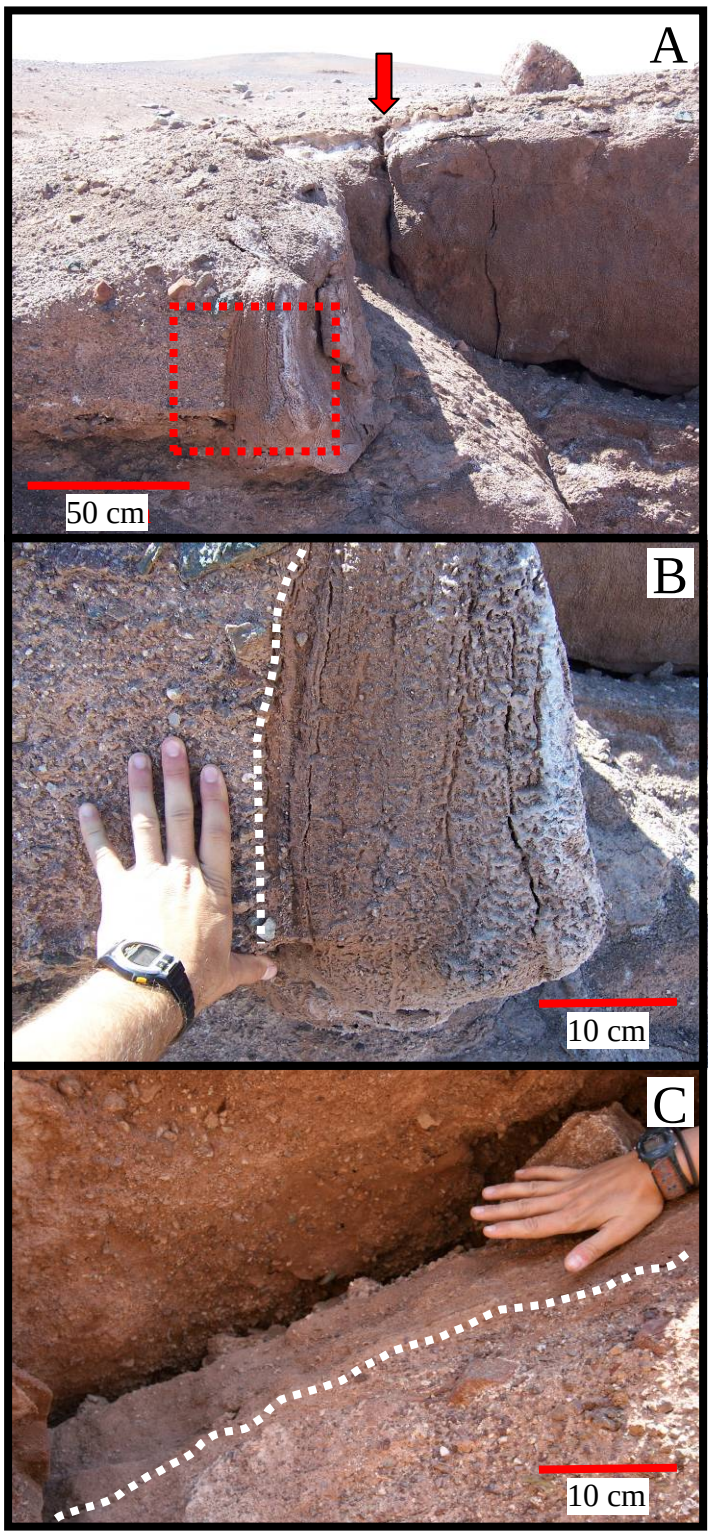

Figure 3.8. **A)** Large vertical soil crack at OE site, note how it cuts through all horizons (red arrow); red box is inset for figure 17B. **B)** Close up of soil crack, note vertical laminae (right of white line). **C)** Horizontal laminae in indurated horizon (above white line).

observed filling most, but not all of the cracks in their respective orientations (Buck et al., 2006b).

Avyz Horizon

The surface layer was characterized as a weakly vesicular A horizon with gypsum and other soluble salts (Figures 3.3, 3.4, and 3.6, Table 9; Appendix). This horizon is ~ 2 cm thick and has a weak, pink (7.5 YR 7/3-7.5 YR 6/3), and slightly effervescent surface crust (upper 1 mm) atop a light brown moderately effervescent base (Figure 3.9). Average pH/EC for the Avyz is 8.03 and 14 dS/m respectively (Table 2). Texturally this soil horizon is a loam with a salt content of 13% by weight (Table 3). Salt minerals were not identified distinctly in petrographic or SEM analyses since they could not be differentiated amongst the high percentage of the fine earth fraction that obscured visibility and data collection (Figures 3.9-3.11). However, elemental spectrums acquired with EDS analyses indicate halite and gypsum in the soil micromass adjacent to igneous grains and vesicles (Figures 3.9-3.12). XRD analyses showed gypsum as the sole salt mineral, but the presence of halite was also noted by taste in the field (Table 6). Macro and microscopic analyses primarily reflect the horizon's predominant silicate mineralogy along with the vesicular nature responsible for the high percentage of soil voids (Figures 3.9-3.11, Table 4). Single to double spaced chitonic and porphyric fabrics (Figure 3.9B, Stoops and Jongerius, 1975; Bullock et al., 1985) were most common as coarser silt/sand fraction of parent material grains/clasts were suspended in a fine-grained matrix of silt/salt/clay (micromass, e.g. Stoops and Vepraskas, 2003; undifferentiated b-fabric, e.g. Bullock et al., 1985). Illite, and kaolinite were the dominant clay minerals identified by XRD with lesser amounts of smectite and chlorite (Table 7, Figure 3.13).

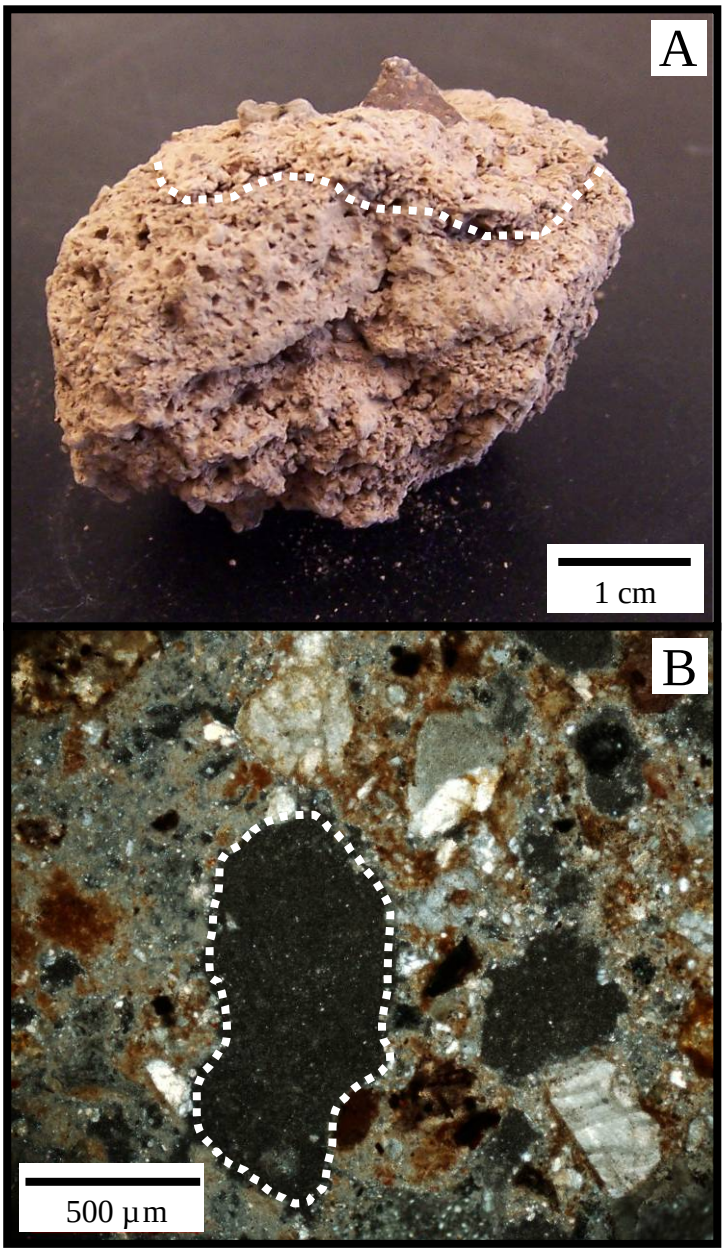

Figure 3.9. A) Image of ped from Avyz horizon, dashed white line underlines surface crust. **B)** Petrographic image (PPL) of Avyz horizon, white dashed line outlines one vesicle for reference.

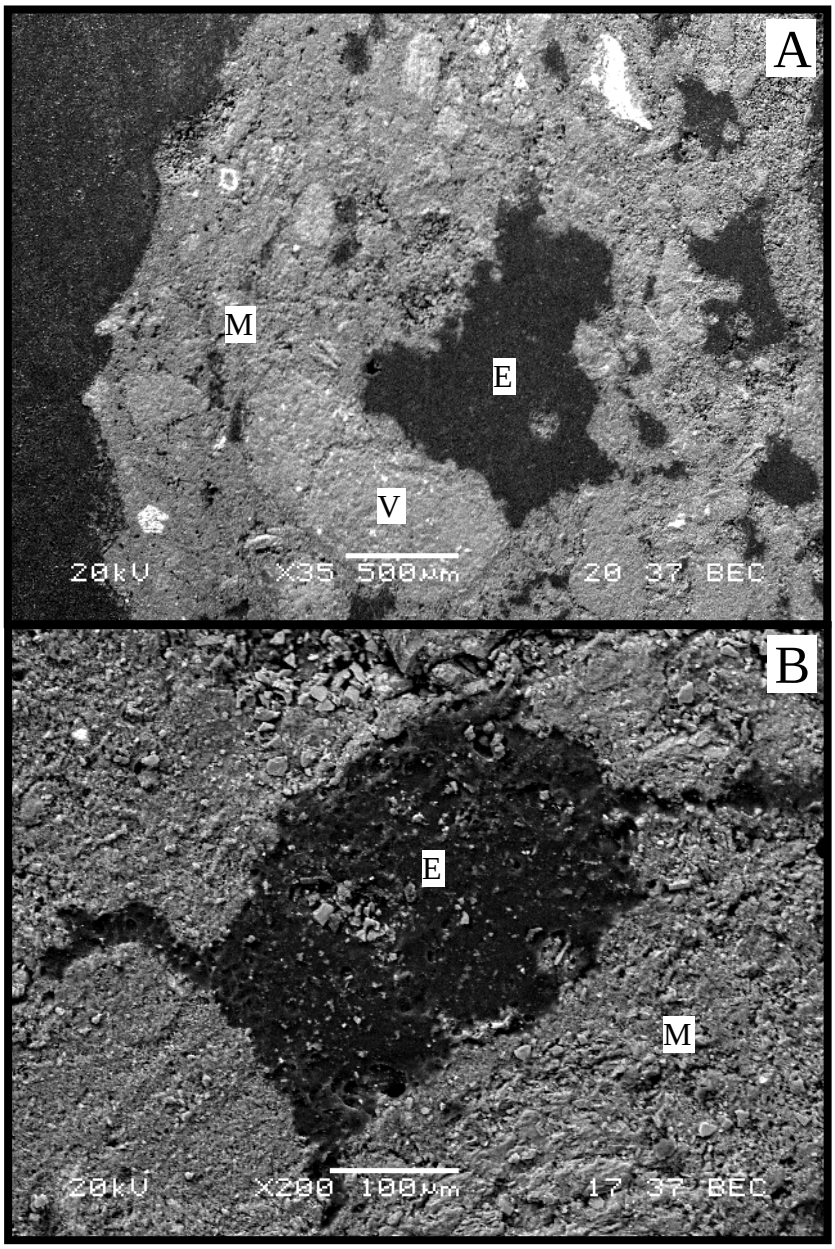

Figure 3.10. A) SEM image of Av horizon, note vesicles preserved with epoxy (E) and the difficulty distinguishing volcanic grains (V) from soil micromass (M). **B)** Close up SEM image of soil micromass and vesicle preserved with epoxy.

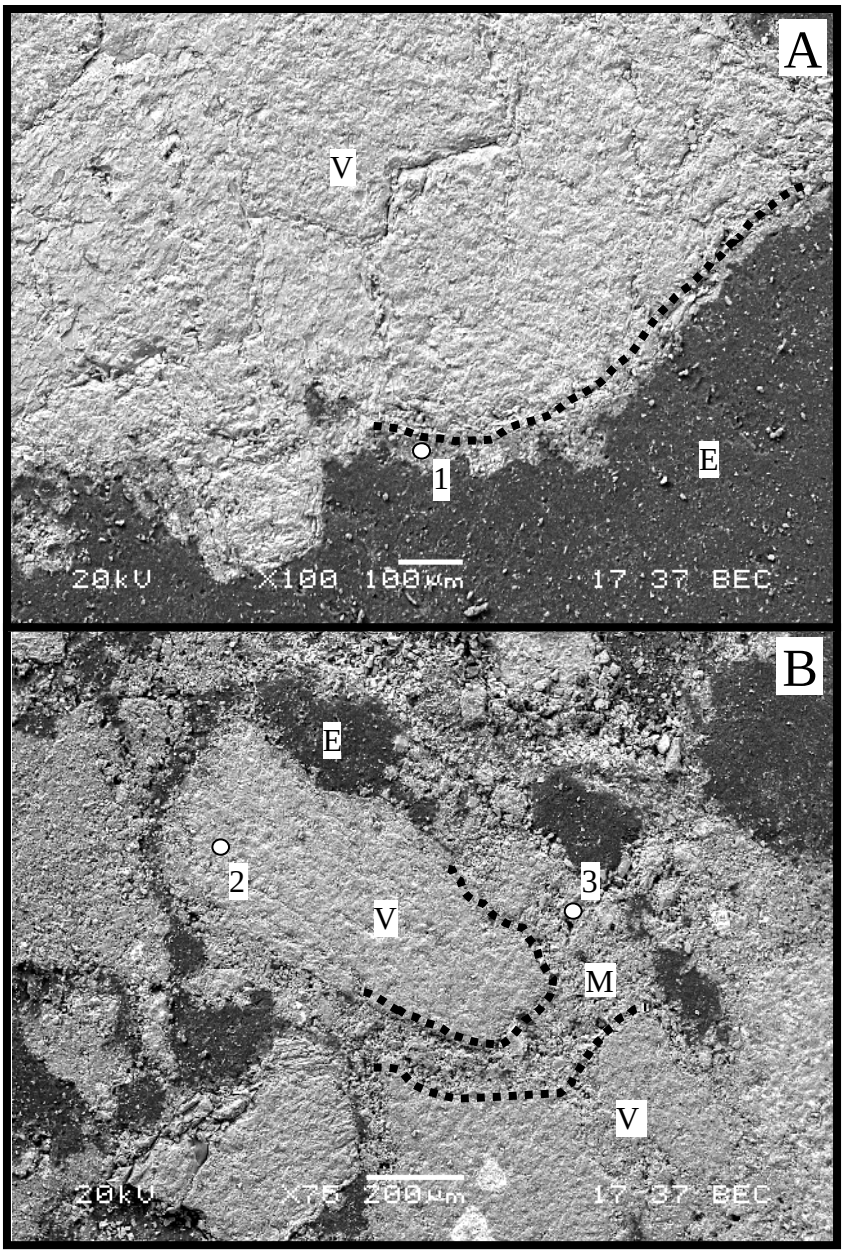

Figure 3.11. A) SEM image of thin layer of soil micromass adjacent to volcanic grain (V) and void space/epoxy (E) (dashed black line for reference). **B)** SEM image of volcanic grains amongst vesicles and soil micromass (M) (dashed black line accents subtle boundary between grains and micromass. Points 1-3 indicate location of EDS spectrum acquisition for figure 3.12.

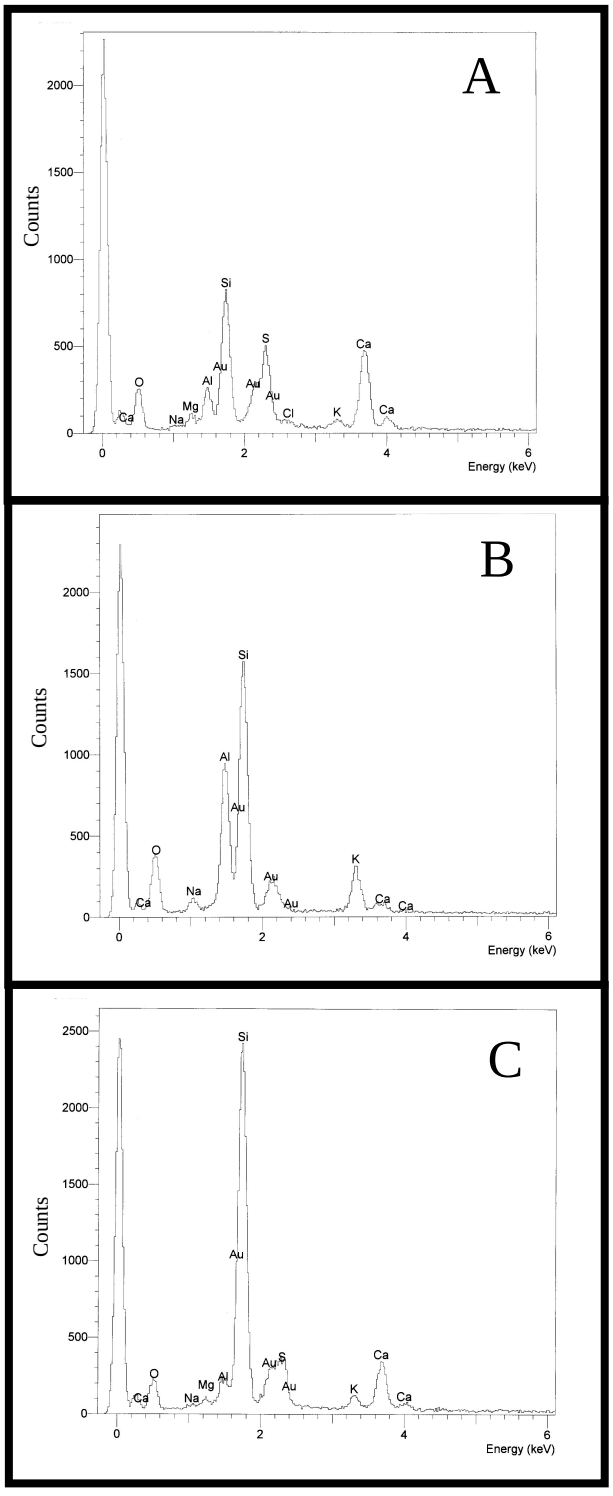

Figure 3.12. A) EDS spectrum for point1 in figure 3.11A; displays mixture of fine silicate material and $CaSO_4$ (gypsum). **B)** EDS spectrum for point 2 in figure 3.11B; volcanic clast signature. **C)** EDS spectrum for point 3 in figure 3.12B; displays mixture of fine silicate material and $CaSO_4$ (gypsum). Gold (Au) peaks are from gold coating on samples.

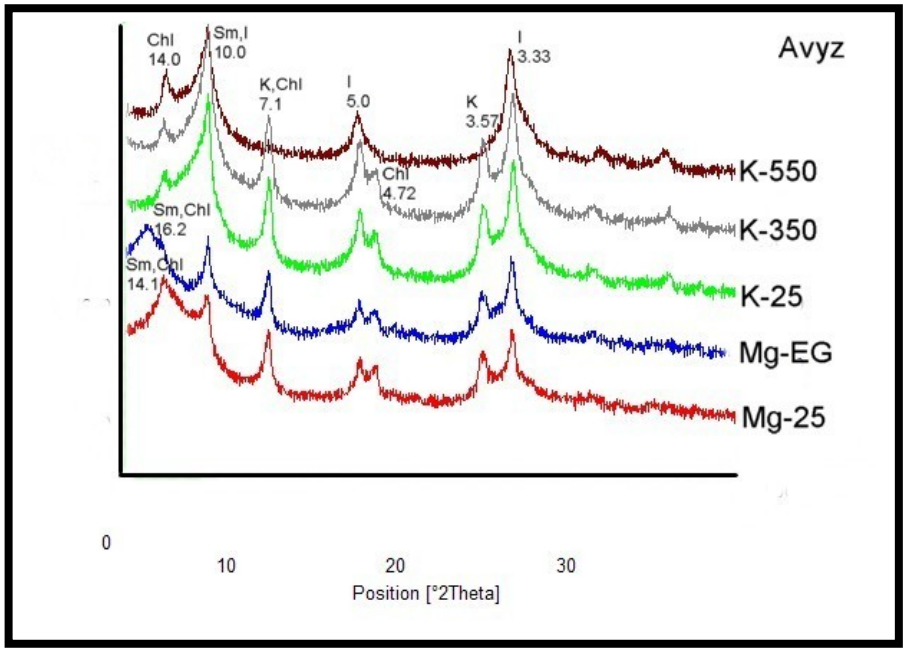

Figure 3.13. Stacked XRD diffractograms of treated samples from the Avyz horizon clay fraction at 0-2 cm depth. Sm=Smectite, Chl=Chlorite, I=Illite, K=Kaolinite; numerical d-spacing values (Table 11; Appendix) also noted with suspected mineralogy. smectite and chlorite (Table 7, Figure 3.19).

Byz Horizon

The Byz horizon is 9 cm thick and slightly to noneffervescent. Average pH/EC is 8.31 and 20 dS/m respectively. Texturally this soil horizon is a silt loam and contains as much as 71% salt by weight. Illuvial salt ($CaSO_4$) is present as Stage I snowballs, Stage II nodules, and incipient Stage III cementation in the center of coarse columnar peds (e.g. Buck and Van Hoesen, 2002). Each columnar ped is partitioned by small vertical cracks filled with sediment and salt (Figures 3.4 & 3.6). The color of this horizon was highly variable depending upon salt concentration and proximity to soil cracks, but varied from white to brown (2.5 YR 8/1-7.5 YR 5/4) (Figures 3.3, 3.6, and 3.14). XRD analyses reveal that there are three $CaSO_4$ minerals (gypsum/ bassanite / anhydrite) contributing to

Figure 3.14. Photo of semi-intact Byz horizon ped illustrating incipient Stage III salt (anhydrite) accumulation in the center of columnar peds; note small volcanic grains (red arrow) and salt shattered (dashed black line) volcanic clast.

the salt content depending on the location within the horizon. Gypsum is most common inside the vertical cracks, bassanite occurs more commonly along the ped edges and anhydrite dominates the interior of the columnar peds (Table 6). SEM/EDS analyses do not readily elucidate the difference in hydration water that distinguishes some salt minerals (Buck et al., 2006a). In addition, the mostly anhedral crystals habits made definitive identification in petrographic scope and SEM/EDS difficult (Figure 3.15). However, anhedral to euhedral lenticular (lozenge-like) or prismatic $CaSO_4$ crystal habits are present (Figures 3.15, 3.17, & 3.18). Crystals are in random orientations displacing, cementing, and supporting detrital igneous grains as a salt-rich soil matrix creating an open gephuric fabric (Figure 3.18B, Stoops and Jongerius, 1975; Bullock et al., 1985). Clay mineralogy in this horizon is similar to the Avyz horizon. Illite and kaolinite are the main clay minerals identified by XRD analyses in this horizon with some contribution of smectite and chlorite (Table 7, Figure 3.19).

Bz Horizon

The Bz horizon (varies from 4 to 7 cm thick) is a loose, mostly unconsolidated (or friable), white, noneffervescent, crystalline salt layer (Figure 3.20). Salt content is >99% by weight. SEM/EDS analyses confirm the presence of thenardite, glauberite, and eugsterite as subhedral to euhedral dipyramidal, tabular/prismatic, and acicular crystals respectively (Table 5, Figures 3.21-3.24). XRD analyses identified the main constituent as thenardite and glauberite as a minor component (Table 6). Given the overwhelming salt content textural analyses were not performed on this horizon. Because clay minerals were assumed to be absent, their identification via XRD was also not undertaken. Horizon fabric was not described as only grain mounted samples were analyzed.

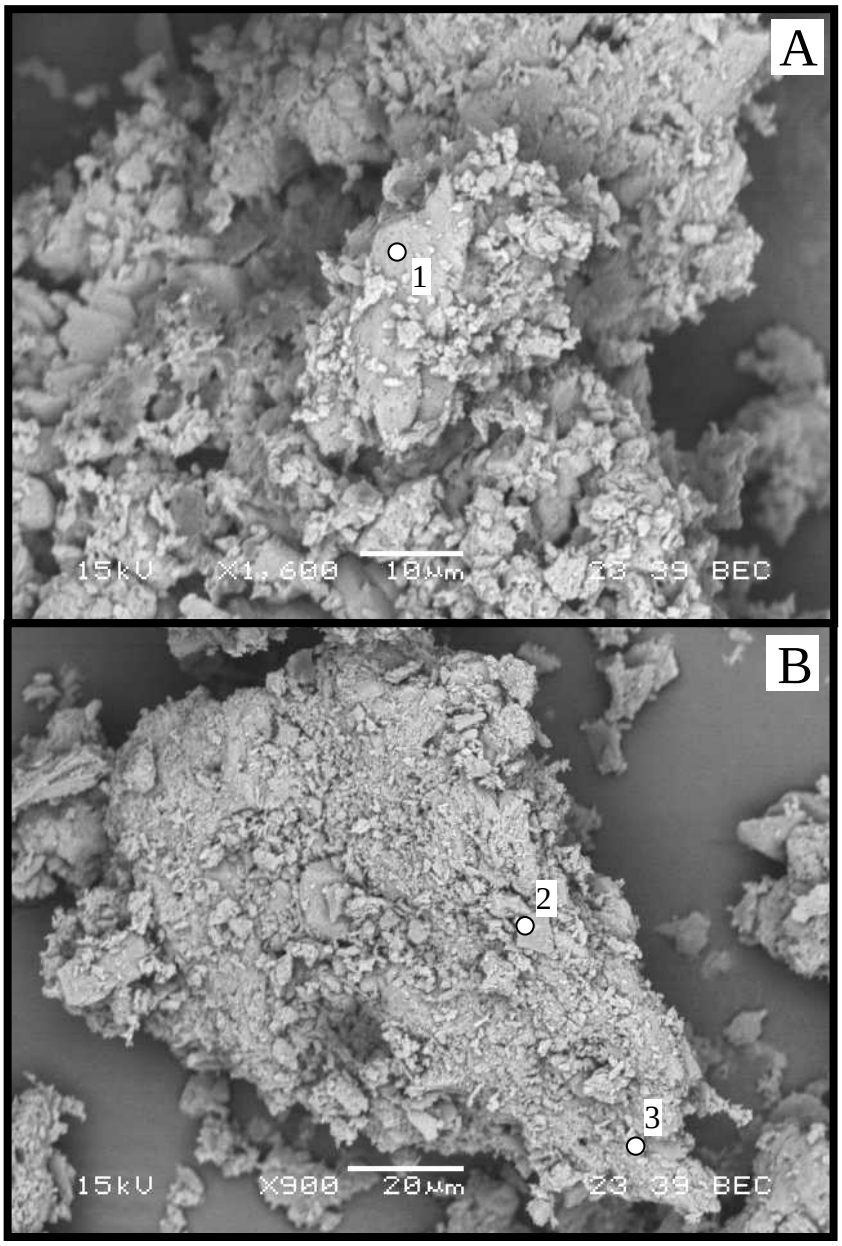

Figure 3.15. A & B) Close up SEM image of (grain mounted) anhedral gypsum/bassanite/anhydrite and silicate grain aggregates from Byz horizon. Points 1-3 indicate locations of EDS spectrum acquisition for data in figure 3.16.

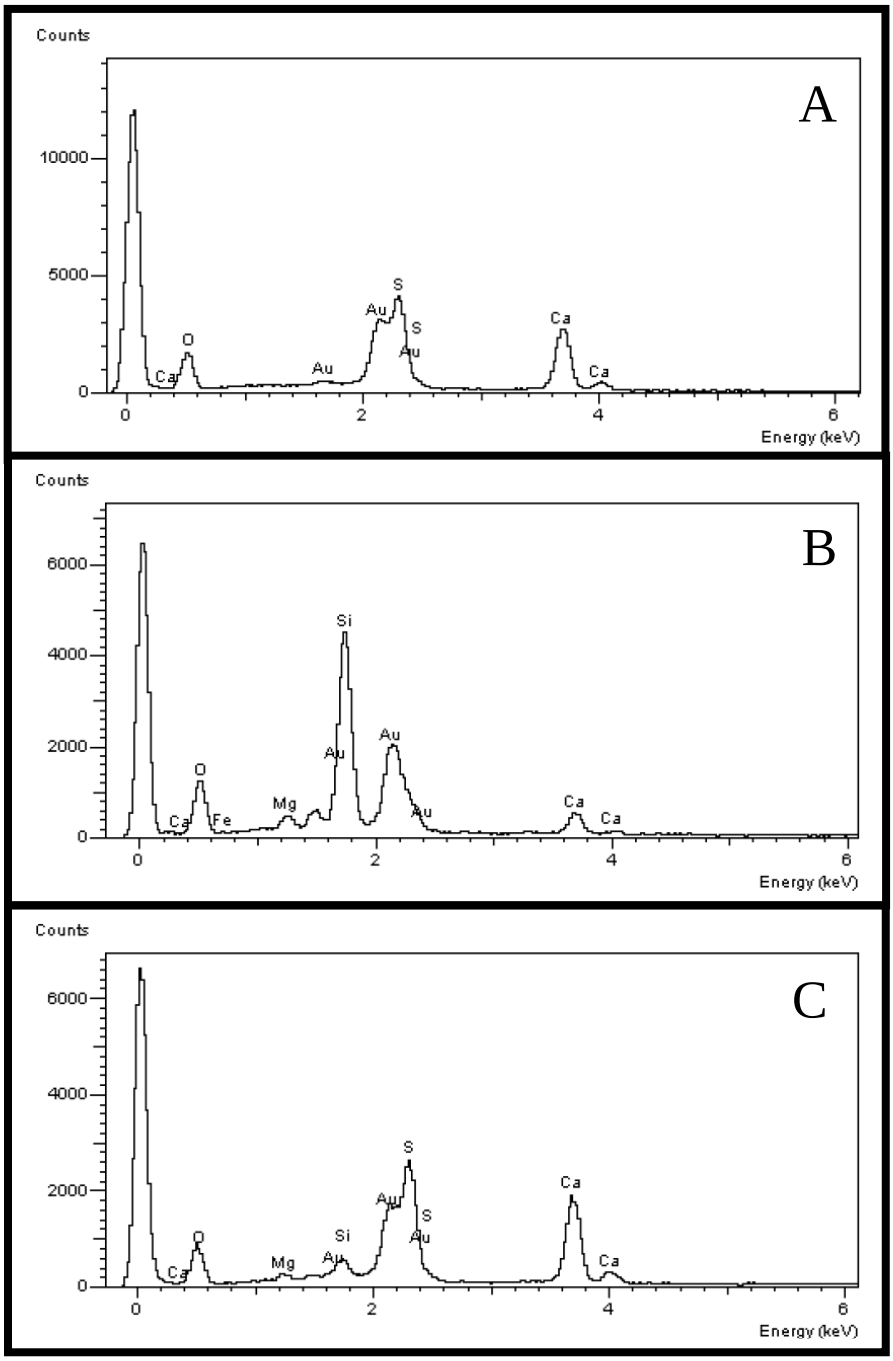

Figure 3.16. A) EDS spectrum for gypsum/bassanite/anhydrite (Ca-S-O peaks) from point 1 in figure 3.15A. **B)** EDS spectrum for silicate mineral (Si-Ca-Mg-Fe peaks) from point 2 in figure 3.15B. **C)** EDS spectrum for silicate grain coated in $CaSO_4$ (gypsum/bassanite/anhydrite) from point 3 in figure 3.15B. Gold (Au) peaks are from gold coating on samples.

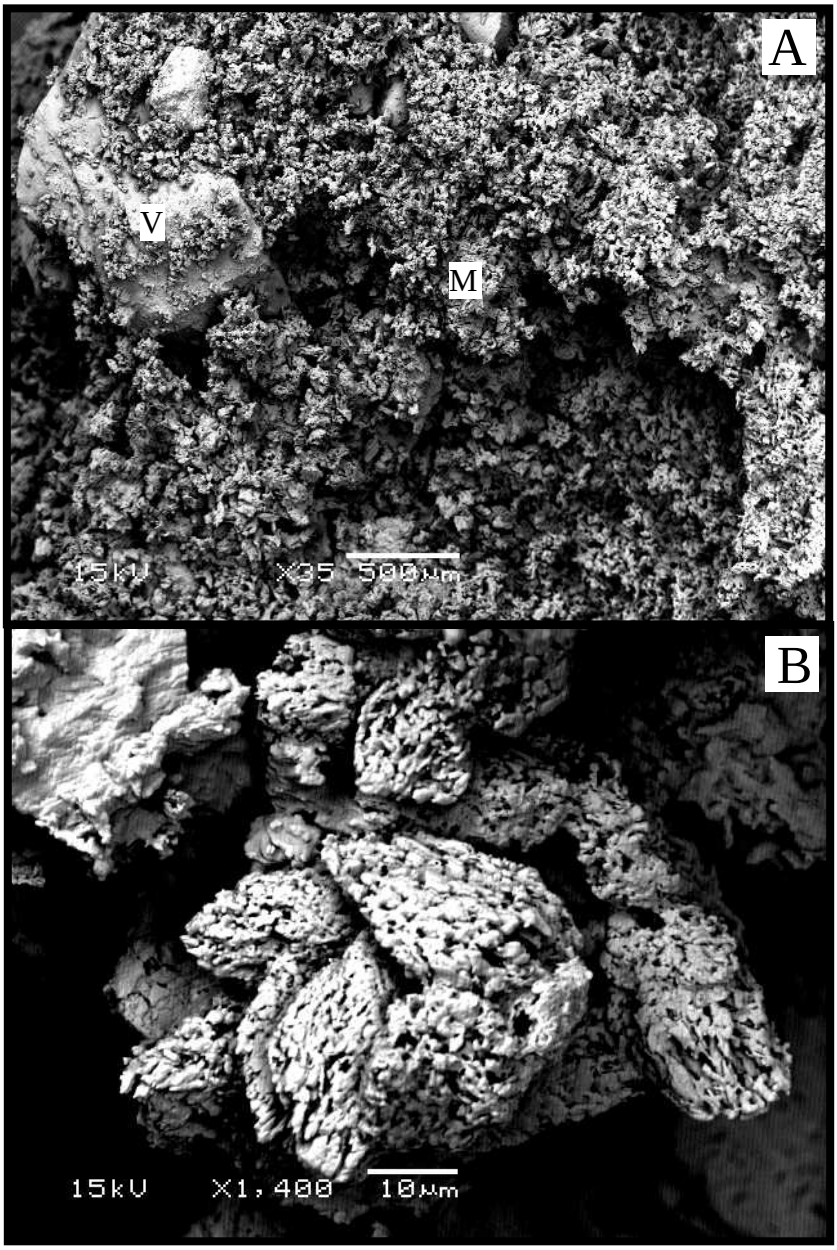

Figure 3.17. A) SEM image of volcanic grain (V) in gypsum/bassanite/anhydrite-rich soil matrix (M) from grain mounted fragment of Byz horizon. **B)** Close up SEM image of skeletal lozenge-like subhedral/euhedral gypsum/bassanite/anhydrite in Byz soil matrix; likely altered by subsequent hydration/dehydration reactions.

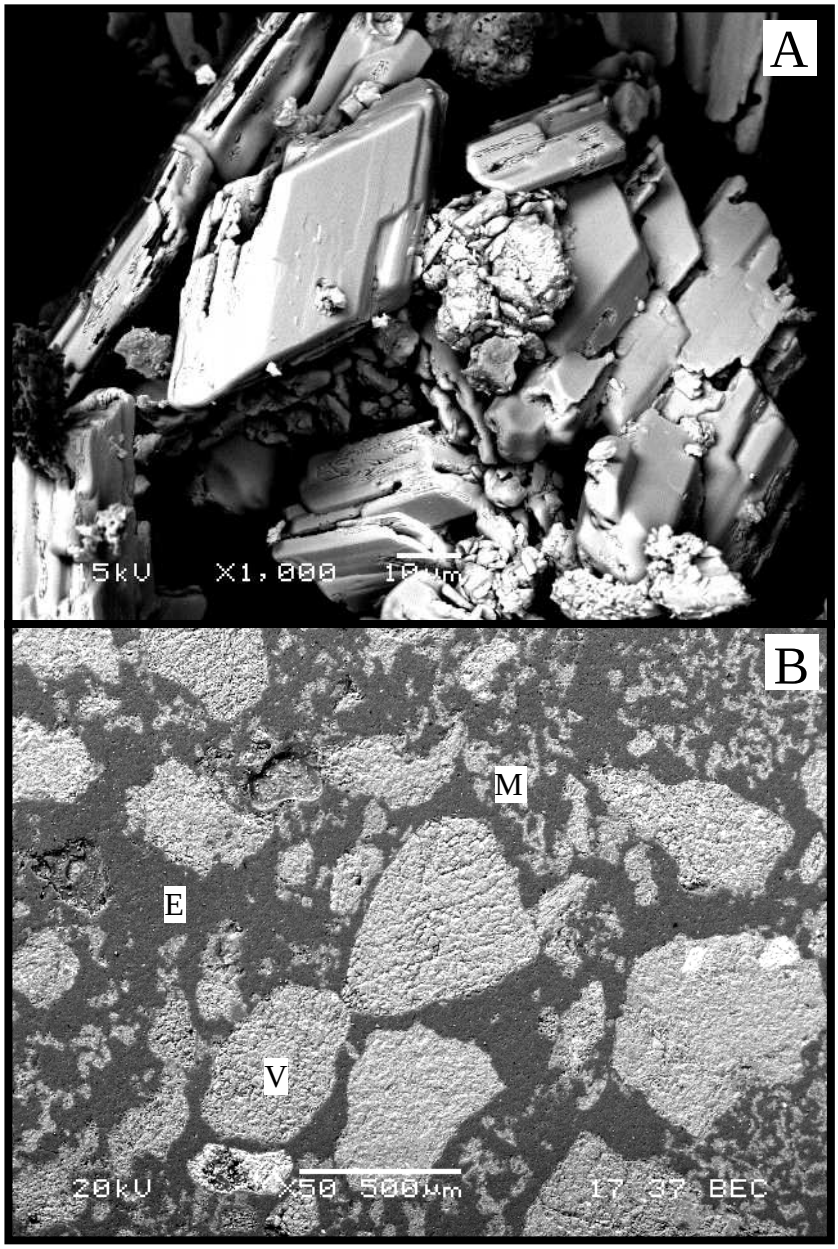

Figure 3.18. A) Close up SEM image of euhedral skeletal prismatic gypsum/bassanite/ anhydrite observed in snowball type accumulation in Byz horizon. **B)** SEM image of volcanic grains (V), gypsum/bassanite/anhydrite-rich soil matrix (M), and voids preserved with epoxy (E) from Byz horizon thin section; note open gefuric fabric illustrated by salt matrix bracing coarser volcanic grains.

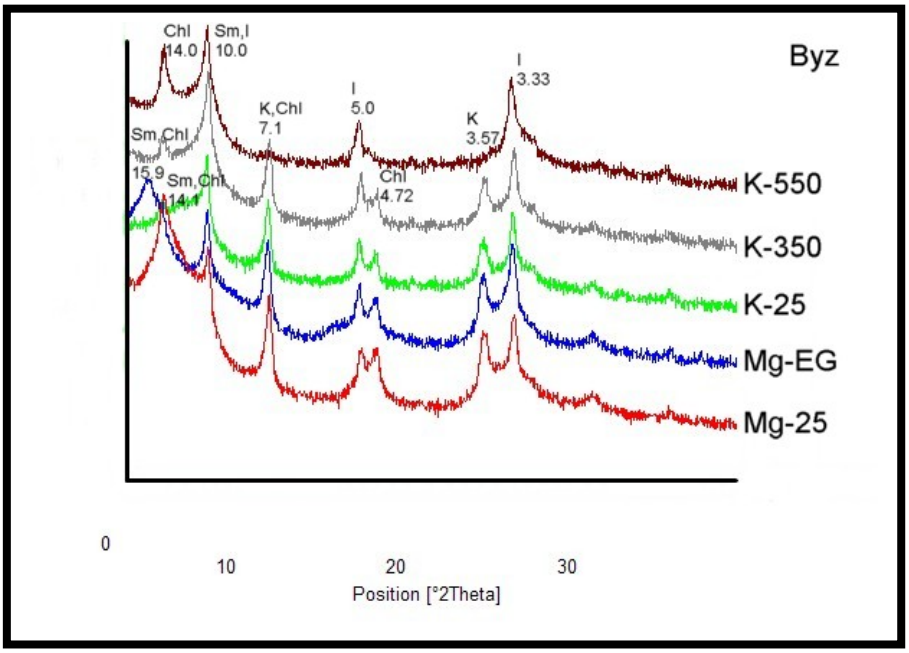

Figure 3.19. Stacked XRD diffractograms of treated samples from the Byz horizon clay fraction at 2-11 cm depth. Sm=Smectite, Chl=Chlorite, I=Illite, K=Kaolinite; numerical d-spacing values (Table 11; Appendix) also noted with suspected mineralogy.

Bz Horizon Hydration-Temperature Experiment

The results of the supplementary experiment indicate that when hydrated the >99% crystalline thenardite layer (Bz horizon) swells and transforms into a gel-like state, which contemporaneously increases in temperature rapidly (Figure 3.25, Table 8). Average temperature increase was 13.8° C (56.8° F). A maximum temperature of 31°C (87.8° F) was achieved as rapidly as 45 seconds, but the average time for run-specific high temperature was 2.3 minutes (138 seconds). At approximately the 10 minute mark of each run the salt began to precipitate in the form of a surface seal on the primarily gel-like sample. Also, after the 60 minute run time, sample temperatures still had not returned to ambient laboratory temperature/original sample temperature. Even though this experiment was only timed for one hour, the samples were stored overnight in a sealed

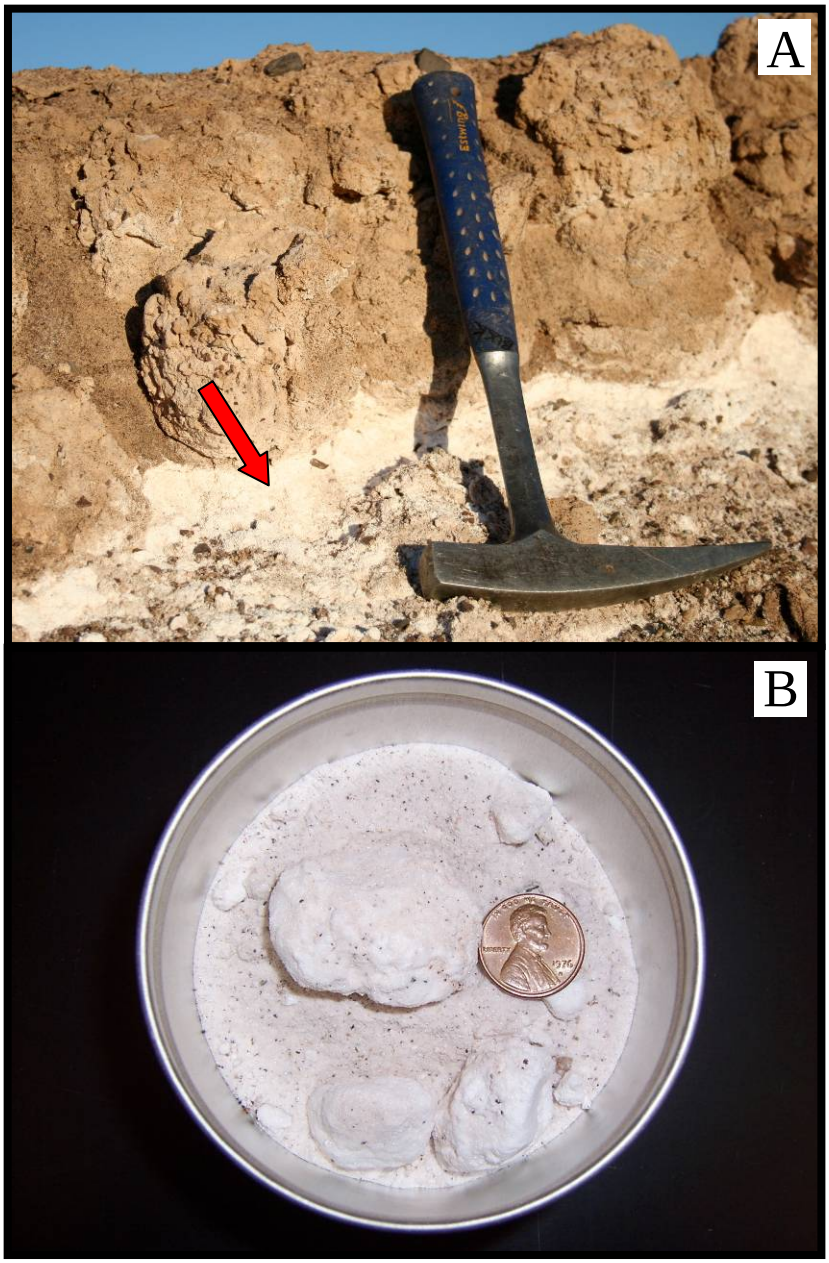

Figure 3.20. A) Field photo of Bz horizon (white thenardite layer, red arrow), head of hammer (18 cm) for scale. B) Photo of loose Bz horizon sample (pre-analyses) in metal sample tin, coin for scale; note small percentage of volcanic grains (dark specs).

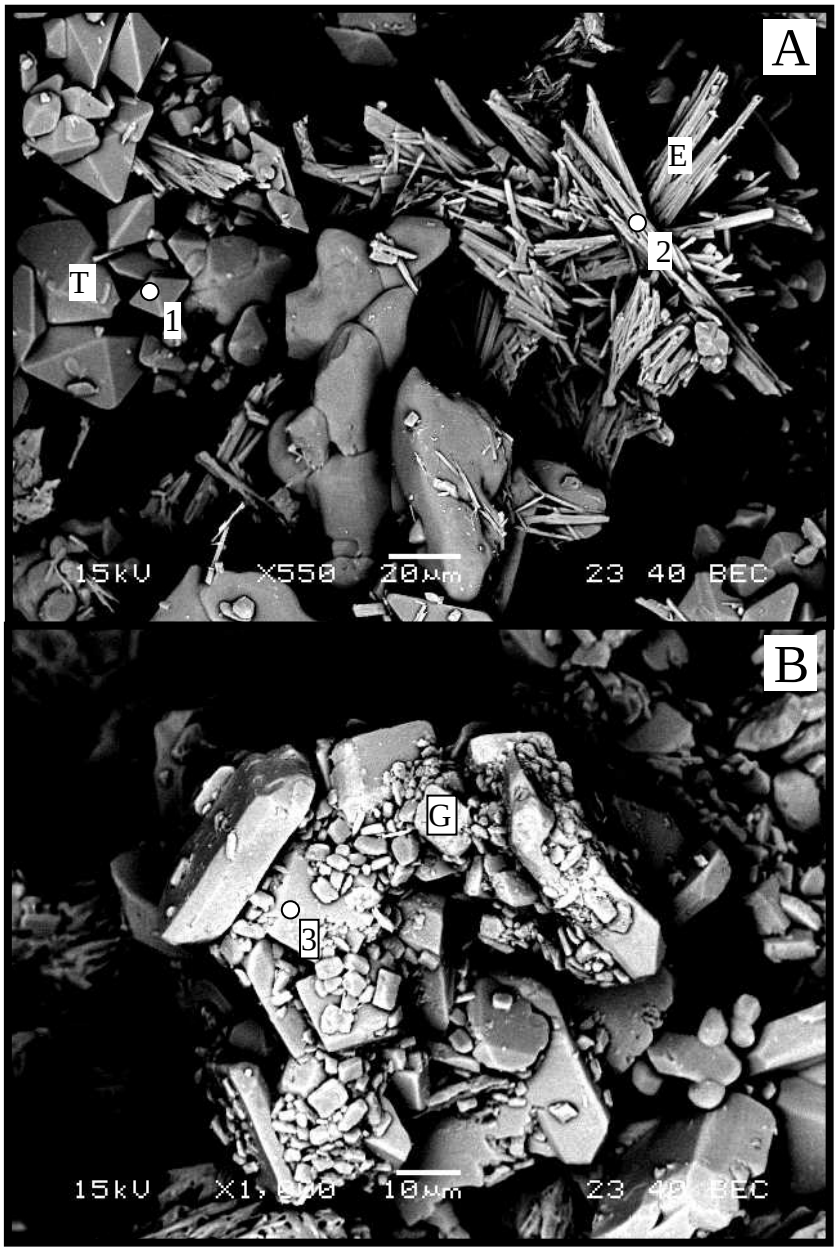

Figure 3.21. A) SEM image of grain mounted subhedral and euhedral dipyramidal thenardite (T) with euhedral acicular eugsterite (E). **B)** SEM image of a grain mounted cluster of euhedral tabular/prismatic glauberite (G). Points 1-3 indicate location of EDS spectrum acquisition for data in figure 3.24A-C respectively.

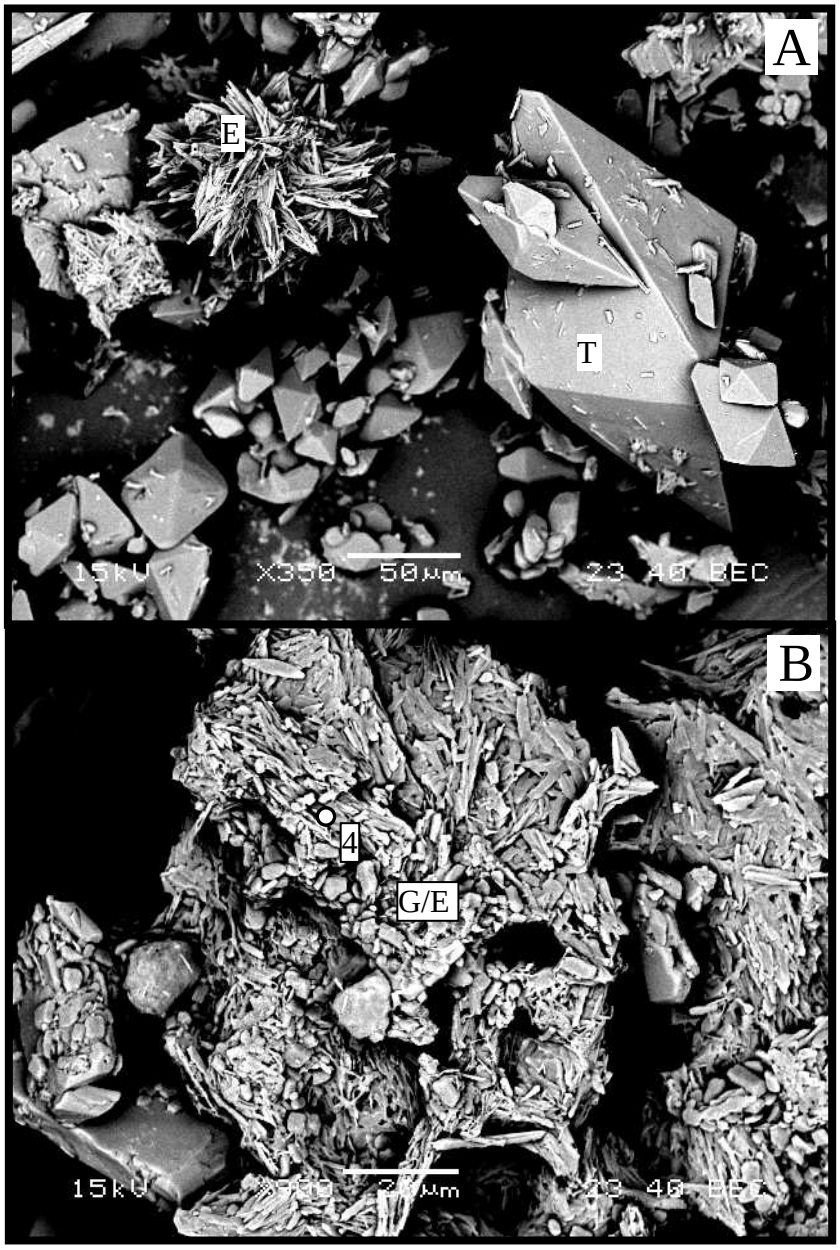

Figure 3.22. A) SEM image of euhedral dipyramidal thenardite (T) and euhedral acicular eugsterite (E). **B)** SEM image of a cluster of subhedral glauberite/eugsterite (G/E); point 4 indicates location of EDS acquisition data in figure 3.24D.

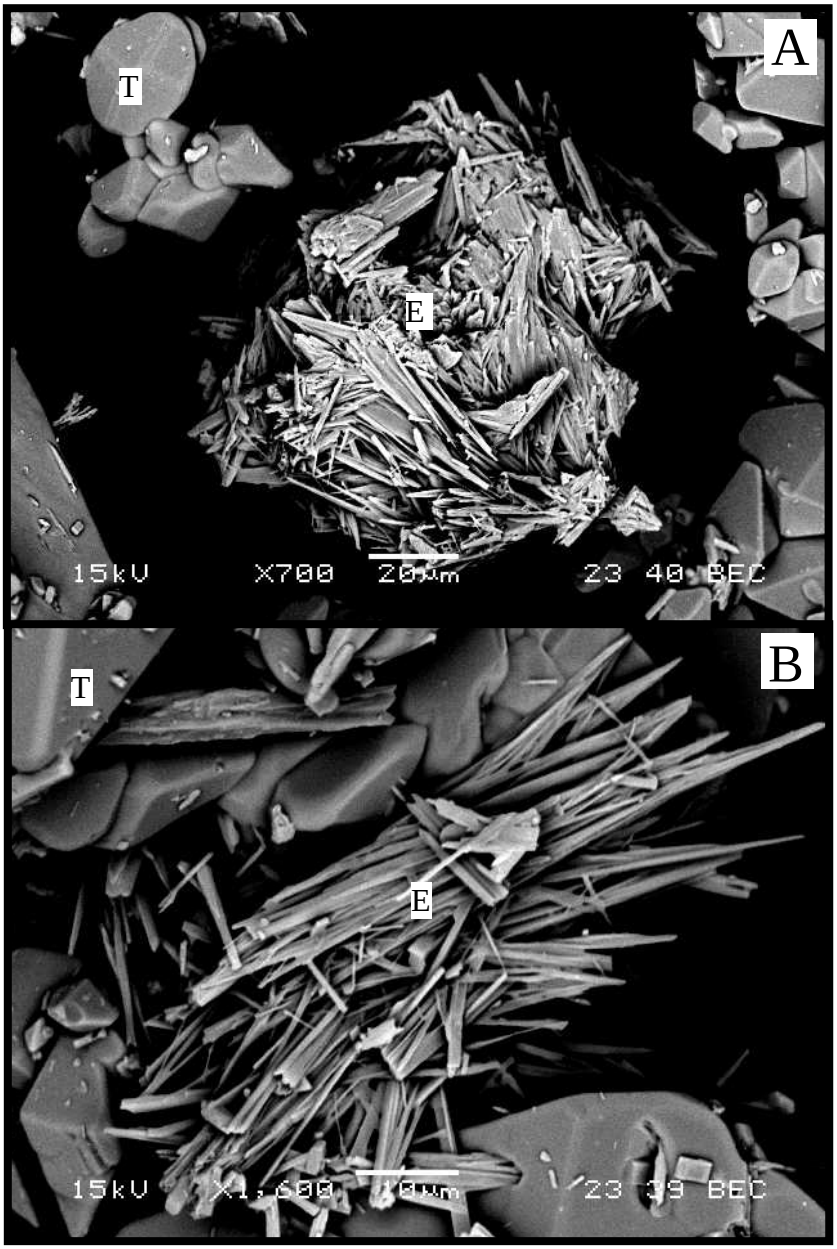

Figure 3.23. A) SEM image of a cluster of acicular eugsterite (E) crystals among euhedral thenardite (T) crystals. **B)** Close up SEM image of acicular eugsterite among euhedral thenardite.

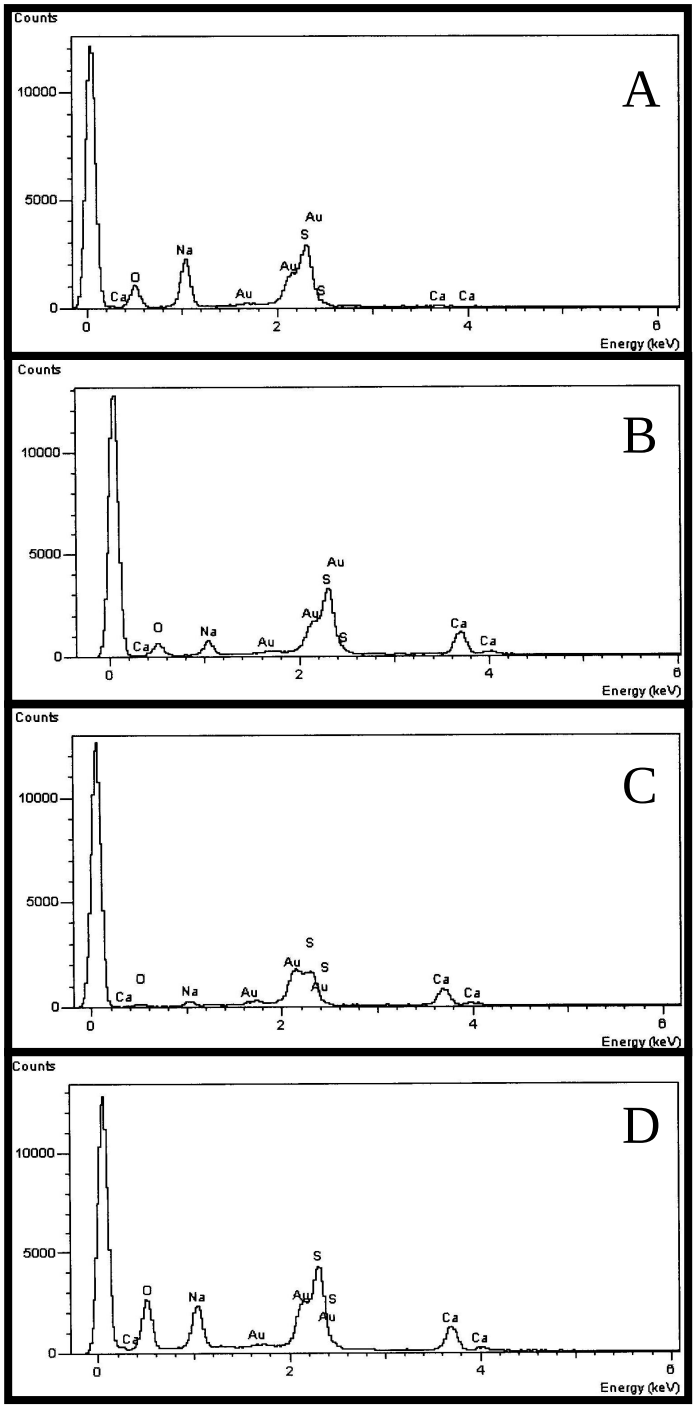

Figure 3.24. A) EDS spectrum for thenardite (Na-S-O peaks) from point 1 in figure 3.21A . **B)** EDS spectrum for eugsterite (Na-Ca-S-O peaks) from point 2 in figure 3.21A. **C)** EDS spectrum for glauberite (Na-Ca-S-O peaks) from point 3 in figure 3.21B. **D)** EDS spectrum for glauberite/eugsterite (Na-Ca-S-O peaks) from point 4 in figure 3.22B. Gold (Au) peaks are from gold coating on samples.

vacuum chamber, with dessicant, and examined the following day. All samples were no longer warm to the touch and most had completely crystallized in their respective beakers. One sample still had a gel-like salt solution preserved in the center of crystallized salt.

Bzm1 Horizon

The Bzm1 horizon (~23 cm thick) was characterized as a unit of poorly sorted coarse sand and gravel clasts (1-8 cm in length) suspended in a slightly to noneffervescent pinkish grey (7.5 YR 6/2-7/2) matrix of fine earth and well cemented by illuvial (stage III+) soluble salts (Figure 3.26) including halite, nitratine, glauberite, thenardite, and darapskite (Tables 5 & 6). Average pH/EC is 7.64 and 84 dS/m respectively (Table 2). Texturally this horizon ranges from a very gravelly silt loam to very gravelly sandy loam with a salt content that ranges from 42 to 51% by weight (Table 3). Bulk density measures 2.18 g/cm^3 (Prellwitz, 2007). Petrographic analyses indicate that soil voids account for 17% of this horizon (Table 4) despite the noticeably indurated nature due to high salt content. SEM/EDS and XRD analyses indicate the presence of halite, glauberite, and thenardite (Tables 5 & 6). Nitratine and darapskite were identified only in XRD analyses. SEM analyses display halite, glauberite, and thenardite as irregular/ anhedral masses (>100µm) or interstitial cement (Figures 3.27-3.29). Some shattered/displaced volcanic / plutonic grains are also seen preserved by the saline cement as salt minerals have previously penetrated incipient clast fractures to degrade the parent material grains/clasts into smaller angular fragments (Figure 3.28). This translates to a single to double-spaced gefuric and porphyric fabric as igneous grains or fragments are matrix supported by bridging or indurating salt constituents (Figures 3.27-3.29, Stoops

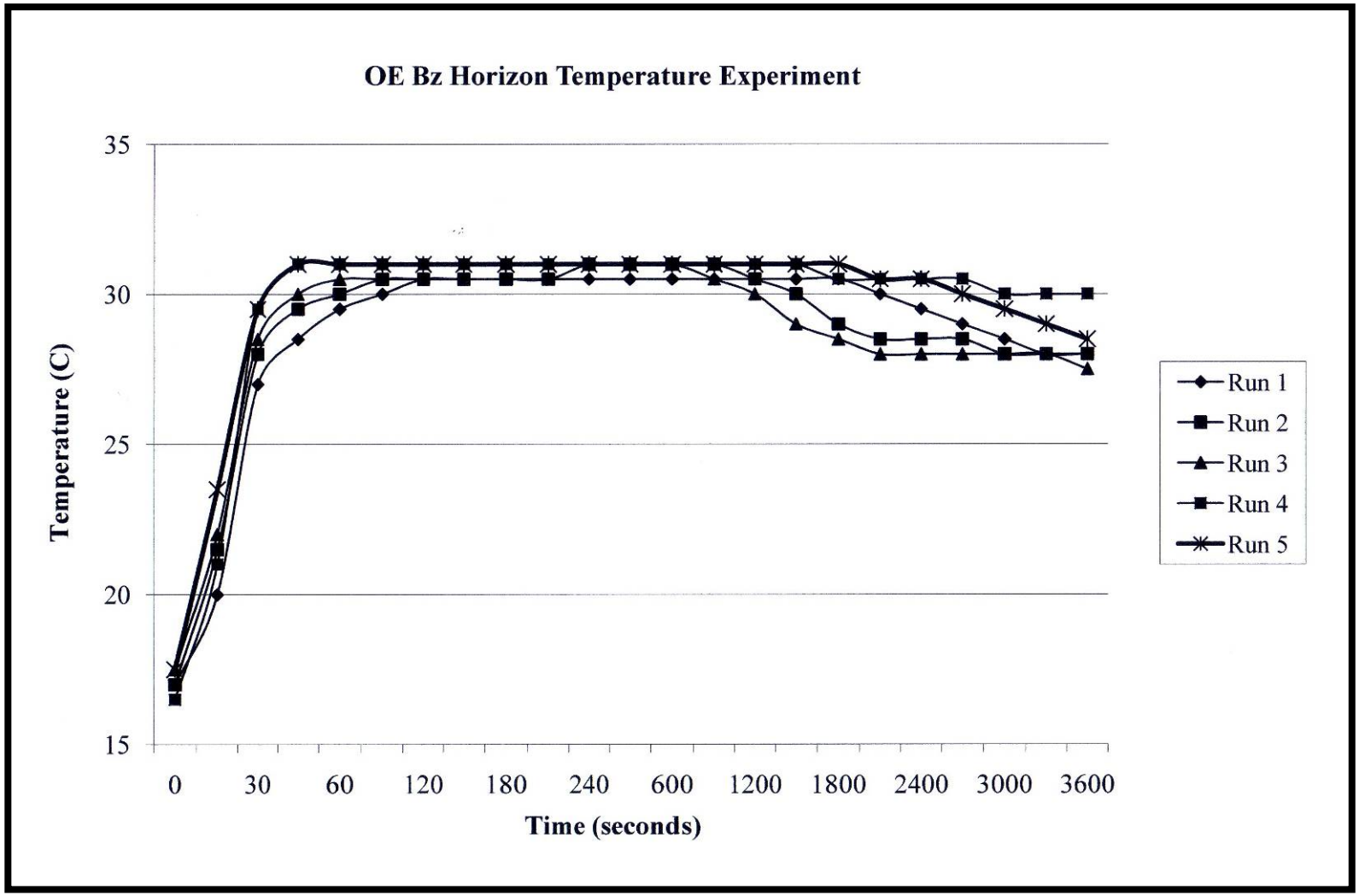

Figure 3.25. Graphic results from Bz horizon hydration-temperature experiment. Data point measurements provided in Table 8.

TABLE 8. Bz HYDRATION-TEMPERATURE DATA

Time (seconds)	Temperature (°C)				
	Run 1	Run 2	Run 3	Run 4	Run 5
0	17.0	17.0	17.5	16.5	17.5
10	20.0	21.5	22.0	21.0	23.5
30	27.0	28.0	28.5	29.5	29.5
45	28.5	29.5	30.0	31.0	31.0
60	29.5	30.0	30.5	31.0	31.0
90	30.0	30.5	30.5	31.0	31.0
120	30.5	30.5	30.5	31.0	31.0
150	30.5	30.5	30.5	31.0	31.0
180	30.5	30.5	30.5	31.0	31.0
210	30.5	30.5	30.5	31.0	31.0
240	30.5	31.0	31.0	31.0	31.0
300	30.5	31.0	31.0	31.0	31.0
600	30.5	31.0	31.0	31.0	31.0
900	30.5	31.0	30.5	31.0	31.0
1200	30.5	30.5	30.0	31.0	31.0
1500	30.5	30.0	29.0	31.0	31.0
1800	30.5	29.0	28.5	30.5	31.0
2100	30.0	28.5	28.0	30.5	30.5
2400	29.5	28.5	28.0	30.5	30.5
2700	29.0	28.5	28.0	30.5	30.0
3000	28.5	28.0	28.0	30.0	29.5
3300	28.0	28.0	28.0	30.0	29.0
3600	28.0	28.0	27.5	30.0	28.5

Figure 3.26. Photo of indurated sample from the Bzm1 horizon (pre-analyses). Note visible soil voids and salt minerals (white powdery material).

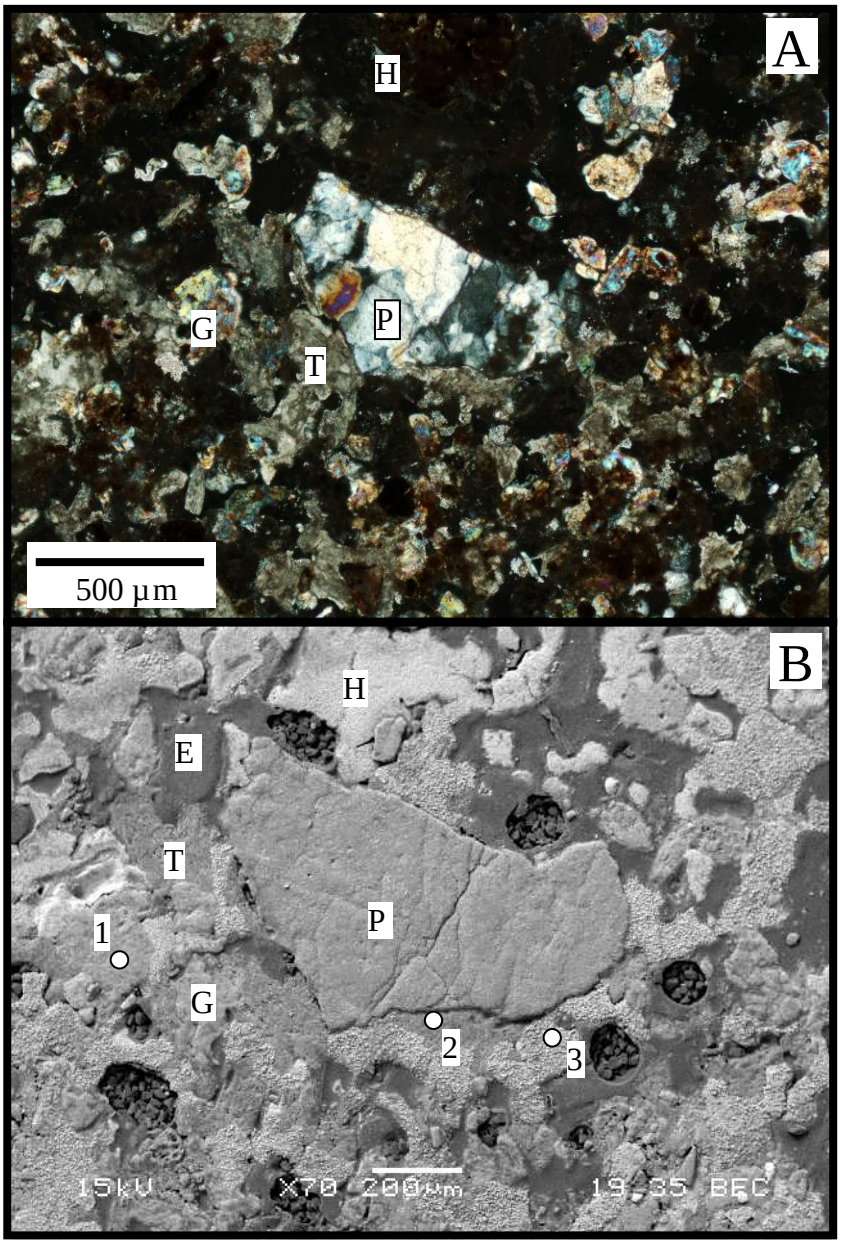

Figure 3.27. A) Petrographic photo, in XPL, of Bzm horizon; granitic grain cemented in the center (P), extinct areas contain voids but are largely halite (H), intermediate birefringence is thenardite (T), higher order birefringence is glauberite (G). **B)** SEM image of same grain in 3.26A. Note abundant soil pores preserved by epoxy (E) and incipient clast fractures in noted grain; points 1-3 indicate location of EDS spectrum acquisition for figure 3.30.

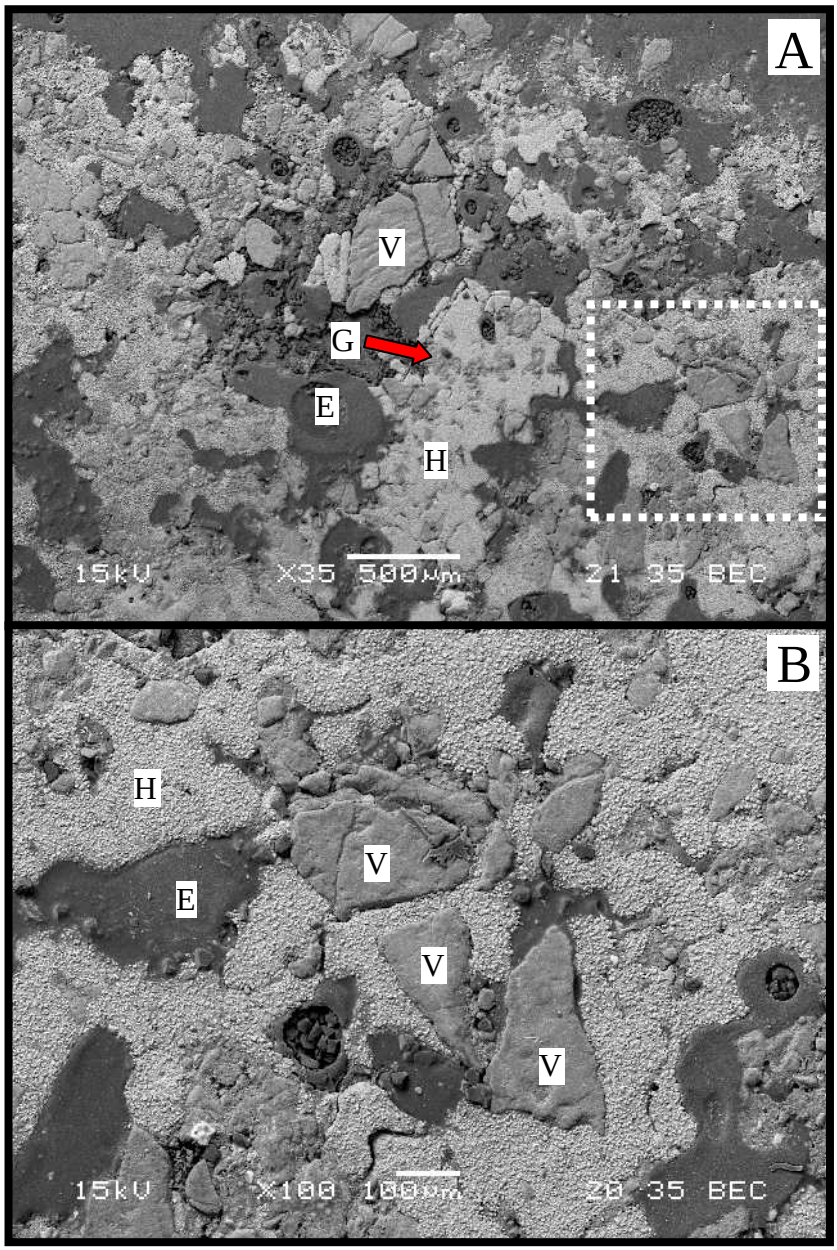

Figure 3.28. A) SEM image of Bzm1 with shattered/displaced volcanic grains (intermediate gray, V) cemented by halite (white, H) and minor glauberite (light gray, G; red arrow for emphasis), voids preserved by epoxy (E); hashed white box is area enlarged in figure 3.28B. **B)** Close up SEM image of shattered volcanic grain outlined in figure 3.28A cemented in halite.

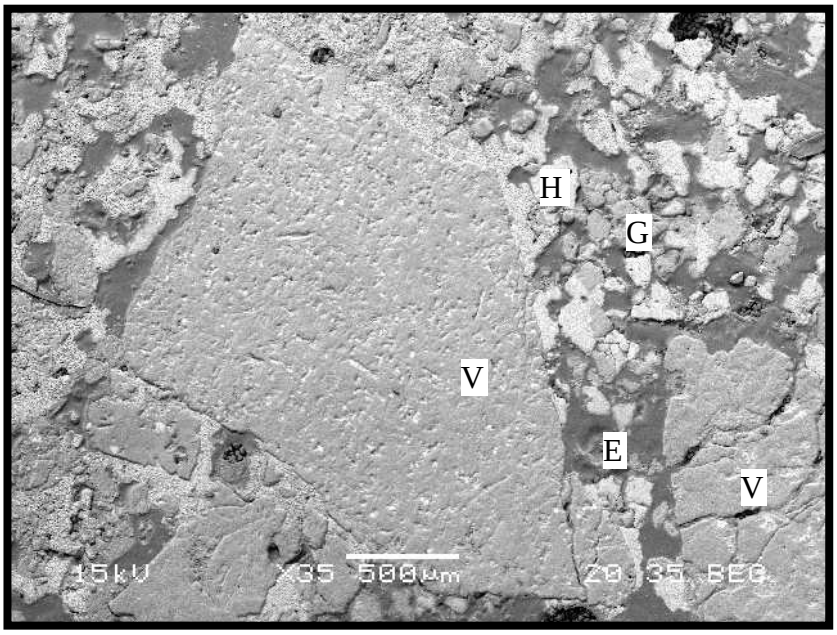

Figure 3.29. SEM image of a large shattered volcanic grain (V) along with halite (H) and glauberite (G) salt matrix bridging/cementing the fragments. Note abundant soil voids preserved by epoxy (E).

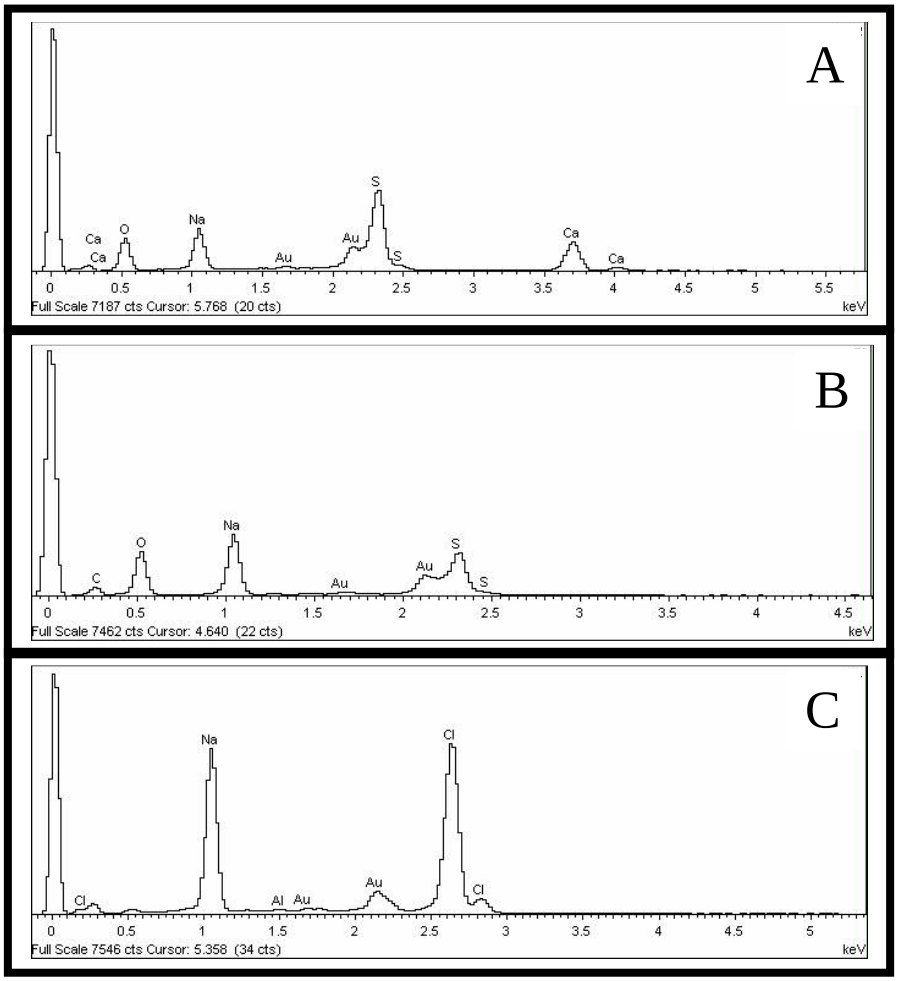

Figure 3.30. EDS spectra from points 1-3 in figure 3.27B **A)** EDS spectrum for glauberite (Na-Ca-S-O peaks) from point 1. **B)** EDS spectrum for thenardite (Na-S-O peaks) from point 2. **C)** EDS spectrum for halite (Na-Cl peaks) from point 3. Gold (Au) peaks from gold coating on samples.

and Jongerius, 1975; Bullock et al., 1985). SEM/EDS and petrographic analyses indicate that halite is the main salt mineral in this horizon (Table 5). XRD analyses indicate that nitratine is more abundant than halite in the horizontal cracks (Table 6). The clay mineralogy of this horizon is similar to the horizons above with common illite and kaolinite and minor smectite and chlorite (Table 7, Figure 3.31).

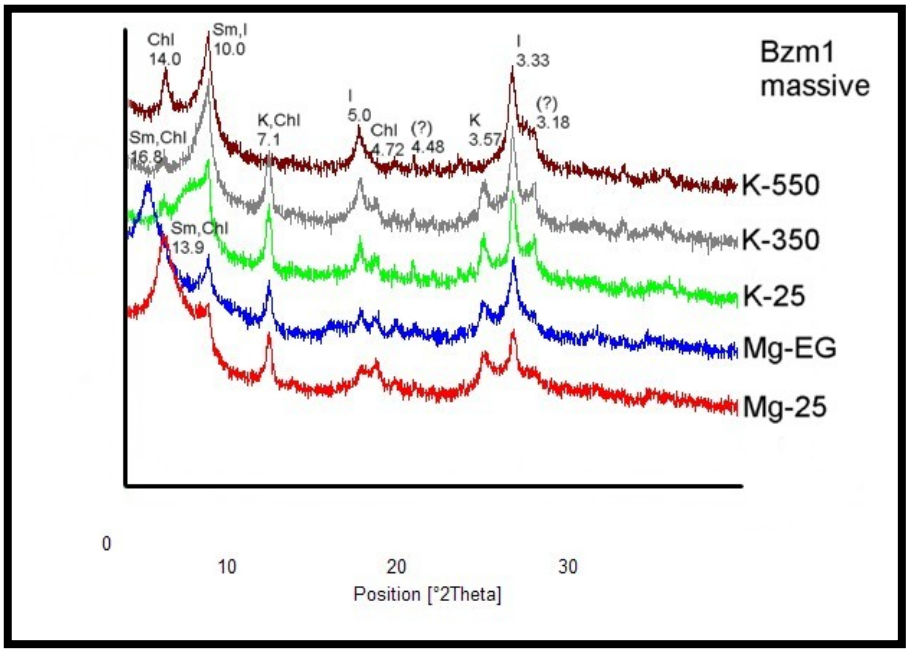

Figure 3.31. Stacked XRD diffractograms of treated samples from the Bzm horizon clay fraction; stack of peaks acquired from massive sample at 26-34 cm depth. Sm=Smectite, Chl=Chlorite, I=Illite, K=Kaolinite; numerical d-spacing values (Table 11; Appendix) also noted with suspected mineralogy. 4.48 peak is suspected to be Chl.

Bzm2 Horizon

The Bzm2 horizon was also characterized as a unit of poorly sorted coarse sand and gravel clasts (1-12 cm in length) suspended in a slightly to noneffervescent pinkish grey (7.5 YR 6/2-7/2) matrix of fine earth and illuvial soluble salts. However, this unit had a

noticeably more indurated nature (in comparison to the Bzm1) and was described as very strongly cemented (stage III+ cementation, Figure 3.32). The overall thickness of this horizon is uncertain, but it was measured to the maximum depth of exposure (minimum thickness of 280 cm, Figures 3.3 and 3.4). Average pH ranged from 7.07 to 7.26 between the depths of 75 and 305 cm (Table 2). EC ranged from 81 to 87 dS/m between 75 and 153 cm depth, and decreased to 68 dS/m at 300 to 305 cm depth (Table 2). Thirteen subsamples analyzed during textural analyses indicate that the Bzm2 is predominately a very gravelly silt loam, but four samples indicate a range of texture including very gravelly sandy loam and very gravelly loamy sand as well (Table 3). Salt content ranges from 18 to 53% by weight in these samples (Table 3). Bulk density ranges from 2.24 to 2.64 g/cm^3 between 58 and 300 cm depth (Prellwitz, 2007). Petrographic analyses confirm the extreme induration by salt minerals with a soil void content of only 1-2% (Table 4). SEM/EDS analyses indicate that the salt constituents include halite, nitratine, glauberite, and anhydrite (Table 5). XRD analyses also supports the presence of halite, nitratine, and glauberite (Table 6). Halite is the dominant saline mineral throughout the Bzm2 horizon except in one sample (174-180 cm depth) where anhydrite is more prevalent (Table 4). SEM/EDS analyses show that halite is a prolific cementing agent for this horizon, but it is also intimately associated with comparable amounts of nitratine as cement and coatings/ pendants on igneous grains as seen in samples collected at 75-80 and 153 cm depth (Figures 3.33 and 3.34). Additionally, XRD analyses suggest that nitratine is more abundant than halite near soil cracks (Table 6). However, halite is commonly seen exclusively as cement and coatings/pendants, especially deeper within the profile (e.g. ~3 m depth, Figure 3.35). Both halite and nitratine are present as

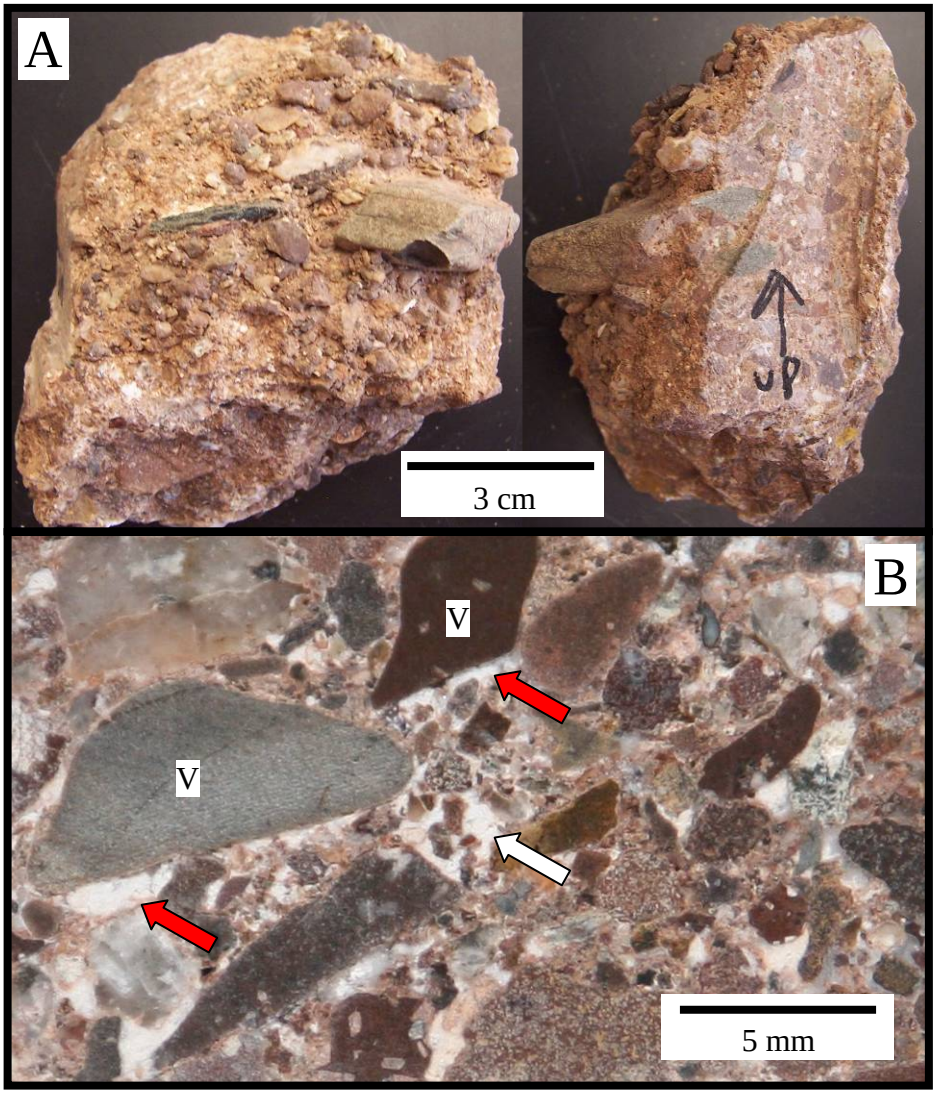

Figure 3.32. A) Photos from front and side views of a hand sample (pre-analyses) of the Bzm2 horizon collected at 155 cm depth. **B)** Photo of polished billet cut from a Bzm2 horizon sample at 155 cm depth; note salt in the form of coatings/pendants (red arrows) on underside of clasts and in interstitial spaces (white arrow).

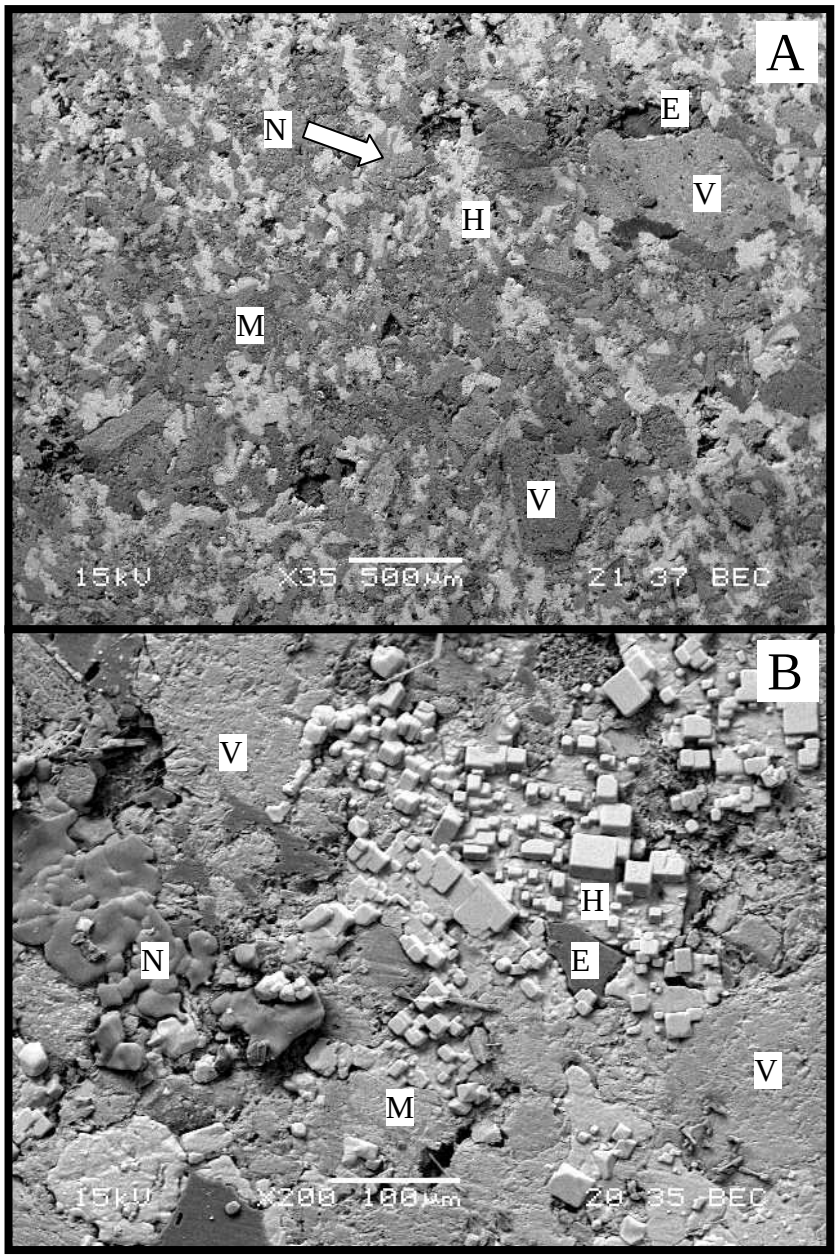

Figure 3.33. A) SEM image of Bzm2 horizon at 75 cm depth; note comparable amounts of halite (H, white) and nitratine (N, light gray; white arrow for reference); volcanic grains (V), soil matrix/micromass (M), and voids preserved with epoxy (E) noted for reference. **B)** SEM image of Bzm2 at 80 cm depth; note massive and euhedral halite and massive nitratine cementing volcanic grains and soil matrix/micromass; some voids preserved by epoxy as well.

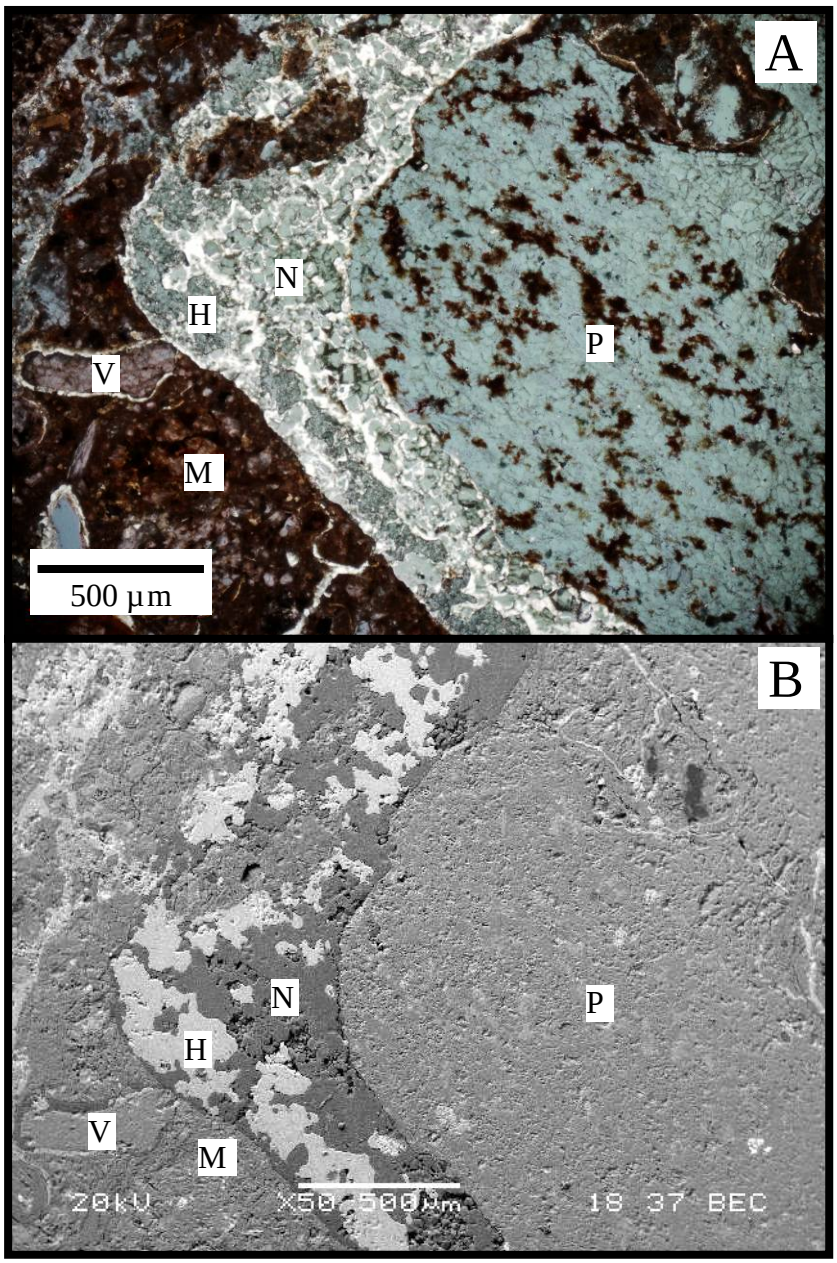

Figure 3.34. A) Petrographic photo (in PPL) of halite (H) and nitratine (N) coating a large plutonic grain (P) within soil matrix (M) (153 cm depth); see image B for halite/nitratine distinction. **B)** SEM image of salt coating depicted in figure 3.34A emphasizing the distinction and intimate association of halite (white) and nitratine (intermediate gray); also note small volcanic grain (V) coated with halite and nitratine.

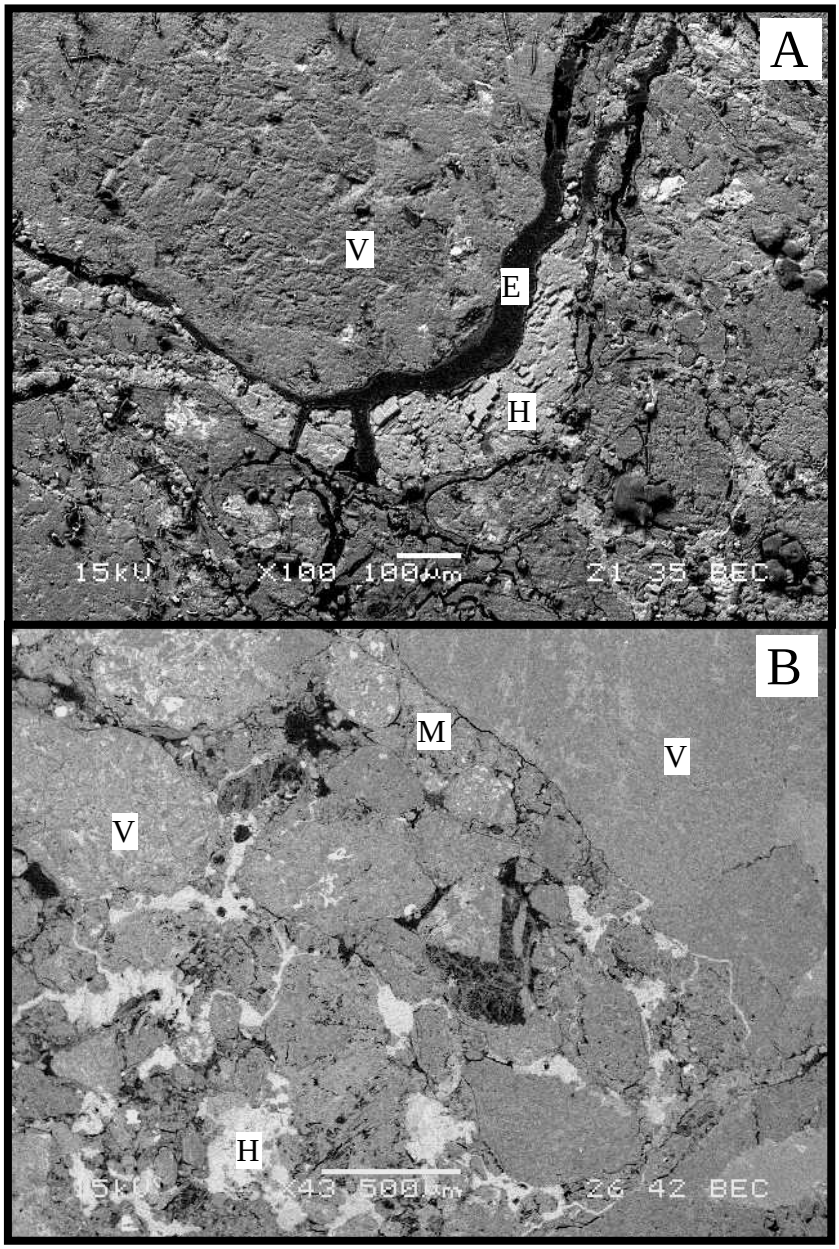

Figure 3.35. A) SEM image of halite (H) pendant on volcanic grain (V)Bzm2 at 292 cm depth; also note void preserved by epoxy (E) at grain-pendant contact. **B)** SEM image of Bzm2 at 300-305 cm depth; note that cement is exclusively halite (H); examples of volcanic grains (V) and soil matrix/micromass (M) for reference.

massive, anhedral masses (>100µm), and subhedral to euhedral crystals (≤50µm and 10-100µm respectively) (Figures 3.33, 3.34, and 3.36). Glauberite is primarily seen as an anhedral to massive cementing agent or grain coating (Figures 3.37). Anhydrite is found in interstitial space as an alabastrine (<20µm) cementing agent between 153 and 180 cm depth and sometimes seen along serrated igneous grain boundaries(along with halite) in samples collected at the 153 and 155 cm depths (Figure 3.37, 3.39, and 3.40). Anhydrite and halite are also seen cementing dislodged and broken argillans in the sample collected at 155 cm depth (Figure 3.37B & 3.39), which according to point count data (Table 4) is where the highest concentration (albeit 3%) of argillans occur within the profile. These salt minerals contribute to a soil fabric that ranges from open to close-porphyric as parent material grains/clasts are distributed (at variable distances) and ultimately matrix-supported by a fine earth fraction of silicate minerals and salt (Figures 3.32B,3.33, and 3.35B, Stoops and Jongerius, 1975; Bullock et al., 1985). Clay mineralogy elucidates illite and smectite as the main clay minerals with kaolinite and chlorite occurring in similarly minor amounts (Table 7). Smectite peaks also show an increased sharpness at approximately 3 m depth (Figure 3.41).

Soil cracks

Soil fractures are a dominant feature throughout the OE profile in horizontal and vertical orientations (Figures 3.4, 3.5, 3.7, & 3.8). Small vertical cracks (1-5 cm wide) are concentrated in the mostly unconsolidated upper three horizons. These cracks narrow and terminate at the base of the Bz horizon at a depth of 15 cm except where the upper horizons vary in thickness (≤25 cm thick). Cracks are filled with vertical laminae of salt, silt, coarse sand, and fragments of volcanic parent material contrasting the noticeably

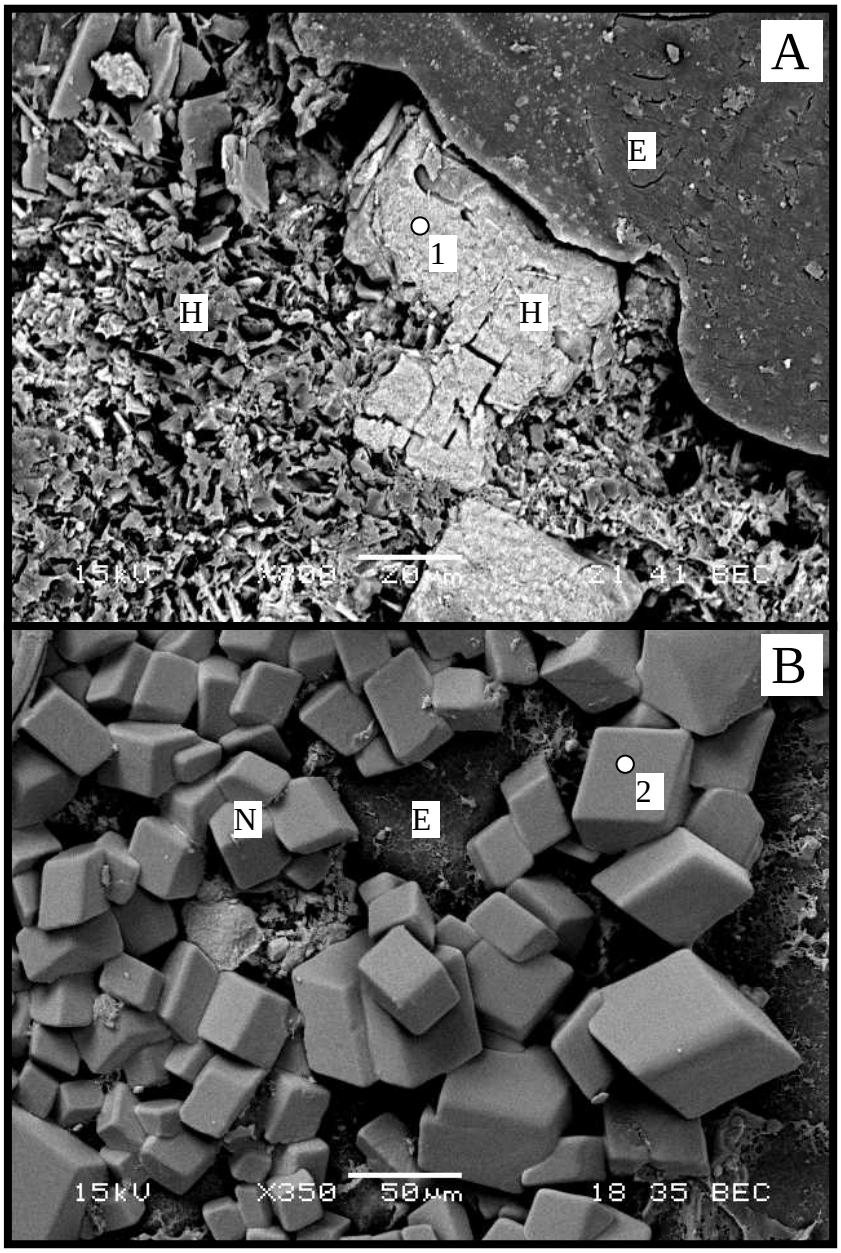

Figure 3.36. A) SEM image of anhedral and euhedral halite (H) adjacent to a soil void preserved by epoxy (E) at 75 cm depth in the Bzm2 horizon. **B)** SEM image of euhedral nitratine (N) in a soil void at 258 cm depth in the Bzm2 horizon; epoxy (E) also noted for reference. Points 1 & 2 indicate location of EDS spectrum acquisition for figure 3.38 A & B respectively.

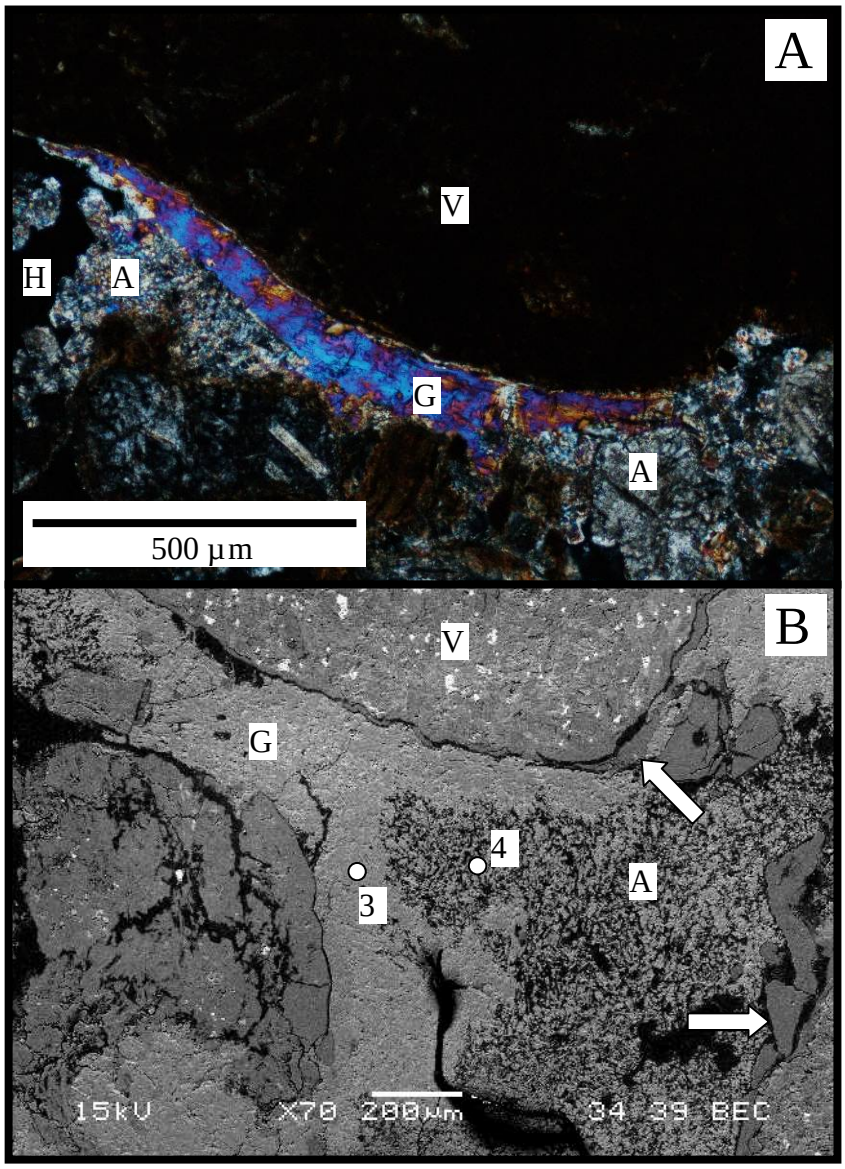

Figure 3.37. A) Petrographic photo (XPL) of anhedral to massive glauberite (G) pendant at the bottom of a volcanic clast (V) cemented by massive halite (H) and alabastrine anhydrite (A) at 155 cm depth in the Bzm2 horizon. **B)** SEM image of glauberite (G) and anhydrite (A) as cementing agents for volcanic clasts (V) at 155 cm depth in the Bzm2 horizon; also note modified/fractured argillans (white arrows) displaced from volcanic clasts and recemented by salt. Points 3 & 4 indicate location of EDS spectrum acquisition for figure 3.38 C & D respectively.

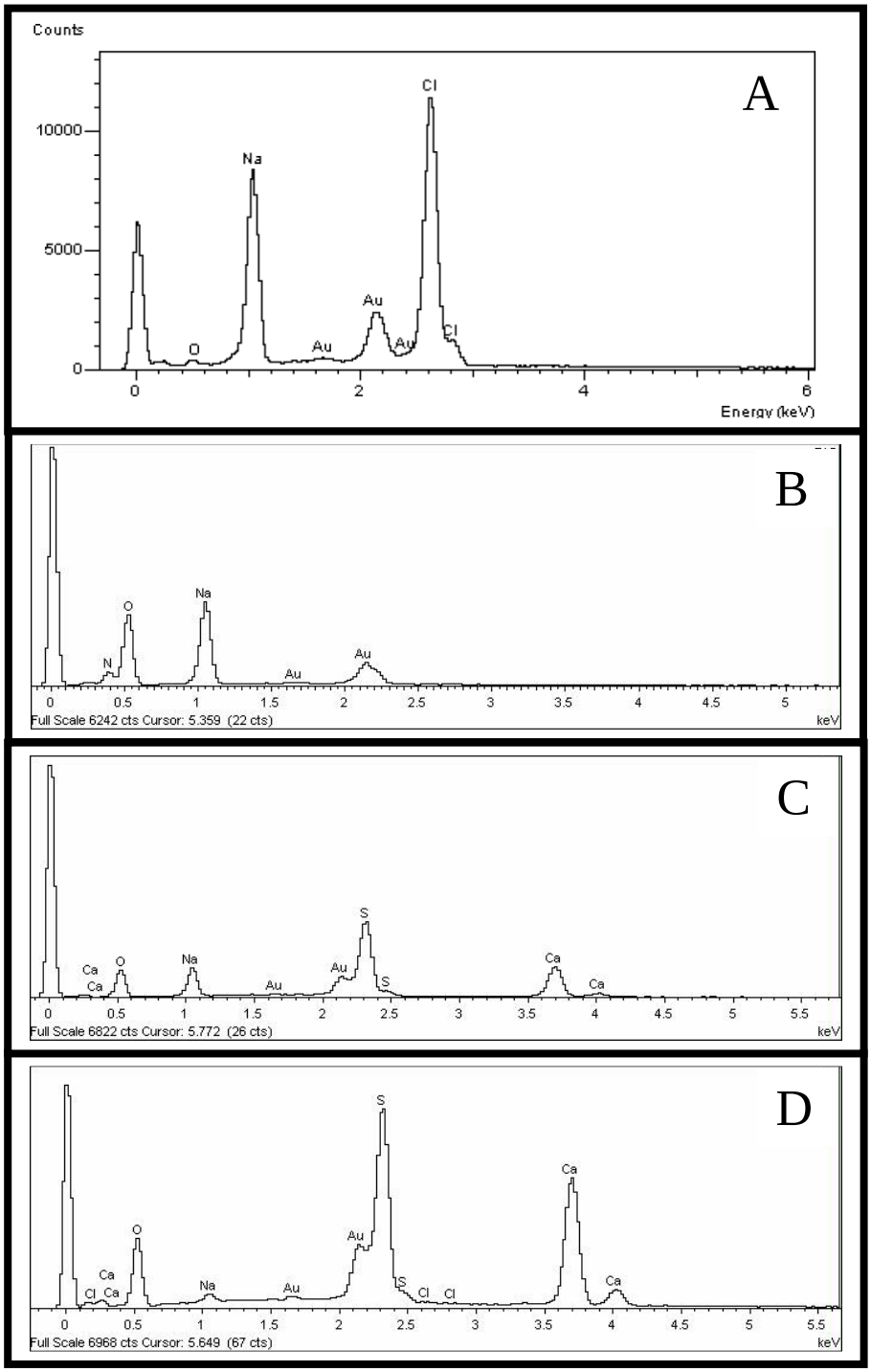

Figure 3.38. A) EDS spectrum for halite (Na-Cl peaks) from point 1 in figure 3.36A. **B)** EDS spectrum for nitratine (Na-N-O peaks) from point 2 in figure 3.36B. **C)** EDS spectrum for glauberite (Na-Ca-S-O peaks) from point 3 in figure 3.37B. **D)** EDS spectrum for anhydrite (Ca-S-O peaks) from point 4 in figure 3.37B. Gold (Au) peaks are from gold coating on samples.

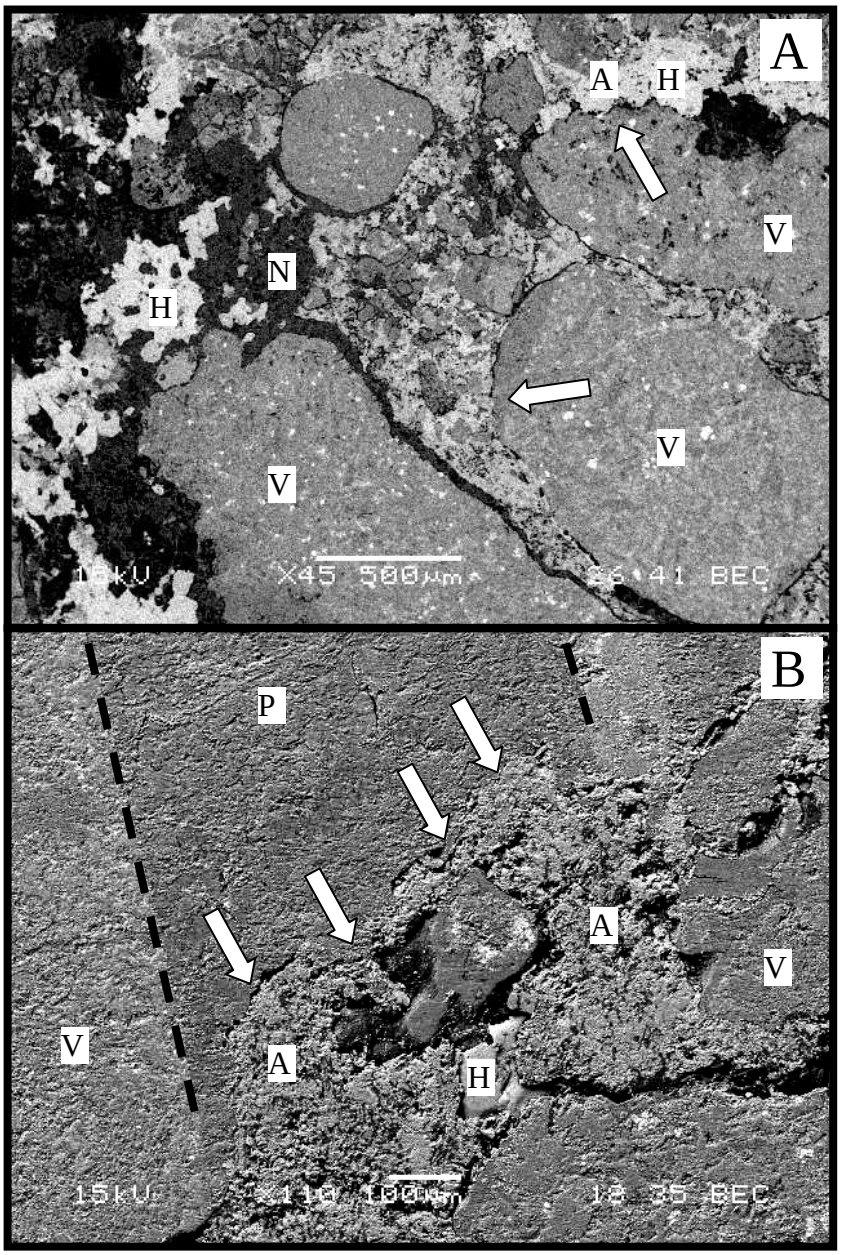

Figure 3.39. A) SEM image of volcanic clasts (V) cemented in halite (H), nitratine (N), and anhydrite (A) at 153 cm depth in the Bzm2 horizon; note serrated grain boundaries (white arrows). **B)** Close up SEM image of volcanic clast (V) at 155 cm depth in the Bzm2 horizon with serrated grain boundary (white arrows) pronounced along plagioclase (P) phenocryst adjacent to anhydrite (A) and halite (H).

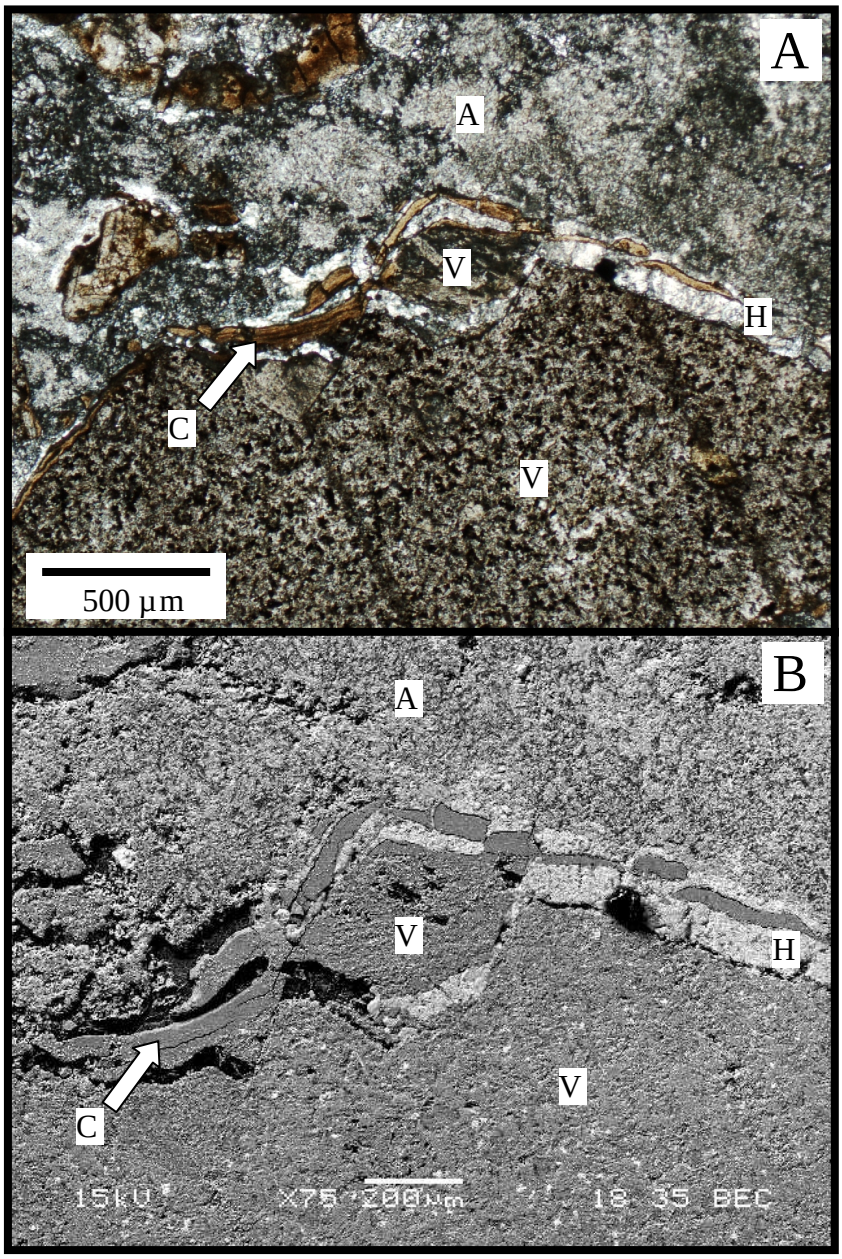

Figure 3.40. A) Petrographic photo (PPL) of an argillan (C, white arrow for emphasis) being displaced from a volcanic clast (V) cemented by alabastrine anhydrite (A) at 155 cm depth in the Bzm2 horizon; also note modified/fracture argillan recemented by halite (H). **B)** SEM image of same field of view in 3.40A with identical labels.

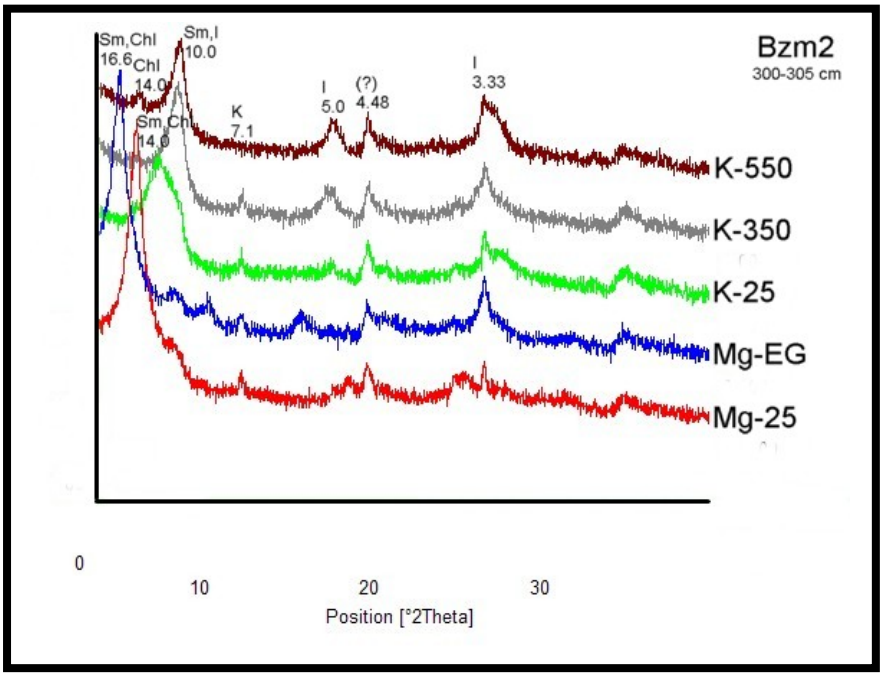

Figure 3.41. Stacked XRD diffractograms of treated samples from the Bzm2 horizon clay fraction; Peaks acquired from massive sample at 300-305 cm depth. Sm=Smectite, Chl=Chlorite, I=Illite, K=Kaolinite; numerical d-spacing values (Table 11; Appendix) also noted with suspected mineralogy. 4.48 peak is suspected to be Chl.

finer soil horizons they cut through (Figure 3.6). XRD analyses indicate that salt mineralogy varies in these laminae between 2 and 11 cm depth (within the Byz horizon); a gypsum/bassanite assemblage primarily occurs in the cracks, but transitions to include anhydrite (increasing) towards the Byz peds (Table 6). Additionally, these cracks network to form small (≤10 cm) soil polygons only seen at the surface where the Avyz horizon and desert pavement have been removed (Figure 3.42).

Both horizontal and vertical cracks (3-20 cm wide) are present in the Bzm1 horizon (Figure 3.4, 3.7, and 3.8). Horizontal / subhorizontal soil cracks (3-9 cm thick) were particularly common. Some are empty voids, but most contain horizontal laminae (2-10 mm thick) of salt, coarse sand/fine pebbles and silt in the 2 mm laminae. Average pH/EC measured 7.57 and 84 dS/m respectively in these horizontal laminae (Table 2). XRD

Figure 3.42. Field photo of small soil polygons (white arrow) observed at the surface of the Byz horizon on younger inset surface below OE profile, where the Avyz horizon and desert pavement were not present; rock hammer for scale.

analyses indicate that nitratine is the most abundant salt mineral in horizontal laminae, but halite, glauberite, and a minor amount of darapskite are also present (Table 6). Clay mineralogy suggests illite is the dominate phyllosilicate mineral in horizontal soil cracks (Table 7, Figure 3.43). Some horizontal cracks serve as a lateral offset of small (~5 cm width) vertical cracks within the Bzm1 and large (10-20 cm wide, patterned ground forming) vertical cracks that propagate through the entire profile (Figure 3.4). Most of the smaller vertical cracks typically terminate within the Bzm1, but some penetrate the underlying Bzm2 horizon narrowing to ~3 cm width. Most vertical cracks are also infilled with laminae (2-10 mm) of salt and sediment, ranging from silt to coarse sand or fine pebbles (Figure 3.8).

Similar to the Bzm1 horizon, soil fractures in the Bzm2 are abundant in horizontal (≤3 cm thick) and vertical orientations (≤20 cm wide). However, the large vertical cracks

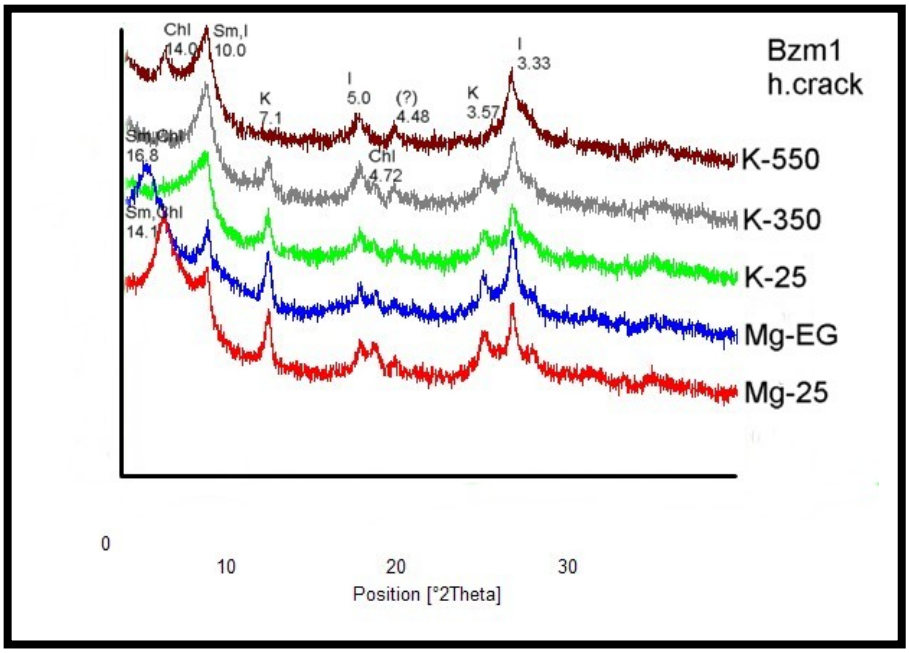

Figure 3.43. Stacked XRD diffractograms of treated samples from the Bzm1 horizon clay fraction within a horizontal crack; Peaks acquired from a horizontal laminae sample at 26-34 cm depth. Sm=Smectite, Chl=Chlorite, I=Illite, K=Kaolinite; numerical d-spacing values (Table 11; Appendix) also noted with suspected mineralogy. 4.48 peak is suspected to be Chl.

(10-20 cm wide) that penetrate all horizons and coordinate to form patterned ground at the surface are the most distinct (Figure 3.8). Most of these cracks also contained laminae (2-10 mm) of silt, coarse sand and sediment and salt in all respective orientations, but some were also observed with no infill (Figures 3.4,3.7, and 3.8). Average pH measurements in cracks within the Bzm2 horizon range from 7.15 to 7.44; the lowest value comes from a horizontal laminae sample at 75 cm depth (Table 2). Average bulk EC ranges from 80 to 88 dS/m and generally decreases with depth although the highest value comes from a vertical crack sample at 126-138 cm depth (Table 2). Textural analyses suggest that cracks are predominately very gravelly silt loams similar to most of the Bzm2 horizon, although one horizontal crack at 80 cm depth classifies as a

very gravelly loam. However, some of the highest clay fraction percentages in the OE profile are found in crack samples; the highest (18%) occurs in a vertical crack sample from a depth of 153 cm depth (Table 3). Soil fractures have higher salt percentages as well, ranging from 24 to 55% by weight (Table 3). Additionally, cracks average 43% salt whereas the massive crack-hosting soil averaged 31% by weight. SEM/EDS analyses indicate that the saline constituents include halite, nitratine, glauberite, thenardite, anhydrite, and calcium carbonate (Tables 5 & 6). Microscopic analyses reveal that these minerals are part of a composite association of parent material (volcanic/ plutonic clasts), salt minerals, and soil matrix/micromass distributed in an intricate network of soil fractures/fracture fills in vertical and horizontal orientations, some visible only with high magnification (Figure 3.44). Both macro and micro scale soil cracks reflect an indiscriminate fracture system. Cracks propagate through igneous parent material clasts, salt-cemented soil matrix, and older salt-filled cracks displaying complex cross-cutting relationships largely preserved with salt minerals (Figures 3.44B-3.47). As with the Bzm1/ Bzm2 horizons, halite and nitratine are the primary cementing agents filling these microscopic cracks, but XRD analyses suggest that nitratine is most abundant (Table 6). No trends in a single salt mineralogy with depth are present. Halite and nitratine are primarily seen as anhedral masses (>100 µm) or massive interstitial cement, fracture fills, and igneous grain coatings (Figures 3.44B-3.47), but are also present in subhedral to euhedral forms; <50µm and 15-100µm respectively (e.g. Figure 3.49). Minor anhedral (10-100 µm) and alabastrine (<20 µm) anhydrite is seen in horizontal/ vertical soil cracks and cementing fractured volcanic clasts within samples at and below 153 cm depth (Figure 3.45B and 3.48A). One discrete XRD sample collected from a vertical salt vein

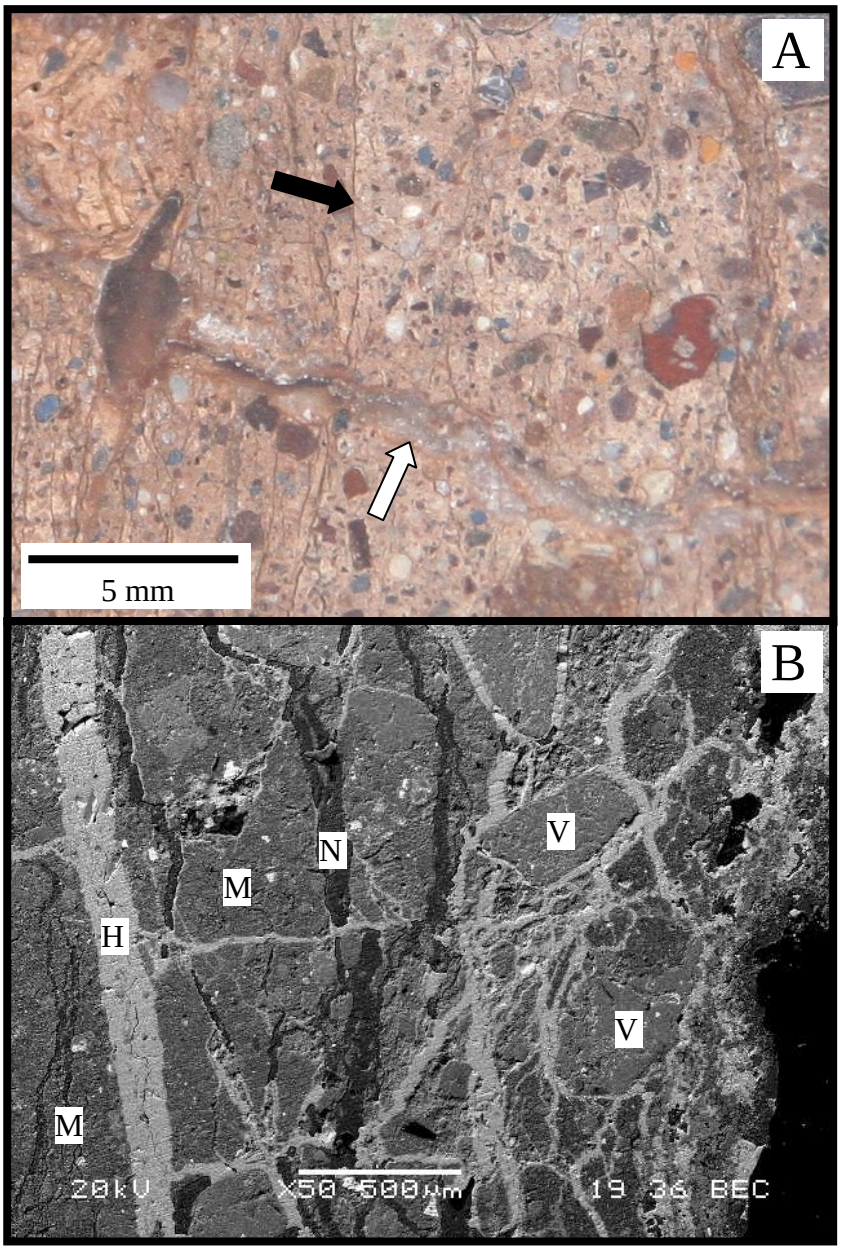

Figure 3.44. A) Photo of polished billet cut from Bzm2 horizon/vertical crack sample at 153 cm depth; note vertical laminae (black arrow) of volcanic grains and soil matrix/micromass, emphasized by slight color variations, crosscut by a subhorizontal crack (white arrow) infilled with halite/nitratine; finer cracks (mostly vertical) can also be seen throughout. B) SEM image of Bzm2 crack sample (153 cm depth) with cross-cutting fractures infilled with halite (H) and nitratine (N) that displace fractured volcanic grains (V) and soil matrix/micromass (M).

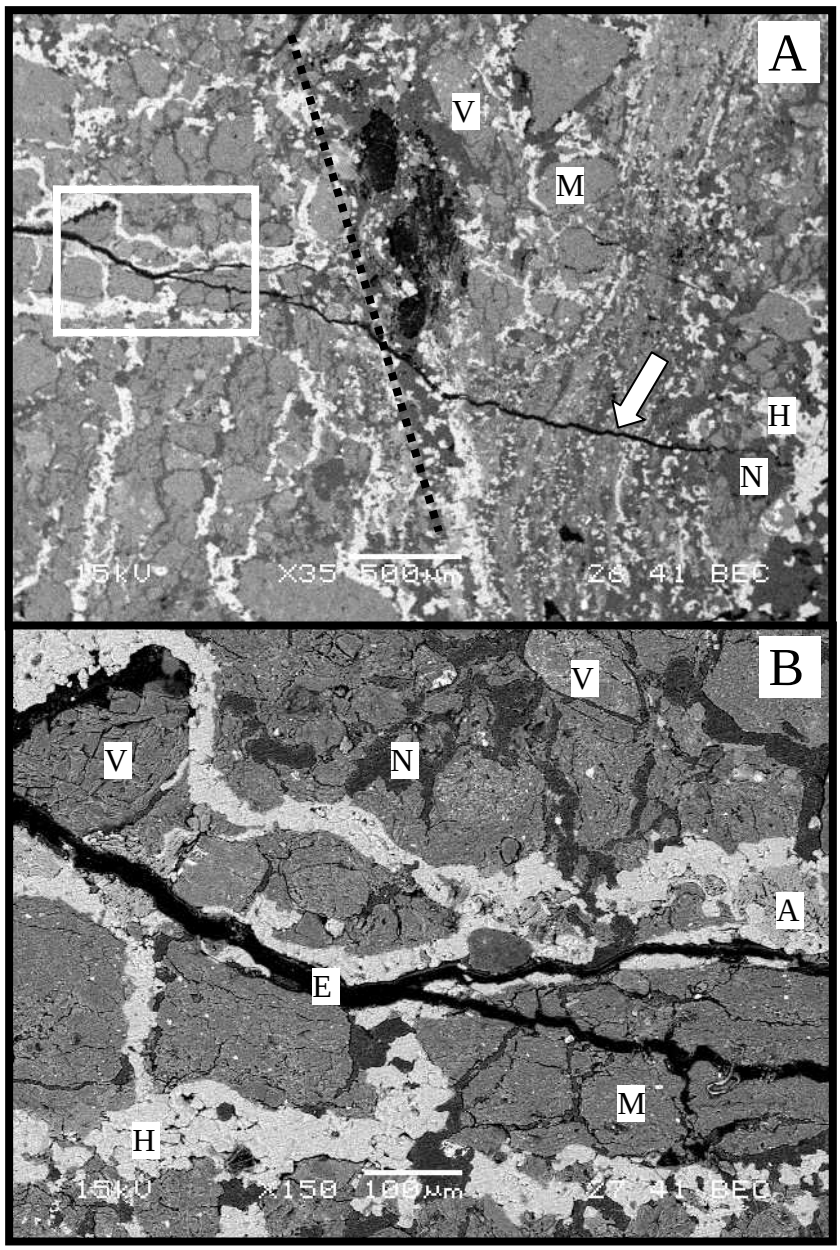

Figure 3.45. A) SEM image (153 cm depth) capturing the approximate boundary (dashed black line) between the Bzm2 horizon (left) and a vertical soil crack (right) cutting through it; note vertically oriented laminae of salt/sediment in crack, including volcanic grains (V) and fragments of soil matrix/micromass (M), along with a more recent horizontal soil crack (white arrow) cross-cutting both massive horizon and vertical crack; white box indicates field of view in figure 3.48B. **B)** SEM image showing the cross-cutting and indiscriminate nature of soil cracks; note unfilled horizontal crack preserved with epoxy (E), that cuts halite (H)/ nitratine (N) filled cracks, and nitratine-impregnated soil matrix/micromass (M); anhedral anhydrite (A) also noted.

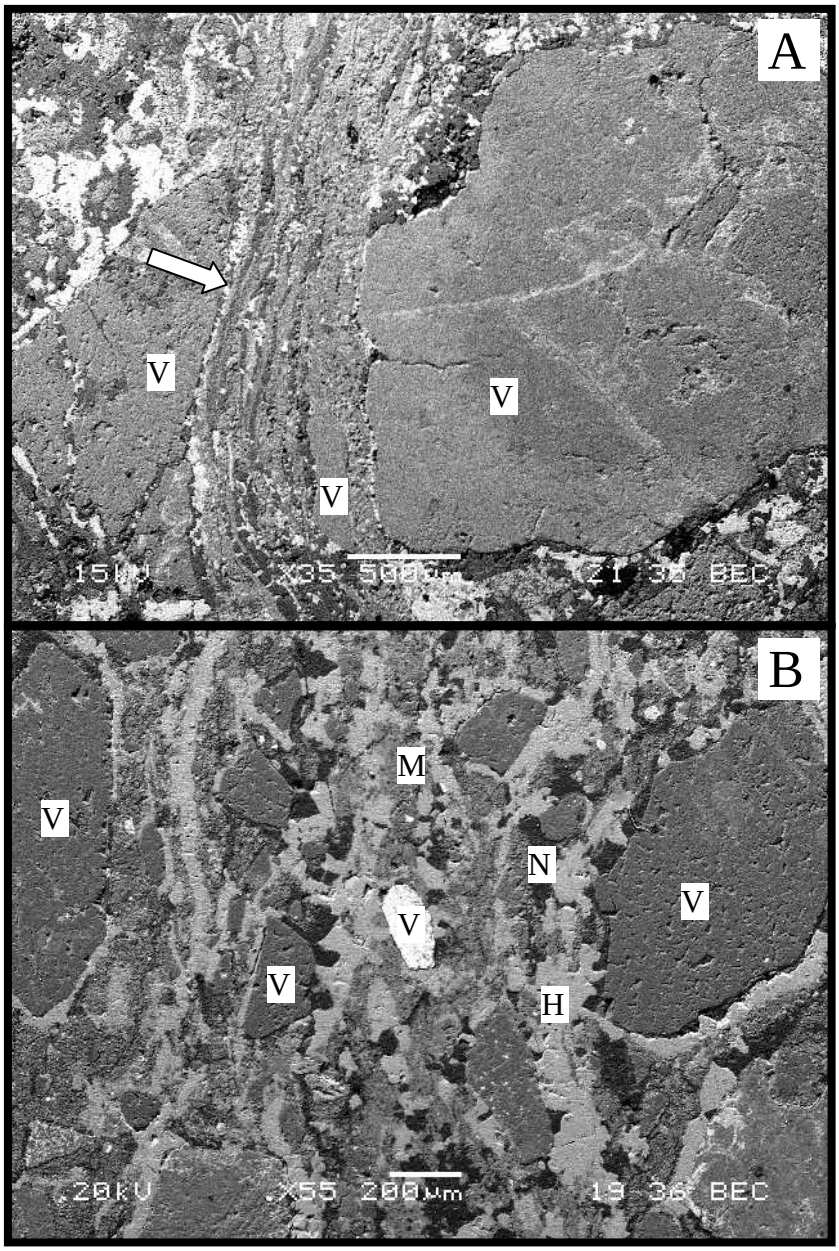

Figure 3.46. A) SEM image of volcanic clast (V) fractured by vertical crack and displaced by vertical laminae (white arrow) of salt/sediment/dust in the Bzm2 horizon at 153 cm depth. **B)** SEM image of vertical laminae of halite (H), nitratine (N), and soil micromass/dust (M) cementing/displacing shattered volcanic clasts (V) in the Bzm2 horizon at 153 cm depth.

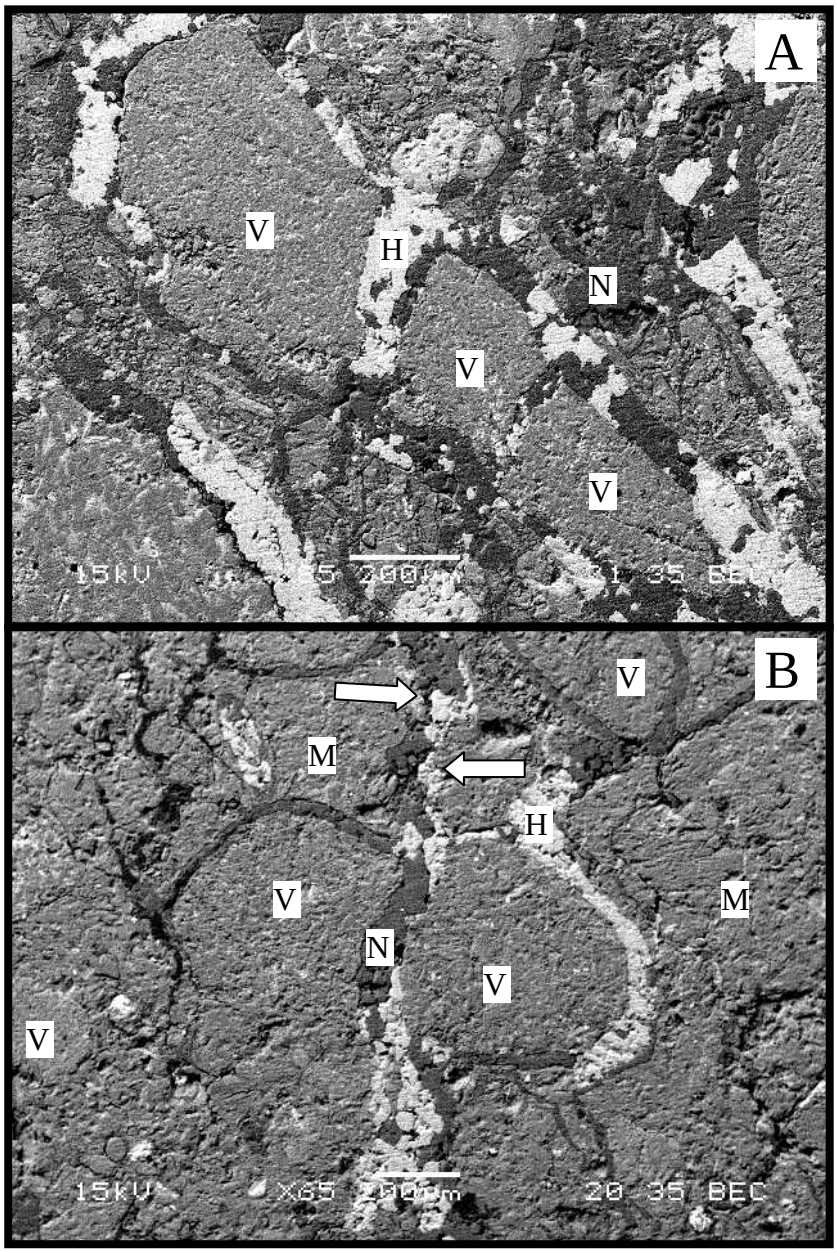

Figure 3.47. A) SEM image of a volcanic grain (V) fractured by soil cracks and displaced by halite (H) and nitratine (N) at 153 cm depth in the Bzm2 horizon. **B)** SEM image of volcanic grain (V) fractured by soil crack (white arrows) composed of halite (H) and nitratine (N); note salt-filled crack is also offset at arrows, soil matrix/micromass (M) for reference.

at 258 cm depth also elucidated mainly anhydrite (Table 6). Glauberite and thenardite are infrequently seen distributed as anhedral to subhedral crystals (5-100µm) and subhedral to euhedral crystals (>100 µm) respectively in horizontal crack samples at 75-80 cm depth (Figure 3.48B). Glauberite is also seen in vertical cracks (various depths) as anhedral or massive (>100 µm) forms as cement or grain coatings similar to those seen in the Bzm2 horizon. SEM/EDS analyses indicates calcium carbonate as irregular/anhedral masses (>100 µm) in a single sample collected within a vertical crack at a depth (258 cm) (Figure 3.49). Clay mineralogy from a horizontal crack (75 cm depth) and a vertical crack (153 cm) indicate similarly minor presence of illite, kaolinite, smectite, and chlorite (Figure 3.51). However, a vertical crack sample collected at a depth of 292 cm shows elevated peaks of illite and smectite much like the sample analyzed in the Bzm2 horizon at 300-305 cm depth (Figures 3.41 and 3.52).

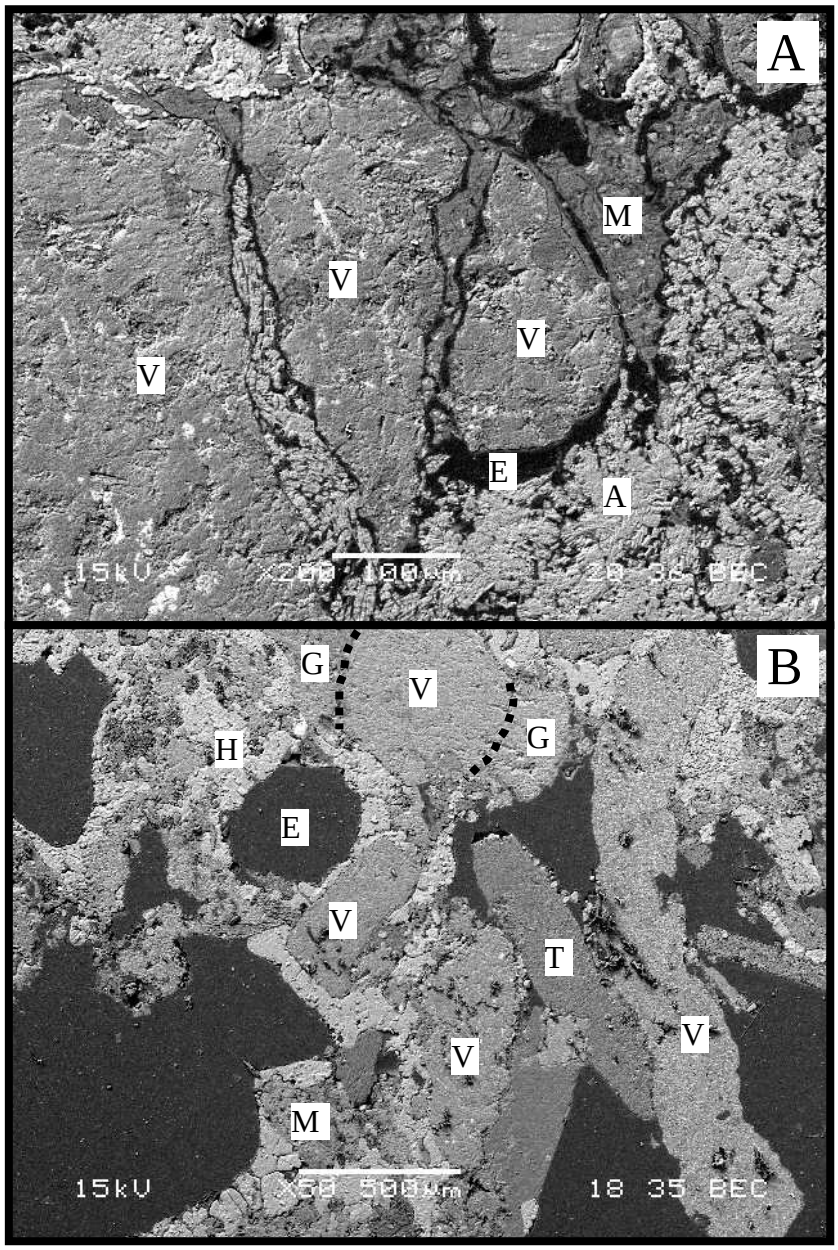

Figure 3.48. A) SEM image of a fractured volcanic clast (V) cemented in alabastrine anhydrite (A) at a depth of 292 cm within a vertical crack cutting the Bzm2 horizon; voids preserved in epoxy (E) and soil matrix/micromass (M) for reference. **B)** SEM image of anhedral/massive glauberite (G) coating a volcanic clast (V, outlined by dashed black lines) and subhedral to euhedral thenardite (T) within a horizontal crack sample at 80 cm depth cutting the Bzm2 horizon; voids preserved by epoxy (E) and soil matrix/micromass (M) for reference.

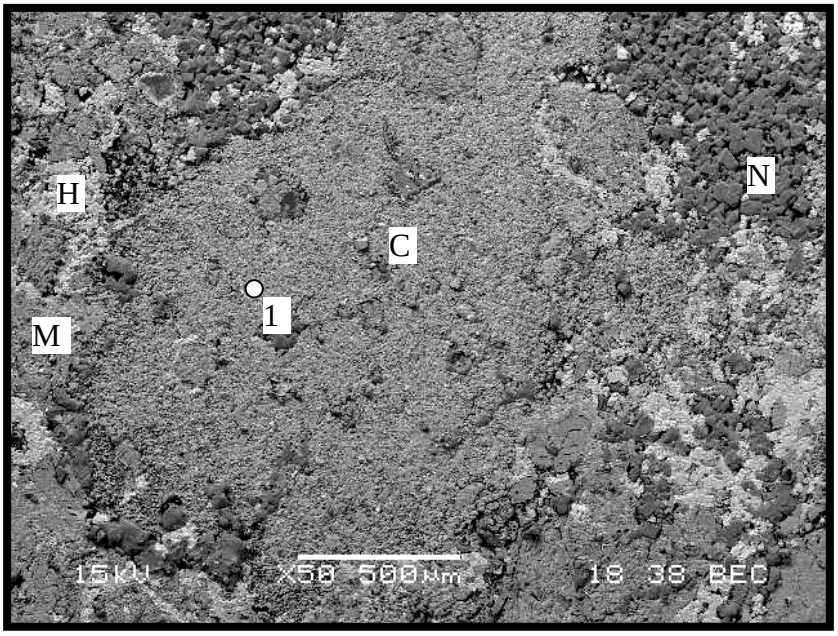

Figure 3.49. SEM image of calcium carbonate (C) accumulation seen within a vertical crack sample collected at 258 cm depth; massive to euhedral halite (H)/ nitratine (N), and soil matrix/micromass (M) noted as well. Point 1 indicates location of EDS spectrum acquisition for figure 3.50.

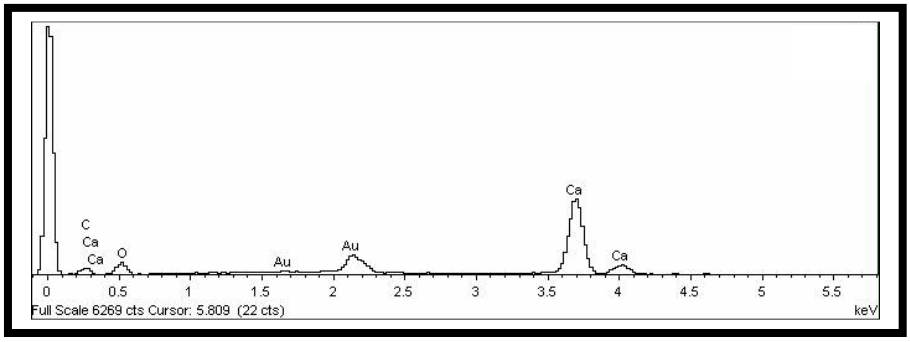

Figure 3.50. EDS spectrum for calcium carbonate (Ca-C-O peaks) from point 1 in figure 3.49. Gold (Au) peaks are from gold coating on sample.

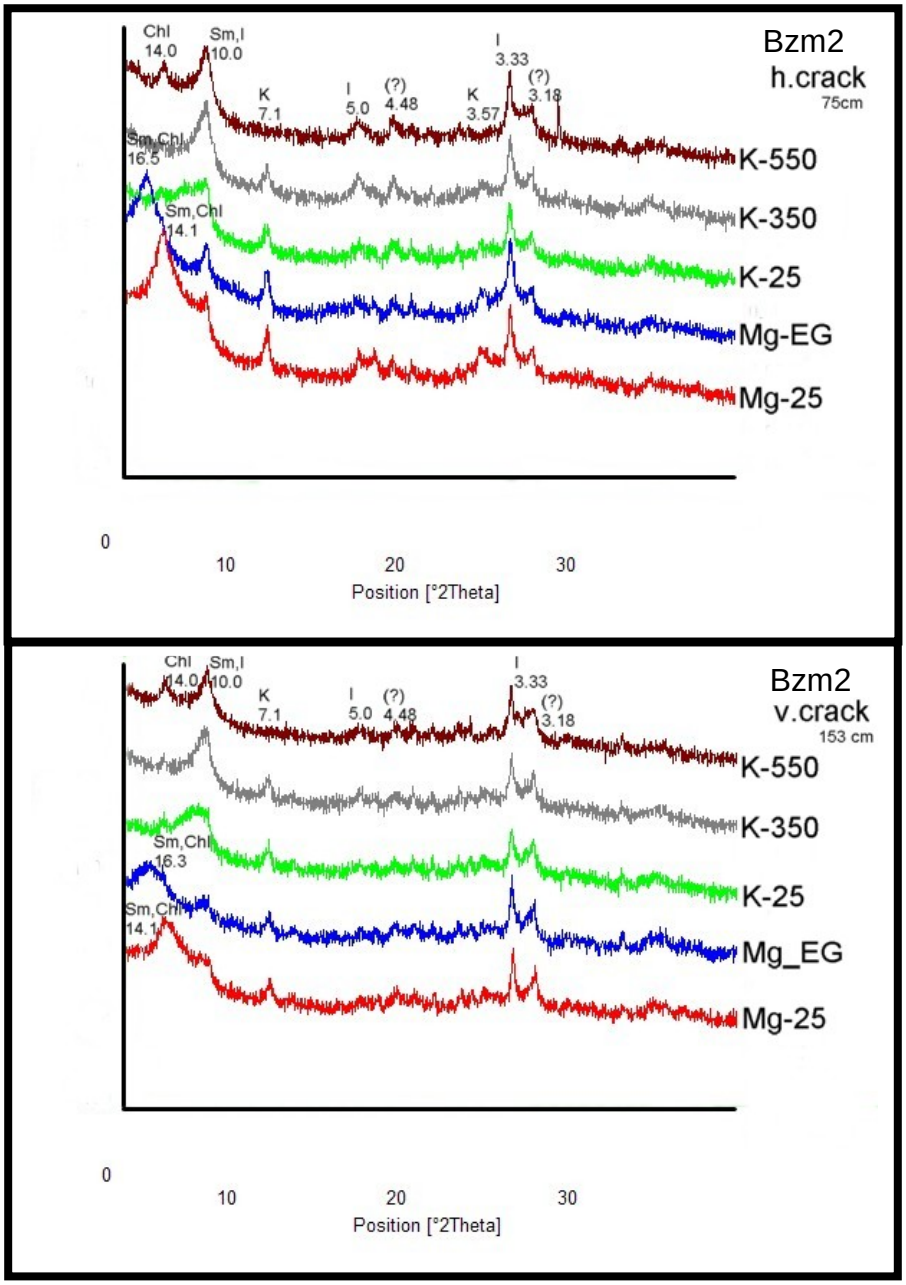

Figure 3.51. Stacked XRD diffractograms of treated samples from the Bzm2 horizon clay fraction; Upper stack of peaks acquired from horizontal crack sample at 75 cm depth; Lower stack of peaks acquired from vertical crack sample at 153 cm depth. Sm=Smectite, Chl=Chlorite, I=Illite, K=Kaolinite; numerical d-spacing values (Table 11; Appendix) also noted with suspected mineralogy. 4.48 and 3.18 are suspected to be Chlorite and Glauberite respectively.

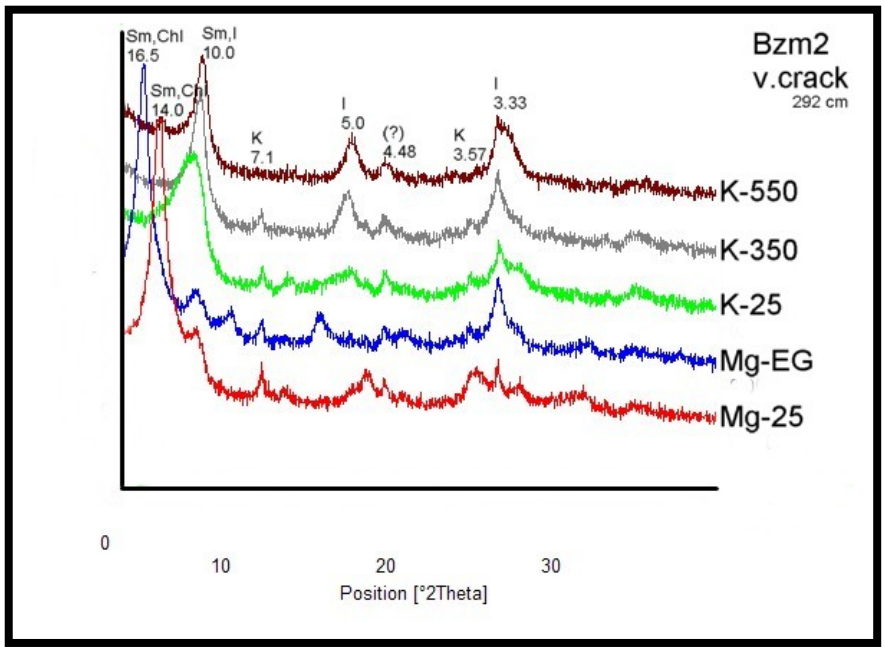

Figure 3.52. Stacked XRD diffractograms of treated samples from the Bzm2 horizon clay fraction within a vertical crack at 292 cm depth. Sm=Smectite, Chl=Chlorite, I=Illite, K=Kaolinite; numerical d-spacing values (Table 11; Appendix) also noted with suspected mineralogy.

CHAPTER IV

INTERPRETATION: HYPERARID SOIL GENESIS MODEL

Salt Heave

In arid and hyperarid climates, soils become enriched in soluble minerals. Once a soil becomes indurated with salt minerals, the behavior of these minerals dominates pedogenic processes and landscape evolution. Environmental variations in humidity/ moisture and/or temperature incite salt reactions that cause volumetric changes in soil materials, hence salt heave (Buck et al., 2006b). Salt heave can occur daily, (possibly diurnally), or with infrequent precipitation events resulting in a dominant or primary mechanism driving pedogenesis (Buck et al., 2006b; Buck et al., 2008). Salt heave is attributed to fundamental salt weathering processes: (1) dissolution/precipitation (enhanced by hydration/ dehydration) and (2) thermal expansion/ contraction of salt minerals (Buck et al., 2006b; Buck et al., 2008). Specifics of salt heave as explained by Buck et al., 2006b are outlined below:

Salt weathering processes are known to accelerate physical weathering of rock, stone, and concrete in both urban and desert environments (Winkler and Singer, 1972; Yaalon, 1970; Amit et al, 1993; Winkler, 1994). In fact, the mechanical strength of these materials is decreased in the presence of salts in solution (Dunning and Huf, 1983). Research suggests that high crystallization pressures exerted on pore walls by

precipitating salts is a major factor in the decay of rock (i.e. process (1) above; Winkler and Singer, 1972; Rodriguez-Navarro and Doehne, 1999), which is greatest in materials with smaller pores (Scherer, 1999). Hydraulic pressures generated during the transition of hydrating salts from lower to higher hydrate forms (Winkler and Wilhelm, 1970) or rapid salt precipitation where pore water is unable to drain (McMahon et al., 1992) are also reported to instigate rock degradation (i.e. process (1) above). Others have concluded that bulk volume expansion initiated by frequent temperature changes can fracture sediments cemented in salt (i.e. process (2) above; Kocurek and Hunter, 1986). Additionally, it is important to note that thermal fluctuations also influence supersaturation ratios of pore fluids, which could in turn affect the magnitude of both crystallization pressure (Winkler and Singer, 1972) and hydraulic pressure (Winkler and Wilhelm, 1970) of salt solutions. However, data presented by Rodriguez-Navarro and Doehne (1999) suggests that what is really occurring is "through-solution hydration" where temperature and humidity sensitive salts rapidly dissolved and reprecipitate creating the destructive salt crystallization pressures rather than volumetric expansion from temperature or hydration (i.e. process (1) above). Some common salts particularly responsive to this process are hydrous/ anhydrous minerals like mirabilite/ thenardite and gypsum/ anhydrite which are extremely unstable (with or without rain) resulting in dissolution/ precipitation (potentially multiple times daily) with small fluctuations in temperature/ humidity. At any rate, salt weathering is considered applicable to salt heave modification in indurated soils because extreme salt cementation promotes tensile strength analogous to rock, stone, and concrete. Since timing and intensity of each of these mechanisms are difficult to quantify in indurated soil, especially at field conditions,

and the fact that they can occur concurrently and/or interchangeably, the term salt heave used in the following discussions implies a coordination of one or more processes unless otherwise noted. However, it is important to suggest that salt dissolution/ precipitation may be the greatest contributor to salt heave in the Atacama (Buck et al., 2006b) since the anomalously high evaporation rates and solute availability will affect the supersaturation ratio, which is directly proportional to crystallization pressure (Winkler and Singer, 1972) making these forces greater within the hyperarid core of the Atacama Desert (Buck et al., 2006b).

Besides the accumulation of soluble minerals, silicate dust plays an enormous role in the genesis of soils in arid and hyperarid climates. Presented below is a new model for the genesis of soils in hyperarid climates (Figure 4.1). The two primary factors controlling the development of these soils and the resulting landscapes are eolian erosion/ deposition; and the accumulation of soluble minerals leading to salt heave.

Step 1

Incipient soils are dominated by eolian processes, which provide a sediment flux of ample salt and silicate dust. Original salt content will vary, but the coarse poorly sorted alluvium provides high porosity/ permeability and facilitates rapid infiltration of windblown soluble minerals during intermittent rain events. However, with an arid climate comes extremely variable precipitation resulting in shallow accumulation at various depths depending on the effective depth of wetting. For example, a measurable rain event in summer months may be adversely affected by higher temperatures (hence evaporation) resulting in less infiltration and salt precipitation at more shallow depths

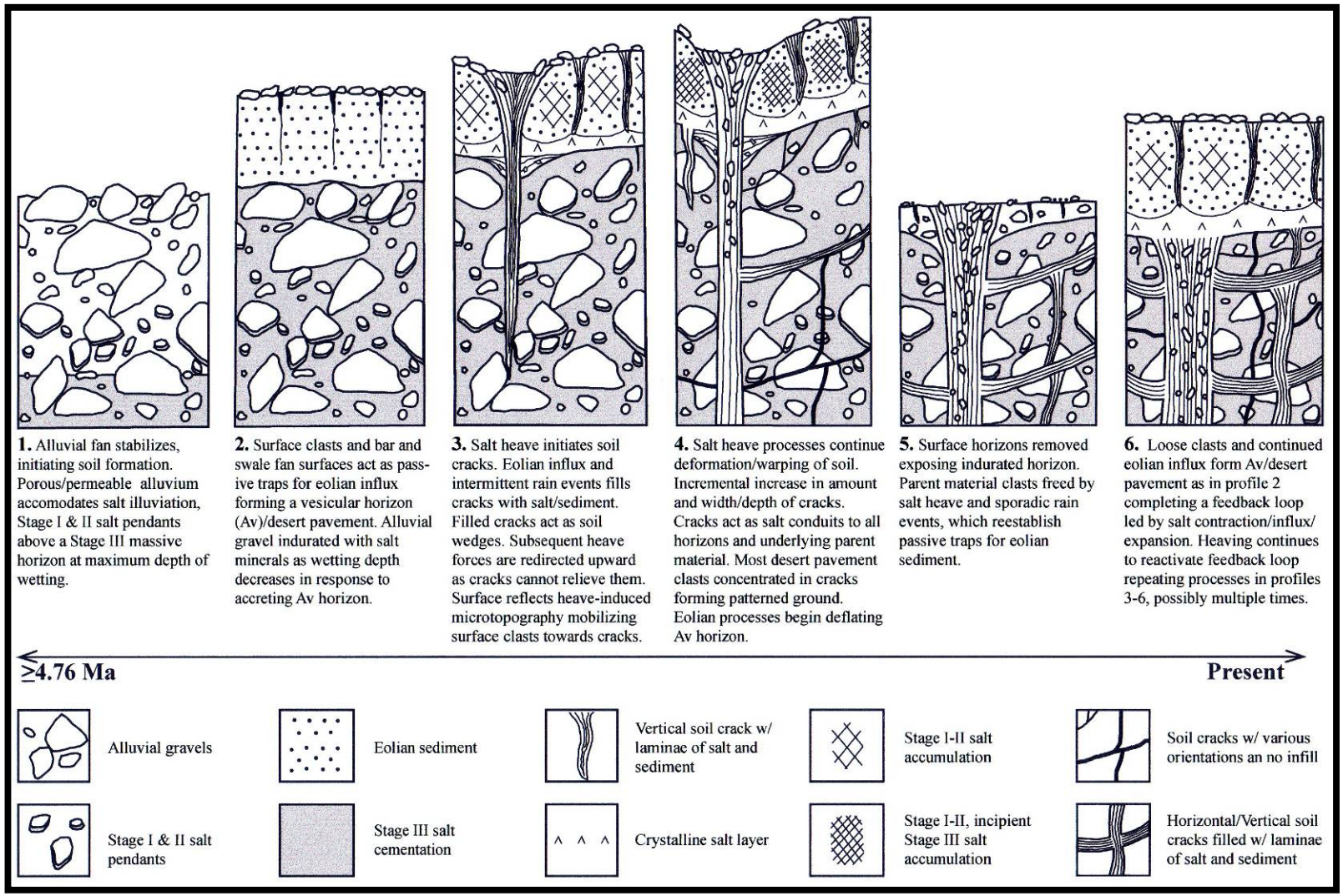

Figure 4.1. Hyperarid soil genesis model and description inspired by OE soil profile.

compared to winter months. In turn salt illuviation at relatively shallow depths promotes soil matrix displacement and clast shattering at or near the surface (Amit et al., 1993). Initial accumulation leads to Stage I snowballs (e.g. Buck and Van Hoesen, 2002) in the soil pores of fine sediment, and thin coatings on the underside of coarser clasts. Continued salt influx and sporadic precipitation encourages further accumulation within the profile as Stage II nodules and/or salt pendants on clasts. With time ($10^2 – 10^5$ years) and depending on geomorphic position/ salt dust input, overwhelming salt accumulation plugs the soil matrix creating a petrosalic or petrogypsic horizon at the maximum depth of wetting.

Step 2

Alluvial gravel at the surface, modified by thermal (McFadden et al., 2005) and salt shattering (Watson, 1985; Amit et al., 1993; McFadden et al., 1998), provide a surface litter of clasts. These clasts along with relict bar and swale topography act as passive traps for the contemporaneous influx of eolian/atmospheric salt and silicate dust. Continuous salt additions empower clast shatter, which in turn intensifies dust retention with the increased surface litter. As salt/dust is translocated with sporadic precipitation, these surface clasts are rafted with an accreting layer of airborne material below them, hence the coevolution of a vesicular horizon (Av) and desert pavement atop the alluvial gravels. This process immediately starts during Profile 1 development and is concurrent with the subsurface accumulation of salt minerals (stages I-III described in Profile 1). Continued aridity, eolian influx, and intermittent precipitation help establish a thick Av and well developed desert pavement, which effectively smooth the irregular surface

previously discerned by bars and swales. The formation of the desert pavement and Av horizon also affects the infiltration of precipitation and decreases the depth of wetting (McFadden et al., 1986). However, this silty (and potentially clay & salt-rich) horizon experiences periods of shrinking/ swelling incited by rapid wetting/drying episodes and trapped air in voids (i.e. vesicles), where intensity of expansion/ contraction varies with magnitude/frequency of water infiltration (Miller, 1971). Shrinking/ swelling of expansive clays in this horizon may also contribute to volumetric changes if present (McFadden et al., 1987). As a result these processes promote columnar (if Na^+ is present) or prismatic peds bound by fine vertical joints/cracks in the Av (McFadden et al., 1987; 1998). These cracks cause preferential water flow into the Av horizon and below. Dissolved salts are carried with the water and preferentially accumulate in the centers of the columnar peds and at the base of the Av horizon (McFadden et al., 1998). During larger rain events, water can be directed through the cracks in the Av and deliver dissolved salts into the underling horizons. Therefore, as the desert pavement and Av horizon evolve (perhaps $10^3 – 10^6$ years) this illuviated salt systematically plugs all soil pores in the underlying alluvial parent material until it is completely indurated, effectively assimilating Stage I and II zones and thickening the Stage III petrosalic horizon noted in Profile 1. Post-induration, the (massive) relatively shallow salt-impregnated alluvium responds cohesively to temperature /moisture (daily and geologic scale) fluctuations via expansion/contraction (salt heave). This initiates fine cracks / incipient soil fissures that extend shallowly into the massive horizon, which may or may not align with Av cracks.

Step 3

Continued hyperaridity and concurrent salt accumulation results in repetitive salt heave processes. Cracks between columnar peds in the Av horizon are larger after many cycles of contraction, eolian infilling, and expansion. This cyclicity and periodic precipitation have supplied noticeable salt via multidirectional illuviation or wicking into the inner reaches of the Av, inflating the unconsolidated horizon(s) with Stage I-II salt morphologies and subsequently enhancing expansion/contraction (i.e. salt heave supplements shrink-swell) within this horizon. Since Av cracks terminate at the indurated horizon contact, a pure layer of salt has also accumulated at the base of the Av representing the periodic, possibly seasonal, flushing of soluble salt(s) being translocated through this horizon. Continued expansion-contraction/salt heave in the indurated soil has resulted in an overall upward heave towards the surface. This has expanded the original surface ruptures in the unconsolidated horizon(s) (including the desert pavement). Some cracks align with incipient soil fissures in the petrosalic horizon described in profile 2 forming larger cracks. Similar to the cracks in the Av horizon, these larger composite cracks also experience multiple cycles of contraction, infilling, and expansion. However, contrary to the smaller cracks, the opposing forces caused by the infilled salt/sediment during subsequent expansion exceed the tensile strength of the indurated horizon. Therefore cracks propagate deeper into the profile instigating future infill and incremental crack extension. Vertical laminae of salt/sediment indicate the cyclicity of eolian dust infill of open cracks followed by salt heave expansion and compaction of the crack-fill sediment. With time these infilled cracks not only penetrate deeper, but become increasingly wider and more sizeable partitions to the adjacent large

volumes (polygons) of soil, largely indurated and continually heaving (daily and geologic scale). As a result these growing cracks (also salt-rich) heave contemporaneously and coordinate with the heaving soil polygons to intensify the volumetric changes within the soil profile. During expansion, all of the opposing forces generated between soil polygons cannot be relieved by the cracks since they have been filled by salt/sediment. Therefore, unrelieved forces are redirected towards the surface, reinforcing the upward warping of surface horizons. These adjustments solely account for small volumetric changes. However, over 10^5 - 10^6 years the countless incremental modifications are responsible for microtopographic highs (soil polygons) / lows (cracks) at the surface that instigate gravitational migration of surface clasts (mm by mm) towards large cracks, which contribute to incipient patterned ground formation.

Step 4

Vertical crack contraction/ infill/expansion cycles have incrementally increased the amount, width, and depth of soil cracks in the massive horizon (including horizontal and sub-vertical cracks). These new and/or larger vertical cracks transmit meteoric water and eolian salt/sediment beyond the petrosalic horizon and systematically enrich the underlying alluvium until eventual induration. This not only increases the thickness of the soil solum (in meters), but also incorporates a larger volume of cemented / indurated soil that enhances each incremental salt heave-induced modification of the profile. Salt heaving results in a noticeably undulating surface topography where the centers of soil polygons serve as surface highs and large soil cracks serve as surface lows. Surface relief leads to several developmental elements that ensure profile evolution. First, it

encourages salt / sediment translocation, both from wet and dry processes, as it directs these constituents into soil cracks that can reach deep into the soil profile and further enhance salt heave. Additionally, each incremental heaving action that results in an increase of relief also aids in mobilizing desert pavement clasts, either by gravitational or surface creep processes, towards soil cracks. Subsequently, clasts (and any dust addition) also act as rigid supports within the soil crack infrastructure, which ultimately makes the infilled crack more resilient during expansion of soil polygons. This reinforces upward heave and subsequent salt / mineral / clast migration toward cracks, repetitively facilitating salt heave processes and enhancing the effects noted above. Repetitive and systematic heaving also initiates cycles of brecciation / recementation of parent material clasts and salt impregnated fines within the massive horizon. Parent material clasts are physically weathered through heaving, but also undergo dissolution through pressure solution caused by extreme crystallization pressures via mineral precipitation in confined soil space/cracks (e.g. Winkler and Singer, 1972; Monger and Daugherty, 1991; Robin, 1978). At the surface, clasts have been shifted into the polygonal cracks and away from the center of the polygons, forming strongly developed patterned ground. Thus, clasts no longer form a strong desert pavement leaving the unconsolidated surface horizons (Av and underlying loose salt horizons) subaerially exposed. Because the centers of the large soil polygons are now no longer covered by a desert pavement, eolian deflation begins to erode surface horizons. These materials then become source material to fill adjacent cracks and soils downwind.

Step 5

The continuously dynamic indurated horizon simultaneously heaves as eolian processes erode the Av horizon. Eventually, the Av and other unconsolidated surface horizons are completely removed. Additionally, the subaerial exposure readily subjects the exhumed indurated massive horizon to temperature/ humidity variations and sporadic rain. This leads to the dissolution of soluble salts near the surface freeing parent material clasts as well as the fine earth material formerly cemented in the indurated horizon. Salt heave concurrently cracks and brecciates the surface increasing soil cracks/conduits, and the amount of some loose (fine) material directly. Subsequently, the fine materials freed via salt dissolution and salt heave are entrained and removed by eolian deflation, leaving only coarse parent material clasts as surface litter. Sporadic precipitation events also help flush any sediment/dust and salts not removed by eolian processes into new and relict surface cracks/pores in the saline alluvium. Additionally, some of the more sensitive salts (i.e. hydrating salts) will dissolve/ recprecipitate quickly as smaller, less-cohesive, and "fluffy" crystals readily entrained via eolian processes and redistributed in nearby passive traps or soils downwind (Buck et al., 2008). Soluble minerals (and/or silicate fines) that are flushed back into the soil profile via soil cracks fuel the well instituted salt heave processes. Parent material clasts liberated from the indurated soil reform a desert pavement and along with irregular surface morphology reestablish passive traps that begin to retain eolian sediment /atmospheric dust resembling step 2.

Step 6

Similar to profile 2, once a desert pavement is re-established, fine eolian material will accumulate beneath and establish another generation of Av/desert pavement formation.

This represents the completion of a feedback loop initiated and driven by salt contraction / influx / and expansion. However, this terminus does not conclude or prevent further pedogenesis. In contrast to the Av / desert pavement formed in profile 2, this unconsolidated unit has formed upon a well established salt heaving "engine" with pedogenic momentum. Persistent salt heave reactivates the feedback loop and repeats processes described in profiles 3-6, possibly multiple times, probably only halted or diverted by a shift in climate shift resulting in salt dissolution and/or another large earth surface process causing massive erosion or burial of the soil.

CHAPTER V

DISCUSSION

Salt Heave

The nitrate-rich soils found in the Atacama Desert are characterized by networks of vertical cracks filled with vertically stratified lenses of gravel, sand, silt, and copious amounts of various salt minerals. At OE these vertical cracks extend deep (≥3 m depth) into soil profiles and coordinate to define large (~2m diameter) soil polygons. Polygons are highlighted as microtopographic lows, created by vertical cracks, sort surface clasts forming a surface anomaly refered to as patterned ground (Buck et al., 2006b; Figure 3.2). Currently, patterned ground and the vertically stratified crack morphology have only been reported to form via frost heave processes (e.g. Lachenbruch, 1962; Retallack, 2001). Similarly, clay-rich soils (i.e. Vertisols) also reflect loosely comparable features known as gilgai and chimneys, respectively, as a result of shrink-swell properties sometimes referred to as argilliturbation (Brady and Weil, 2004; Beckman et al., 1984; Newman, 1983; Shaetzl and Anderson, 2005).

However, neither frost heave nor argilliturbation can explain the occurrence of these features in the hyperarid core (Central Depression) of the Atacama Desert where the OE site resides (Figures 1.3, 1.4, and 1.9). The present and geologically persistent hyperarid climate (see Climate, pg. 12) consists of temperatures and extremely low precipitation inputs that are not conducive to the formation of ice or frost heave

processes. Additionally, clay content measured in this study indicates that clay minerals (including shrink-swell clays) are in low abundance (averaging 8%, Table 3; percentage calculated after salt removal). Even if shrink-swell clays are present in the silt fraction it is unlikely their contribution is comparible to clay mineral dynamics present inVertisols (>30%, Brady and Weil, 2004) since silt percentages were calculated after salt removal as well, suggesting little to no soil modification via argilliturbation. Therefore, the lack of ice/ expansive clays and the prevalence of salt minerals (Tables 1,3,5, and 6) a new formation process termed salt heave (Buck et al. 2006b) is utilized to explain the expansion/ contraction forces responsible for soil cracks, patterned ground formation, and hyperarid pedogenesis at OE.

Hyperarid Pedogenesis at OE

The Central Depression of the Atacama Desert is known to contain extensive alluvial fan deposits termed “Atacama gravels” (Nishiizumi et al., 2005) deposited between the Oligocene and mid-Miocene in response to Coastal Range and Andean uplift (Mortimer and Saric, 1975; Ericksen, 1981; Clarke, 2006). These ancient landforms have been remarkably stable and preserved due to low erosion rates (Nishiizumi et al., 2005) and limited chemical weathering losses (Ewing et al., 2006) attributed to the present and geologically persistent hyperarid climate since the mid-Miocene (Ericksen, 1981; Alpers and Brimhall, 1988; Rech et al., 2006). Since the OE soil profile examined in this study is located medially on an ancient alluvial fan composed of poorly sorted, gravelly, (mainly) volcanic material, this landform is considered to be correlative to the Atacama gravels ubiquitous throughout this hyperarid corridor of the Central Depression.

Therefore, soil development at OE theoretically could have begun as early as the mid-Miocene (~13-15 Ma). However, soil inception would have been dependant on site specific soil stability (possibly affected by erosion and/or sedimentation), which is known to be variable in arid climates and/or fluctuations in intensity of aridity (e.g. Buck and Monger, 1999). Aridity has certainly varied in magnitude in the Atacama since the Miocene (e.g. onset of hyperaridity) adding an element of uncertainty to the initiation of profile development and complicating the estimation of OE profile age. However, Prellwitz (2007) dated granitic surface boulders on a nearby lower, younger, inset geomorphic surface (OE2) using cosmogenic radionuclide (CRN, ^{10}Be) dating. These analyses yielded empirical dates of 2.71-3.23 Ma for the OE2 surface. Using the nitrate inventory (368.28 kg) contained in the soil at OE2, Prellwitz (2007) also calculated a nitrate flux rate (0.041 g/m^2/yr) based on those dates. In the absence of granitic surface boulders on the OE surface (of focus in this study), the OE2 flux rate was substituted to calculate an empirical age with the nitrate inventory (613.31 kg) at OE. This calculation suggests a minimum empirical age of 4.76 Ma for the OE soil profile (Prellwitz, 2007). Although, the sizeable difference in nitrate inventories, the fact that OE2 is an inset fan within the OE fan surface, and lower bulk density (2.29 vs. 2.38 g/cm^3) as well as average salt content (28 vs. 40%) (Prellwitz, 2007) between OE2 and OE respectively suggests that the OE profile may be much older than the difference in empirical dates between OE2 and OE imply. Therefore it is believed that the reported age of 4.76 Ma is not only a minimum age because of decreased nitrate retention with increased cementation over time (Prellwitz, 2007), but inherently low due to the lack of datable surface material (granitic boulders) corresponding to the actual landform/surface age and

inception of pedogenic processes at OE. The age of this profile is consequently broadly constrained between 4.76 Ma (Prellwitz, 2007) and ~13-15 Ma (Ericksen, 1981; Nishiizumi et al., 2005; Rech et al., 2006) and simply inferred as ≥4.76 Ma in the proposed hyperarid pedogenesis model (Figure 4.1).

Step 1

Step 1 (Figure 4.1), therefore, models this Atacama gravel-type alluvial deposit at OE stabilized sometime between 4.76 Ma and ~13-15Ma. After stabilization, the irregular OE surface began to passively trap eolian dust/salt between surface clasts and within surface lows associated with bar and swale topography (McFadden et al., 1987; McFadden et al., 1998). Additionally, the coarse Atacama gravels provided ample porosity/ permeability for infiltrating meteoric water. Albeit extremely variable in frequency and magnitude given the arid/hyperarid climate, measureable precipitation events flushed eolian derived dust/ salts, and/or atmospheric solutes already dissolved in the rain water before intercepting the OE surface, to the effective depth of wetting. The very coarse parent material (i.e. Bzm1 and Bzm2 horizons) at OE (Table 3) is evidence for the assumed rapid and readily accommodated dust/salt-enrich water percolation. However, cutans found in micromorpological analyses provide the strongest evidence for mineral illuviation early in soil formation at OE. Two types of cutans are seen using micromorphologic techniques, halans (salt pendants) and argillans. These features could have only formed as illuviated dust/salt accumulated on the surfaces/ undersides of clasts when void space was still abundant in the incipient soil profile (i.e. before complete induration of the alluvium). Salt pendants are prolific in the Bzm2 horizon and primarily composed of halite, and halite-nitratine, but occasionally glauberite (Figure 3.34, 3.35A,

3.37A). Stage II pendant formation is comparable to a stalactite-style accumulation as salt-rich pore fluids periodically precipitate salt minerals on the undersides of clasts since this is the last place for these fluids to concentrate (in coarse parent material) as gravity and climate dictate the depth of wetting and salt precipitation; each periodic accumulation adds another layer of salt to the pendant, hence the stalactite comparison (Amundson et al., 1989, 1994; Birkeland, 1999; Chadwick et al., 1988; Courtey et al., 1994; Ludwig and Paces, 2002; McFadden et al., 1991; Pierce, 1985; Pierce and Scott, 1982; Reheis et al., 1992; Sowers et al., 1988; Treadwell-Steitz and McFadden, 2000; Wang and Anderson, 1998). However, voids are sometimes present adjacent to pendants in the OE profile at the clast-pendant boundary (Figure 3.35A) suggesting that salt accumulating directly along the clast edge is not necessarily the first increment of salt accumulation on an individual clast. This observation was also reported by Brock and Buck (2005) in calcium carbonate pendants and indicates that pendants do not always form in a manner similar to stalactites. Pendants at OE, in contrast to calcium carbonate pendants, are composed of highly soluble salt minerals and are more likely to dissolve/ re-precipitate with changes in temperature, humidity, or pore space chemistry. Thus, distinct laminae are unlikely to be preserved, which may explain why none were observed in this study. Because of this, it is difficult to interpret the relative timing or sequence of salt mineral formation in these pendants. It is also important to note that extreme caution was taken prior to and during sample preparation for these analyses to avoid the destruction of (micro) pedofeatures such as pendant laminae. Samples were never exposed to water, high humidities, or sizeable temperature fluctuations; however some dissolution/ re-precipitation may have occurred prior to analyses due to the highly sensitive/ soluble

minerals present at OE (Table 1). We believe this is unlikely because "dusting" of tiny euhedral crystals was not seen covering the surface of thin sections during sample preparation. "Dusting" is observed when soluble salt samples are exposed to high humidity/ water effectively altering salt mineralogy/ morphology (Dr. B.J. Buck, personal communication). Additionally, the high relief or the 3-D effect reflected in some of the SEM images is attributed to minimal epoxy removal around various salt crystals during thin section preparation as opposed to salt (re)precipitation because of sample alteration. Epoxy from thin sections (both in-house and externally prepared) was noted to become "gummy" then spall in the presence of acetone, which was used during sonification to remove polishing media from in-house prepared thin sections, as well as surface preparation for sample photos (externally epoxied billets). Degraded epoxy removed during sample preparation creates microtopography that is subsequently enhanced by high magnification resulting in the high relief seen in SEM images. Therefore the microscopic results presented herein are considered to be an accurate reflection of salt mineralogy/ micromorphology within the OE soil profile even after samples were collected and transported out of the hyperarid Atacama Desert environment.

Argillans formed in the the incipient soil profile (Step 1) are primarily found in a sample collected at 155 cm depth (Figures 3.37B and 3.40), though noted between depths of 153 and 258 cm (Table 4). These depths indicate that they must precede the induration of the Bzm2 since the Na-salts (i.e. halite) presently cementing most of the Bzm2, would have had a dispersive influence on clays (Petersen, 1980). This would have caused soil matrix inundation with salt and dispersed clay minerals rather than discrete clay coats. However, petrographic (Table 4) and SEM (Table 5, Figures 3.37B and 3.40) show that

the depths where argillans are present contain noteable amounts of Ca-sulfate (anhydrite) and Na-Ca-sulfate (glauberite). As the soil solutions transmitting these salts to depth came in contact with the clay dispersed in Na-salt (or vice versa), dispersed clays would have flocculated in the presence of the illuviated Ca^{2+} ions, likely resulting in argillans on volcanic grains represented herein. Additionally, Petersen (1980) suggests that Na-salt accelerated argillic soil formation (10^3 years) in saline fan alluvium in the Panamint Valley, California by enhancing the infliltration of dust derived clays. This helps to explain the presence of clay (Table 7), especially at depth, given the limited amount of chemical weathering of volcanic materials permitted by the hyperarid climate at OE even in the initial periods of soil genesis.

With time these same infiltrating saline soil-fluids plugs a zone within the alluvium at the maximum depth of wetting, creating a diagnostic petrosalic horizon (Amit et al, 1993); also modeled in the base of profile 1 (Figure 4.1). Induration of the OE profile to all observable depths prevented the determination of the maximum wetting depth of the profile at this point and presently. The exact timing for the formation of this indurated horizon is speculative, but considering the vast (geologic) evaporite deposits, salars, and other saline-soils (Ericksen, 1981; Rech et al., 2003; Clarke, 2006) upwind of OE in the Pampa del Tamarugal (Figure 1.4), eolian processes likely accelerated induration in perhaps as little as 10^2 years. However, Amit et al. (1993) suggests that petrosalic horizons in the hyperarid ($\leq$50 mm/yr precipitation, Amit et al., 2006) Negev Desert, Israel are formed in gravelly alluvial fan chronosequences in roughly 500,000 years. These “Reg soils” are possibly the closest analogy to the OE soil profile for several reasons: they formed (1) in a hyperarid climate, (2) on coarse alluvium, (3) under the

influence of a rainshadow effect caused by orogenic topography, (4) with sizeable eolian dust/salt influx (Amit et al., 1993; 2006); hence the temporal upper limit of 10^5 years used in the proposed hyperarid model. In contrast, however, the magnitude of hyperaridity (<3 mm/yr vs. ≤50 mm/yr precipitation) and local/regional sources of salt at OE (versus the Negev soils) is noteably higher, which enhances both distribution and accumulation of eolian dust/salt; hence the 10^2 to 10^5 year time constraint for profile 1. Future chronosequence studies on Atacama fans will provide a more constrained time estimate for this incipient profile (1) as well the others described herein.

Step 2

Continued eolian/atmospheric dust/salt influx and persistent hyperaridity fuel the next period of pedogenesis at OE (i.e. Step 2, Figure 4.1). Gravel clasts at the surface are reduced to smaller and smaller clasts via thermal (McFadden et al., 2005) and salt shattering (Watson, 1985; Amit et al., 1993; McFadden et al., 1998) processes (e.g. Figure 3.6B). This effectively increases surface litter/ particle density creating a desert pavement composed of closely packed (modified) clasts derived from the alluvial parent material below (e.g. Wells et al., 1985). Once formed this desert pavement enhances the retention of eolian dust (Yaalon and Ganor, 1973; Gile, 1975; Petersen, 1977; McFadden et al., 1992; McFadden et al., 1998), resulting in the formation of a vesicular horizon (Av) below the desert pavement (e.g. Figure 3.9A). Over time the desert pavement and Av coevolve (Gerson and Amit, 1987; McFadden et al., 1998) where the tightly packed pavement clasts are vertically elevated as the Av thickens with continuous eolian inputs of soluble minerals and silicate dust (e.g. Cooke, 1970; Yaalon and Ganor, 1973; Gile, 1975; Wells et al., 1987; Wells et al., 1995; McFadden et al., 1987; McFadden et al.,

1992; McFadden et al., 1998; Anderson et al.,2002); and subsequently smooth surface irregularities like relict bar and swale features (Figure 3.1). Two textural domains at OE highlight this process with a noteable distinction between unconsolidated surface horizons and (presently indurated) alluvial parent material below. The surficial (Avyz and Byz) horizons (Figure 3.6) are comprised of mostly clast-free silt and fine sand with generally higher clay percentages compared to indurated horizon measurements (Table 3). This is consistent with typically loamy Av horizons (McFadden et al., 1998) and exemplifies the textural dichotomy often seen in desert soils between these surficial horizons and the underlying parent materials. The Bz horizon was not given a textural designation because of its overwhelming salt content (>99%, Table 3), but is considered part of this unconsolidated domain (discussed further below). These horizons are all interpreted to be eolian dust derived and originally emplaced as a singular Av horizon upon the underlying alluvium after fan stabilization as described above and illustrated in Profile 2. The separate horizon designations are explained further in the Profile 3-4 discussions below. Desert pavement clasts atop the Avyz (Figure 3.6B) reflect identical volcanic lithologies noted in the underlying alluvium suggesting that they are synchronous to the parent material, but systematically dislodged/ modified then rafted vertically during eolian deposition and formation of surficial horizons (e.g. Wells et al., 1985). Furthermore, most researchers agree that the desert pavement is essential to initiate and accelerate the Av formation (Yaalon and Ganor, 1973; Gile, 1975; Petersen, 1977; McFadden et al., 1992; McFadden et al., 1998). Thus, the desert pavement in Step 2 (Figure 4.1) is tightly packed even though the desert pavement at OE is presently weakly interlocking (Figures 3.2 and 3.6B). This apparent inconsistency is also

addressed later in the Step 4 discussion. Concurrent with the formation and thickening of the Av, the petrosalic horizon born in Profile 1 thickens in the subsurface as soluble salts dissolved from the surface or surficial horizons continue to infilitrate the porous profile with sporadic rain events. The desert pavement and continually accreting Av cause some surface runoff/ evaporation atop the pavement and limit rain percolation to depth because of high surface areas (Shaetzl and Anderson, 2005) and/or negative matric potentials (McFadden et al., 1998) associated with the silty Av. This translates into shallower depths of wetting over time as the Av thickens, which results in accumulation of illuviated salt at increasingly shallower depths, thus thickening the petrosalic horizon. The fine soil cracks (illustrated in Step 2) that bound columnar Av peds certainly favor rapid meteoric infiltration at times (e.g. McFadden et al., 1986; 1998) implying that depths of salt precipitation will be variable and not necessarily shallower with each subsequent addition of saline water. Additionally, anomalously intense rain events (perhaps every 10^3-10^4 years) relatively unaffected by surficial horizons could flush surface/ subsurface salts much deeper and overlap or overprint previous salt accumulation (e.g. Harden et al., 1991). Anhydrite-cemented alluvium at depths of 153 to 180 cm in the Bzm2 (Tables 4 and 5, Figures 3.37B and 3.39A) provides evidence of this process as the anhydrite cement could be an older salt accumulation preserved by subsequent halite (and nitratine) induration in the Bzm2. Of course, this could also be a reflection of soil chemistry as anhydrite could have illuviated contemporaneously with halite since NaCl can increase the solubilities of gypsum/ anhydrite until it overwhelms the system (Braitsch, 1971). However, it is difficult to say which (if either) of these interpretations is correct so it is more important to note that the salt minerals (Tables 4-6)

cementing the massive horizons at OE are extremely sensitive to depth of wetting changes given their high solubilities (Table 1) and environmental sensitivity so they are readily translocated during these changes. Ultimately, stochastic salt migration via percolating meteoric water (of various magnitudes) over geologic time scales eventually coalesces Stage I-II with Stage III zones noted in Profile 1. Hence, thickening of the petrosalic horizon towards the surface until the underlying parent material is completely indurated, as illustrated in Profile 2 (Figure 4.1) and evidenced presently by the extremely salt-indurated alluvial parent material (Bzm1/ Bzm2 horizons, Figure 3.5) and elevated EC values (Table 2) at OE. Estimating the time required to form the profile illustrated in Step 2, similar to Step 1, is difficult. Some indication is inferred from the hyperarid Negev Desert as Av horizons form there in a 10^3 year time scale (Gerson and Amit,1987; Amit et al., 1993). Desert pavement and Av studies in the Mojave Desert similarly report these geologically instantaneous time spans (McFadden et al., 1998; Quade et al., 2001). Quade et al., (2001) also constrained timing of desert pavements/ Av horizons in their study via radiocarbon dates of underlying spring deposits (Quade et al., 1998), therefore this rapid minimum time is adopted in the proposed hyperarid pedogenesis model. Since these surface horizons contribute to the induration of the parent material below them, the formation of the indurated horizons at OE could have also been equally rapid. The preservation of halans/ salt pendants (Figures 3.34, 3.35A, and 3.37A) also suggests rapid cementation since these pedofeatures could have easily been dissolved and reincorporated into the Bzm2 horizon in the presence of subsequent soil water given their particularly soluble constituents. However, in the absence of chronosequence data at present within the study are an upper limit of 10^6 years is also

incorporated into the model since precipitation/ moisture events (as well as temperature/ humidity fluctuations) available to translocate salt minerals, to depths of ≥3m seen at OE, can be highly variable given the hyperarid climate in the Central Depression (Ericksen, 1981, Ewing et al., 2006). Therefore a 10^3 to 10^6 year temporal constraint is noted at this point in the proposed pedogenesis model.

Step 3

The complete induration of parent material concludes the period of pedogenesis depicted in Step 2. This signifies the inception of salt heave in the massive horizon at OE and a transition from eolian-dominated to salt heave-dominated pedogenic processes. As noted in Chapter IV, salt heave functions through salt weathering processes including: (1) dissolution/precipitation (enhanced through hydration/dehydration), and (2) thermal expansion/ contraction of salt minerals (Buck et al., 2006a; Buck et al., 2006b). However, current research indicates that process 1 is the most influencial weathering process since the transition from anhydrous to hydrous salt phases does not infer hydration but rather "through-solution hydration", where rapid dissolution/ precipitation facilitates the salt phase transition (Rodriguez-Navarro et al., 1999). The effectiveness of salt heave at OE is therefore attributed to repetitive/ persistent salt dissolution/ precipitation reactions, which exert significant crystallization pressures in the confined spaces within soil materials over time. Minerals most likely to exert the highest crystallization pressures in this study include halite, anhydrite/ gypsum, and thenardite (Winkler and Singer, 1972; Figure 5.1). For example, theoretical calculations of halite pressures suggest forces of 654 atm when it is oversaturated by a factor of 2 at 50° C (Winkler and Singer, 1972). Rodriguez-Navarro et al., (1999) also report that halite is a

more effective weathering agent at low relative humidity, which makes it a strong proponent for salt heave in the Atacama Desert, and therefore OE. Since halite is the most abundant salt mineral in indurated horizons it is considered a major contributor to salt heave at OE. Anhydrite and gypsum crystallization pressures similarly calculated are 398 and 334 atm respectively (Winkler and Singer, 1972). Although these minerals as well as the hemihydrate (bassanite) are mostly concentrated at the surface in unconsolidated horizons at OE, the presence of anhydrite in indurated zones (albeit lesser than halite overall) could over time contribute significantly to salt heave (e.g. dehydration/precipitation; Rodriguez-Navarro et al., 1999) especially since the presence of sodium chloride lowers the transition temperature of gypsum-anhydrite (Gordon and Macdonald, 1953). The transition from bassanite to gypsum can also be a rapid process (Winkler and Wilhelm, 1970) aiding salt heave over time. Similarly, the thenardite-mirabilite transition temperature is also affected in an environment saturated with sodium chloride (from 32.4° to 17.9° C, Goudie, 1977). Thenardite crystallization pressure calculations suggest forces of 345 atm when oversaturated by a factor of 2 at 50°C (Winkler and Singer, 1972). The transition of thenardite to mirabilite (or vice versa) results in a 314% volume change and can occur multiple times daily with temperature and humidity fluctuations (Winkler, 1975; Sperling and Cooke, 1980), which should certainly supplement salt heave (i.e. dehydration/precipitation; Rodriguez-Navarro et al., 1999) in confined soil materials. Similar to gypsum/bassanite/ anhydrite, thenardite mainly occurs in an unconsolidated surface horizon limiting its overall contribution to salt heave process at OE. However, its occurrence (albeit less than halite) in indurated horizons suggests some contribution over extended periods of time. Although specific

measurements of crystalline pressures for the other salts found in this study (i.e. nitratine, glauberite, eugsterite, bloedite, and darapskite) are not presented here, their respective contributions to salt heave are considered noteworthy. These minerals are also extremely soluble (Table 1) and sensitive to temperature/humidity, and therefore, should exert similar (perhaps lesser magnitude) crystallization pressures during dissolution/precipitation reactions in soil pores/cracks. Ultimately, all the salt minerals present at OE possess the ability to dissolve and precipitate frequently with temperature or relative humidity changes at the surface or at depth in pore spaces (Buck et al., 2006b). Therefore, rain events are not necessary to incite salt heave at OE or elsewhere in the hyperarid core of the Atacama Desert characterized by its infrequent and/or negligible precipitation.

Broadly estimated between 10^3 and 10^6 years of hyperarid soil formation at OE, Step 3 (Figure 4.1) models the transition to salt heave processes noted above, however eolian processes certainly persist. Dust/ salt inputs are continuous (and likely variable in intensity) which in conjunction with periodic precipitation cause differentiation of the Av horizon by long-term retention of the windblown dust/ salt. Dissolved salts translocate and reprecipitate shallowly within the Av causing horizonation. The three surface horizons (Avyz, Byz, and Bz, Figure 3.6) seen at OE confirm this process, although the snapshot in time represented by Step 3 is not correlative to the present OE profile temporally. Subsequently, horizon thicknesses, texture, salt content, and degree of accumulation are likely to be less than reported herein (Figures 3.3 and 3.4; Table 3) at the time period represented by Step 3. Salt/ clay mineralogy and pH/EC may vary as well (Table 2, 5-7). Therefore, the pedogenic specifics of these (Avyz, Byz, and Bz)

horizons are discussed with Step 4 correlation to the OE profile. For now it is more important to note that the Av is likely thickening as well as evolving with continued hyperaridity and continued dust/salt influx. As mentioned above this step, (3, Figure 4.1) is illustrated primarily to reflect a transition from eolian to salt dominated processes (Figure 5.1). Anomolous salt percentages (Table 3) and bulk density (Figure 5.2), throughout the OE soil profile and negligible soil voids (Table 4) especially in the Bzm2

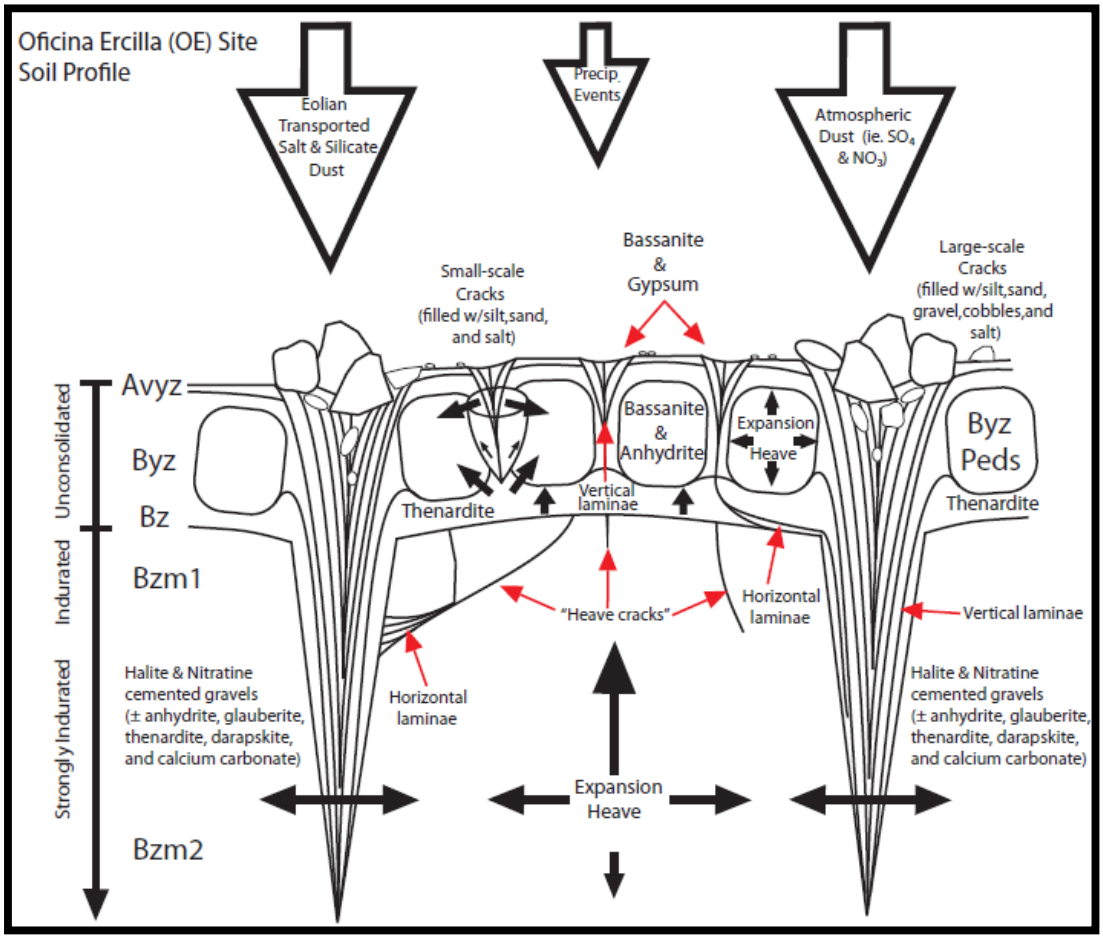

Figure 5.1. Schematic summary of salt heave model for OE noted in text.

horizon testify to the soil mass gain reported by Ewing et al. (2006). However, the soil cohesion as a function of this extreme salt induration is the focus of Step 3 and OE development at this point. The induration of the subsurface horizon(s) with salt minerals is so extreme that it responds to environmental changes (i.e. temperature/ humidity/ moisture fluctuations) collectively as a single unit. Since the massive horizon is so indurated, volumetric expansion/ contraction via salt heave processes, cannot be dispersed on an intergranular level. This results in incremental yet cumulative (irreversible) massive soil horizon distortion/ warping (Figure 5.1). After many repetitive

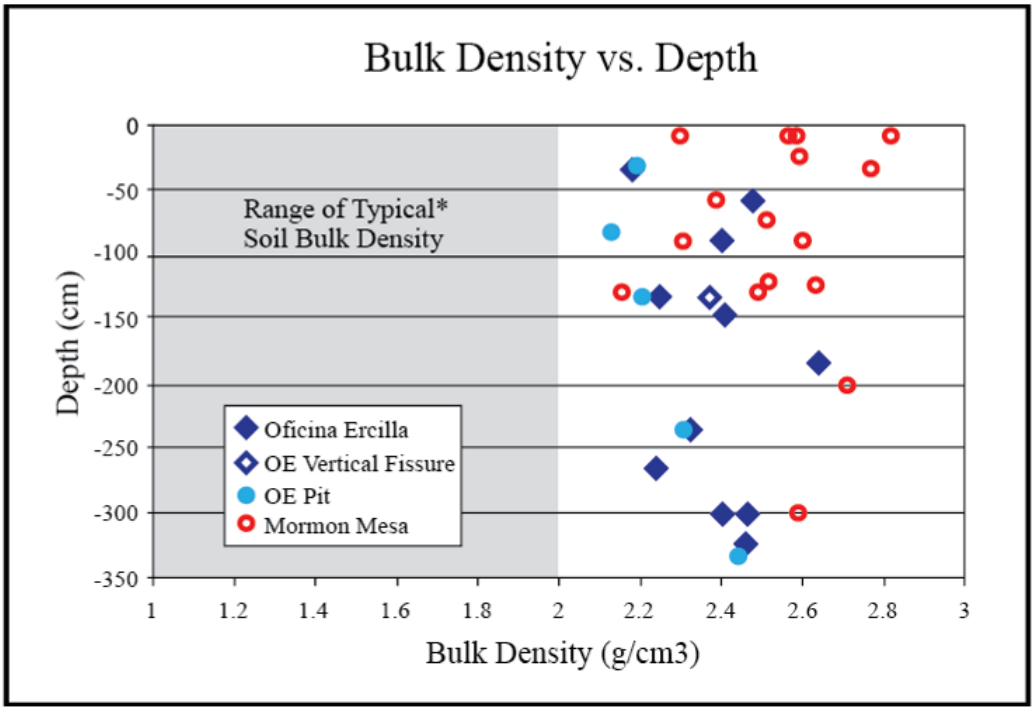

Figure 5.2. Bulk density with depth at OE (modified from Prellwitz, 2007), petrocalcic horizon data from Mormon Mesa, NV for comparison (data acquired via personal correspondence with Dr. Amy L. Brock). * Gray area indicates bulk density range of most soil orders excluding Histosols, Andisols, and Gelisols that fall below the bulk density range on the x-axis; hardpans are also not included in this gray area.

horizons are contemporaneously forced to mimick the upward deformation and eventually reflect a gently undulating surface microtopography. This surface characteristic is evident at OE presently (Figures 3.1, 3.2 and 3.42), but has also been described by other researchers at other localities in the Central Depression (Ericksen 1981; Clarke, 2006; Buck et al., 2006). With time and continuous salt heave modification the cohesive soil develops tensile stresses as a result of expansion/ contraction, which result in vertical soil cracks as illustrated in Step 3 (Figures 4.1 and 5.1) and at OE (Figures 3.4 and 3.8A-B). These vertical cracks breach the surface, disrupting surface horizons including the desert pavement atop, and eventually coordinate to define soil polygons at the surface (Figures 3.1 and 3.2). Some of these cracks may also align with the fine cracks between columnar Av peds. Cracks are topographically lower than adjacent soil polygons, so when cracks are open, sediment from surficial horizons as well as eolian dust/ salt infill the cracks by gravitational forces or with water infiltration, as seen in (Figures 3.4 and 3.8A-B) and reflected in texture/ salt content data (Table 3). These infilled cracks then enhance the next phase of upward soil warping since the cracks have been filled and subsequently cannot relieve lateral expansion forces created by salt heave (Figure 5.1). Additionally, each subsequent contraction, infill, expansion cycle leads to crack propogation deeper into this soil profile, which fuels this salt heave feedback mechanism as sediment/ dust/ salt keep getting flushed to depth and effectively incorporating deeper reaches of the soil profile. Since a profile was not viewed at the OE site to represent this profile (3) specifically, it is not known, but likely these vertical cracks would reflect many vertical laminae signifying the cycles of contraction/ infill/ expansion similar to those seen presently at OE (Figures 3.4,3.8A-B,

and 4.1). The fine cracks between Av peds would also reflect similar (albeit finer) laminae since the soil warping would also cause these cracks to open/ infill/ close concurrently (Figure 3.4, 3.6, and 4.1). Another key process illustrated here (albeit incipient at this point) is the disruption/ dismantling of the desert pavement. Fluctuations (and increasing) microtopography at the surface lead to the mobilization of pavement clasts toward surface lows (i.e. cracks), via gravitational forces or incremental creep processes attributed to microtopography fluctuations. In contrast to Quade et al., (2001) desert pavement destruction is not linked to vegetation disturbance/ climate change, but rather salt heave processes solely since vascular plants are devoid in the hyperarid core of the Atacama Desert (and OE) (Ericksen, 1981; Rech et al., 2006).

Step 4

Step 4 (Figure 4.1) is the most accurate physical depiction of the OE site presently. However, placing the OE profile at this position in the model temporally is debateable and discussed below. In the meantime this step (4, Figure 4.1) will be used as an illustrative guide to examine and interpret OE pedogenesis, and salt heave processes dominating post soil induration (Step 3) up to the present day. At this point in the model, hyperaridity, concurrent salt accumulation, and well established salt heave processes have persisted for significant geologic time spans ($>>10^6$ years). These have had a profound affect on both unconsolidated and indurated horizons. Texture, mineralogy, and eolian/ atmospheric dust sources for unconsolidated horizons correlate well with the description of the chuca layer (Figure 1.8) described by Ericksen (1981) and are considered synonomous (Figure 5.3). This study divided this unconsolidated zone (chuca) into three soil layers, but is interpreted to be a single Av horizon subsequently differentiated by

long-term retention of windblown and translocated dust/salt. This inference is based on similarities to Av horizon/ped properties documented in the Mojave Desert (McFadden et al., 1997,1998). The obvious similarity is the vesicularity of the Avyz horizon at OE (Figure 3.9A), which is a distinguishing characteristic for Av horizons worldwide (Springer, 1958; Cooke, 1970; Miller, 1971; Evenari et al., 1974; McFadden et al., 1987, 1998). Columnar peds bounded by salt/ sediment filled cracks occur throughout the Byz horizon (Figure 3.6) and are similar in size and shape to those documented in the Cima volcanic field, CA (McFadden et al., 1987, 1998). These columnar Byz peds also reflect

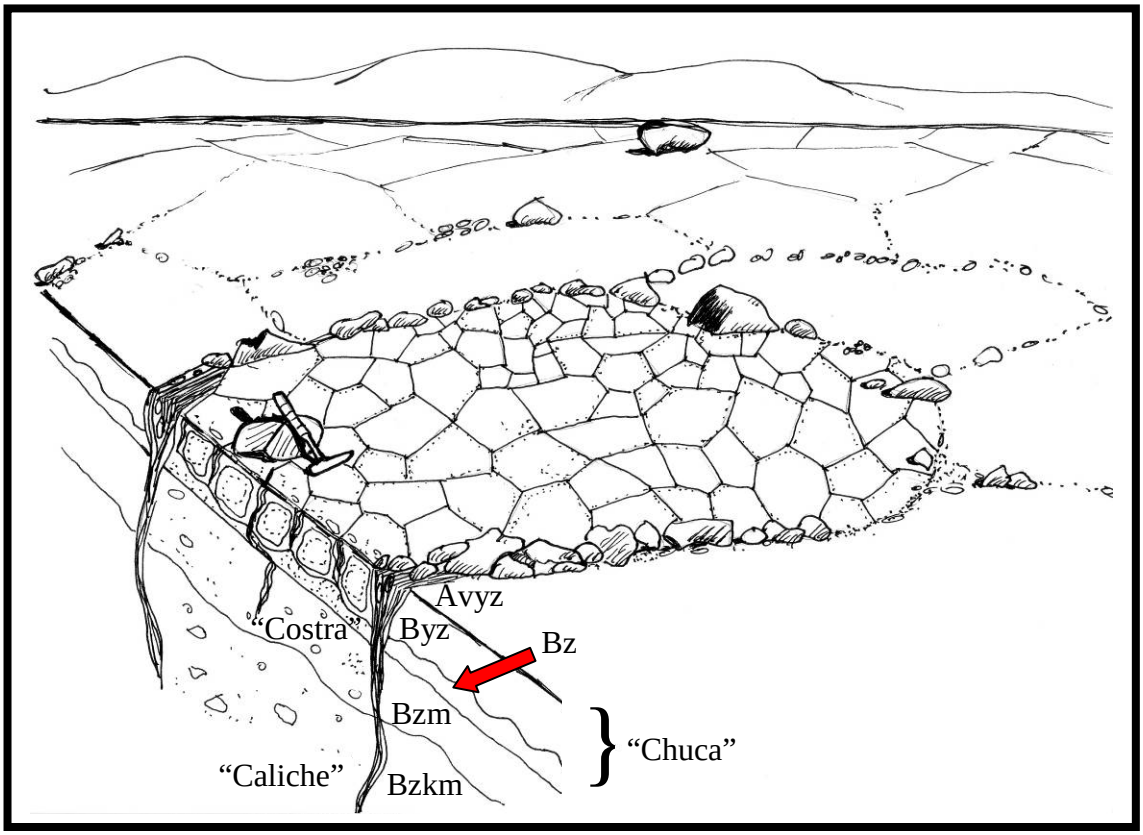

Figure 5.3. Sketch of Figure 3.2B modified to represent horizonation-soil crack relationships at OE and likely correlative layers noted in Ericksen (1981). Note: Smaller polygons only seen in the field when desert pavement and Avyz are not present, see also Figure 3.42.

an increasing concentration of gypsum/ bassanite/ anhydrite towards the center of peds (Table 6, Figure 5.1), which is similar to the calcium carbonate distribution in the less arid Mojave peds (Anderson et al., 1994; McFadden et al., 1987; 1998). This indicates that water movement in both cases is towards ped centers. Additionally, soil carbonate in the Atacama is limited (Quade et al., 2007) and precipitation is generally not chemically favored (Rech et al., 2006; Prellwitz, 2007) due to the common ion effect and the lack of organic processes (Ewing et al., 2006). Therefore, soluble salts that are typically (sometimes seasonally) flushed out of the Av (McFadden et al., 1998) are retained in the soil in this study. Gypsum/ bassanite/ anhydrite salt crystals in the Byz seen in SEM analyses exhibit mainly an anhedral/ alabastrine to subhedral lozenge-like habit (Figure 3.17). However, euhedral skeletal prismatic crystals were observed in grain-mounted salt aggregates and snowball morphologies (Figure 3.18A). Alabastrine and skeletal morphologies suggest rapid evaporation, therefore accelerated precipitation, resulting in multiple crystal nucleation (alabastrine; Watson, 1985) and an exhaustion of saline pore fluid causing incomplete crystal formation (skeletal). The lozenge-like crystals are likely degraded prismatic crystals partially-dissolved with infiltrating meteoric water (Watson, 1985). Prismatic crystals most likely dominate when saline meteoric water is adequate in the Byz since impurities such as halite and organic matter, which would favor a lenticular habit (Edinger, 1973), are limited (below XRD detection level, Table 6) or not present. The open gefuric fabric constructed by these prismatic/lozenge-shaped crystals is a reflection of salt weathering processes, but do not contribute to salt heave throughout the entire profile. Since this horizon is not indurated it is not entirely cohesive, therefore crystallization pressures of these mineralogies is mostly dispersed on an intergranular

level as displacive crystallization (Watson, 1985), hence the open gefuric fabric, exhibited by randomly oriented crystals and salt aggregates, which raft, displace, and eventually adhere soil materials (Figure 3.18B). Horizon porosity (Table 3) is likely an indirect result of this fabric since the small prismatic crystals promote a less cohesive and 'puffy' nature (e.g. Buck et al., 2008). Although clasts are sparse within the Av, displacive crystallization can also cause clast shattering (Figure 3.14) in surface horizons (e.g. Amit et al., 1993) when saline soil water infiltrates incipient clast fractures. Salts subsequently precipitate and fracture/ displace clasts, which over time may account for some volumetric fluctuation in this horizon and some displacivity surficially. The Bz (Figure 3.6) is thought to form in a similar manner to the calcium carbonate accumulating on the bottom of columnar peds noted in the Mojave (McFadden et al., 1998). In this case, the mineralogies are different, but the location of salt accumulation is the same. However, the reason for the enrichment of thenardite specifically in the Bz is somewhat uncertain. Ericksen (1981) reports that this layer is common, but mineralogy can vary between locations as gypsum, anhydrite, thenardite, bloedite, or humberstonite. This study shows that glauberite and eugsterite also occur in this horizon (Table 5, Figures 3.21-3.23). Variability of salt mineralogy by location suggests that enrichment of any specific mineral is determined by site specific criterion/criteria. At OE this is may be attributed to the dominance of Na^{+} /Ca^{2+} cations and SO_4^{2-} anions (Prellwitz, 2007), which over time results in preferential precipitation (at a solubility dependent depth) of either gypsum or thenardite invoked by the common ion effect in soil solutions supersaturated with SO_4^{2-} (e.g. Braitsch, 1971; Reheis, 1987; Buck and Van Hoesen, 2002). Salt morphology in the Bz is dominated by euhedral prismatic and acicular habits

(Figures 3.21-3.23), which also suggests that this horizon contributes to displacivity surficially (Buck et al., 2006b, 2008). Additionally, the hydration-temperature experiment performed on the Bz horizon (Figure 3.25, Table 8; also see pg. 76) shows that this horizon expands when wetted. The heat generated when the thenardite is hydrated could potentially compliment solar radiation-induced topotactic reactions, and subsequent mineralogical differentiation, (e.g. Mees and Stoops, 2003) of Ca-sulfate salts in the overlying Byz. However, since sediments are generally poor insolators this thermal effect may be negligible attributing mineralogical variation (i.e. gypsum/ bassanite/ anhydrite) mainly to long term dessication associated with the infrequent rainfall capable of infiltrating these surficial horizons.

Because the genesis of surficial (Av) horizons is dust-derived, this indicates that an unconformity exists at the boundary between the overlying unconsolidated horizons (Avyz, Byz, and Bz) and the underlying indurated soil horizons (Bzm1 and Bzm2). This hiatus is considered to be geologically negligible since the coevolving desert pavement and dust accumulation/ formation of an Av would have begun forming immediately after cessation of sedimentation (McFadden et al., 1987, 1998; Quade, 2001). However, as illustrated in the hyperarid pedogenesis model, the present Av and desert pavement at OE are not necessarily the first to form, which can in some instances, indicate a larger time disparity between surface age and profile age. The well-developed set of unconsolidated horizons (Avyz, Byz, Bz) and the enrichment of soluble salt in the Byz (Table 3) could support a significant profile age at OE (perhaps Pliocene; Prellwitz, 2007). However, it is possible that surficial horizons like these have been eroded and re-formed during the history of this geomorphic surface. Therefore these unconsolidated horizons may be

much younger than the surface boulders used to date the OE profile, which would have remained at the surface during unconsolidated horizon removal/reformation. In fact, as Step 4 illustrates and the present weakly interlocking/ missing desert pavement shows (Figure 3.6), these horizons are presently in a phase of eolian erosion since the pavement is no longer sufficient to prevent losses to wind. Additionally, Brock and Buck (2009) studied an arid soil in southern Nevada thought to be ~5 Ma and dominated by eolian processes. Yet, they found that this high geomorphic surface underwent numerous episodes of massive eolian erosion followed by re-sedimentation and soil formation during its ~5 m.y. formation. Therefore, it is likely that the OE soil has also experienced similar processes and therefore its temporal position in the proposed hyperarid pedogenesis model may correspond to Step 6 instead of Step 4.

Step 5

Indurated horizons (Bzm1 and Bzm2) in this study also exhibit profile characteristics that suggest that Av horizons are indeed transient over geologic time scales. In fact, the Bzm1 horizon specifically is interpreted to represent the subaerially exposed indurated horizon in Step 5 (Figure 4.1), thereby implying the surface horizons (Avyz, Byz, Bz) have been removed at least once. This interpretation is evidenced by field observations including: (1) prolific cracks in multiple orientations (i.e. brecciation), (2) less indurated nature compared to the underlying Bzm2, and (3) and the extremely variable thickness observed over short distances. These observations correspond well to the layer Ericksen (1981) referred to as Costra (Figure 1.8) therefore it is considered analogous to the Bzm1 (Figure 5.3). Ericksen (1981) describes the costra as a generally thin or absent, moderately to firmly cemented layer that can be similar to the underlying caliche or a

transitional material with properties of both the chuca above and the caliche below. Continued salt heaving which creates an undulating surface morphology and/or the preferential infiltration of rainfall via soil cracks, while the indurated horizon was exposed, could account for the disparity in preservation (thickness) noted by Ericksen (1981), and field observation above, as surface erosion would scour simultaneously to achieve steady state. It is also important to note here that the caliche layer described by Ericksen (1981; Figure 1.8) is also considered synonomous with the Bzm2 horizon (Figure 5.3) since the description of this extremely cemented caliche layer contains veins/ layers of nitrate-rich saline material and pebbles with halos of saline material. Both of these features are found in this study (in indurated horizons) and described as infilled halite-nitrate cracks and halans/ pendants respectively. Therefore, composite soil properties of the chuca-caliche suggested in the costra description (Ericksen, 1981) translates to Bzm1 characteristics resembling both unconsolidated horizons and the Bzm2. Laboratory analyses (mineralogical and micromorphological) provide evidence for this. Of course identical parent material and induration in the Bzm1 indicates the similarity between Bzm1 and Bzm2; and likely at one time were a single Bzm. However, clay content/ mineralogy in the Bzm1 are interpreted as strong evidence for similarities to unconsolidated surface horizons. Table 3 shows that elevated clay percentages in the Bzm1 rival those in the Avyz and Byz. This is hard to explain if the Bzm1 was never exposed because its strong induration would prevent the incorporation of silicate dust especially if the Av horizon were overlying it. Similar to the Avyz and Byz, the Bzm1 contains an analogous clay mineral assemblage of commonly illite and kaolinite, with minor amounts of smectite and chlorite (Table 7, Figures 3.13, 3.19, and 3.31). Illite and

kaolinite specifically are noteworthy, as these clay minerals have commonly been reported in the clay fractions of many arid soils (Dregne, 1976; McFadden, 1982; McFadden et al., 1986, 1998; Simonson, 1995). Illite in particular is known to enrich surface horizons of aridic soils around the globe via dust inputs and neoformation (Singer, 1988). Although the Singer (1988) hypothesis on pedogenic illite was not tested in this study, it is a possibility given substantial residence times associated with the Atacama's enduring aridic regime (Alpers and Brimhall, 1988; Rech et al.,2006) and cation (i.e. K^+) availability at the OE site (Prellwitz, 2007). However, dust-derived illite is the interpretation here inferring that the Bzm1 has been exposed to surface/ eolian processes as some point during pedogenesis of the OE profile, as well as during Step 2. Additionally, microscopic analyses reflect higher porosity (Table 4, Figure 3.27-3.29) in the Bzm1, which are likely due to salt dissolution when the underlying indurated horizon in the proposed model was exposed (Figure 4.1, Step 5) to rainfall or temperature/ humidity fluctuations at the surface, thereby resulting in a slightly less-cemented upper portion of the underlying indurated horizon.

Step 6

As the proposed model illustrates the integrity of surface horizons are ultimately influenced/ dictated by the salt heave processes occurring in the indurated horizons. The well established salt heave mechanism (from Step 3 onward) continues to propagate vertical cracks deeper into the soil profile and ultimately the alluvial parent material below. At OE these cracks extend to ~3m depth (Figures 3.4 and 3.8), but many extend beyond this viewable depth so the terminal depth is unknown. However, cracks penetrating to 18 m depths are reported regionally (Dr. J. Rech, personal

communication). This suggests that cracks not only provide a place for eolian additions to accumulate, but also "short circuit" salt illuviation by providing a direct conduit to more permeable/ non-cemented parent material. Subsequently, more parent material is incorporated effectively increasing the thickness of the indurated zone and therefore enhances salt heave with the increase of cohesive soil material. Additionally, each cycle of contraction/ infill/ expansion that promotes cracks propogation also increases the width of cracks as dust/ salt/ sediment are vertically stratified within them. This in turn provides more resistance during expansion equaling more upward warping of soil polygons, which results in destruction/ mobilization of desert pavement towards cracks (Step 4, Figure 4.1), hence patterned ground. This again means loss of unconsolidated horizons, either consumed by soil cracks or removed via eolian deflation since the pavement clasts no longer provide a protective armor.

In addition to the macroscale pedofeatures (i.e. vertical cracks/ patterned ground/ surface microtopography) that testify to the significant role salt heave plays in pedogenesis at OE, microscopic scale pedofeatures within the Bzm2 horizon and the soil cracks that fracture it also give some indication of the smaller incremental salt heave processes that ultimately facilitate the larger scale manifestations of salt heave. Anhedral to euhedral, albastrine, and massive salt forms (Table 5) indicate not only in-situ precipitation, but continual/ repetitive salt dissolution/ recrystallization (i.e. salt heave) in the Bzm2 horizon regardless of depth. SEM/EDS analyses reveal that these dynamic salts cause and preserve pedofeatures including serrated grains, shattered clasts, and (sometimes cross-cutting) soil cracks.

Parent material clasts with serrated edges were observed at approximately 153-155 cm depth in the Bzm2 horizon (Figure 3.39). Embayed and serrated grains have been studied and implicated as indicators for pressure solution in petrocalcic horizons as a result of calcite precipitation (Monger and Daugherty, 1991). Additionally, the near neutral pH values at this depth dismiss high pH induced grain dissolution (e.g. Walker, 1962; Friedman et al., 1974). Therefore it is hypothesized that the serrated grains observed at OE are similarly pressure solution features. However, precipitation of anhydrite is suggested here instead of calcite since anhydrite is the mineral present along these dissolution features. The high crystallization pressure exerted by anhydrite (Winkler and Singer, 1972) during precipitation is inferred to have the same effect on grain boundaries as would calcite in a confined soil matrix (i.e serrated grains). Therefore, as anhydrite precipitated in the confined interstitial space between grains, the indurated Bzm2 horizon provided an opposing force thereby creating compressive stresses (Robin, 1978) along the volcanic grain boundary as the anhydrite crystal(s) applied pressure on the clast during crystallization. This crystallization pressure increases the solubility of the silicate grain (Weyl, 1959; Maliva and Siever, 1988a, 1988b) resulting in dissolution.

Shattered clasts and soil cracks are common and contemporaneous throughout the Bzm2 horizon (Figures 3.44-3.48). Although, the process by which clasts are shattered in this horizon differs from salt-shattered clast(s) observed in the Byz horizon and other arid soils globally (i.e. Amit et al., 1993). The shattered clast seen in the Byz horizon (Figure 3.14) reflects cycles of salt dissolution/ precipitation near the surface, where salt has invaded and dismantled a parent material clast via pre-existing weaknesses in the clast;

similar to observations by Amit et al., 1993. However, clast shattering at depth in the Bzm2 is facilitated by salt heave via soil cracks, which indiscriminately fracture indurated soil, salt infills (Figures 3.44 and 3.45), and inevitably parent material clasts (Figure 3.46A) as they propagate through the soil profile. During salt heave contraction, open cracks are formed and later filled with eolian sediments and surface clasts. Water from subsequent rain events is preferentially transferred into these cracks because elevated centers of large soil polygons create a surface topography that directs runon into them (e.g. Figure 3.2). Water especially generates periods of salt heave in that it dissolves salts from the surface and within the sediment-filled cracks, thereby translocating them to greater depths. When they precipitate, expansion occurs, closing the cracks and heaving soil polygons upward. Therefore, salt and sediment that filled the cracks undergo compression and laminae are preserved (Figures 3.8A and 3.46). Furthermore the compressive forces from salt precipitation cause reorganization of constituents making distinct laminae of salt and sediment (Figure 3.49). Ultimately, the indurated Bzm2 horizon is so cohesive that the massive unit responds as a whole to salt heave stresses (e.g. cracking) throughout regardless of differences in grain sizes. Therefore, the cracks highlighted by salt/ sediment laminae propagate through all constituents in the Bzm2 horizon, including clasts of various sizes; hence clast shattering.

Similar to observations by Amit et al. (1993), clast shattering is not dependant on specific salt mineralogy. This is evidenced in SEM images as clasts are shattered by halite-nitratine (Figures 3.47-3.50) and anhydrite (Figure 3.51A). However, the depths (e.g. 153-292 cm) where clast shattering is occurring within the OE profile is in contrast to Amit et al. (1993). They conclude that clast shattering on hyperarid alluvial fans (in

Israel) is only facilitated near the surface because of rapid and extreme temperature/ moisture variations at ≤50 cm depth. This suggests that despite climate and solum similiarities to Atacama fan surfaces in the Central Depression, the Pleistocene and younger fan surfaces in their study have not experienced the residence time and/ or salt influx required to cross the pedogenic threshold resulting in soil cohesion. Therefore, tensile stresses via salt heave and subsequent salt cracks are not present to shatter clasts at depth. This stresses the need for more research to quantify this apparent hyperarid threshold, illustrated in the transition from Step 2 to Step 3 (Figure 4.1).

Besides their role in clast shattering, cross-cutting soil cracks observed during SEM analyses also suggest temporal relationships of salts and heaving. For example, the vertical seam of nitratine in Figure 3.44B is cross-cut by a halite-filled crack, meaning the nitratine precipitated first. But the nitratine vein is also offset horizontally suggesting that the soil was sheared laterally, possibly by halite precipitation in the larger crack to the left, or during microscale adjustments via salt heave preceding the halite filled cracks. Figure 3.45B shows a similar relationship between nitratine and halite as most of the halite filled cracks disseminate nitrate-impregnated soil matrix, suggesting nitratine precipitated first. However, the horizontal orientation of the halite-filled and epoxy-filled cracks is particularly informative of small upward heaving increments (~10 µm per crack) induced by the cracking and subsequent salt precipitation. Since the infilled cracks cannot close they signify an irreversible volumetric change towards the surface, hence salt heave. This phenomenon is echoed in Figure 3.44A, but shows an even greater upward heave since the horizontal crack (white arrow) propogating across the billet measures ~ 0.5 mm thick. Similarly in Figure 3.40 a fragment of a salt-fractured clast

and the argillan coating it are being displaced and heaved upward by halite. Although this sample is not directly correlated to a crack network, cracks in close proximity most likely provided the conduit for halite to modify this clast and clay coat (interpreted to be a pedofeature formed early in OE soil development, i.e. Step 1. It would be difficult to characterize the timing and magnitude of each of these systematic salt heave adjustments relative to the OE profile as a whole, based on these discrete snapshots. However it seems logical to suggest that their collective contribution is noteworthy throughout the OE profile. Since these microscopic cracks are prolific throughout the Bzm2, the individually small soil modifications combined translate into a composite volumetric adjustment of the indurated horizons that is considerable over geologic time scales (10^6 years).

OE Soil Profile Implications

Soil horizons and the trans-horizon cracks that disrupt them define the most fundamental profile relationships attributed to hyperarid pedogenesis at OE (Figures 4.1 and 5.3). Fine, unconsolidated surficial horizons (Avyz, Byz, and Bz) and underlying indurated gravelly horizons (Bzm1 and Bzm2) produce a distinct soil profile dichotomy. Soil cracks emphasize this division as small soil cracks only penetrate the unconsolidated horizons, which network to form small surface polygons (only visible at the surface when desert pavement/ Av are removed, Figure 3.42). Whereas the large intersecting soil cracks extend well into the indurated horizons (≥3m depth; and up to 18m regionally, Dr. J. Rech, personal communication). It is these larger cracks that eventually form the patterned ground as the clasts in the desert pavement are shifted into them (Ericksen,

1981; Buck et al., 2006). Therefore, small cracks/polygons are attributes of the Av horizon (Avyz, Byz, and Bz)(e.g. McFadden et al., 1998) modified by long term salt accumulation. Likewise, large soil cracks and patterned ground are manifestations of the indurated horizons' (Bzm1 and Bzm2) behavior also attributed to long term salt accumulation.

This division exemplifies the difference in tensile strength between the upper and lower units inherited from their provenance (i.e. soil texture), soil structure, and mineralogy. As the proposed model implies, this distinction does not indicate that these horizons form or function completely independent of each other. The self-sustaining feed back loop proves that they are pedogenically intertwined by salt heave processes and co-dependent even though their mineralogical, textural, and structural properties create juxtaposition. The hyperarid climate has just modified these properties as a result of long-term retention of eolian/atmospheric dust and limited soil losses over geologic time scales (10^5-10^6 years) (Ewing et al., 2006; Brock and Buck, 2009). Reported 120% soil mass gain due to salt additions alone, suggests that the salt fraction of the dust influx is most influential (Ewing et al., 2006). The data presented in Prellwitz (2007) suggests similar or greater gains of eolian/atmospheric solutes in the Ercilla Valley, particularly expressed at OE by abundant (sometimes overwhelming) soil horizon salt content (Tables 2 and 3) along with anomalously high bulk density measurements (Figure 5.2). Therefore, just as the arid-hyperarid transition in the Atacama defined a threshold from volumetric collapse/soil mass loss to volumetric expansion/soil mass gain (Ewing et al., 2006); the antiquity of hyperaridity defines another pedogenic threshold through saline mineral accumulation.

Extreme salt induration has provided the necessary soil cohesion to develop tensile stresses (through salt heave) in indurated horizons, which is evidenced by the large soil cracks that distinguish this profile. This connection also confirms salt heave as the catalyst for patterned ground formation as contraction/expansion processes rooted in the indurated horizons cause the undulating soil surface as well as the large soil cracks. Moreover the soil fractures are critical to continue profile evolution, as illustrated in the proposed model, making the salt heave/soil cracks/patterned ground connection inherently essential to pedogenesis. Additionally, the salt minerals/salt habits present in this study are known to incite salt heave processes often, possibly diurnally, (Buck et al., 2006, 2008), which over geologic time scales ($10^5 – 10^6$ years) accounts for the countless cumulative soil adjustments required to manipulate the soil solum and fan surface into its present state. This suggests that once salt minerals have accumulated to the point of cohesion/ induration, salt heave processes are the most important control on hyperarid pedogenesis. Therefore, salt heave is interpreted to be the dominate pedogenic process, as well as the proponent for patterned ground, occurring at OE and in similarly hyperarid soils as hypothesized by Buck et al. (2006).

Petrosalic Soil Morphology

OE and similarly hyperarid sites within the Atacama Desert provide a unique opportunity to supplement fundamental petrosalic soil morphology studies (e.g. Amit et al., 1993; Amit and Yaalon, 1996). At present diagnostic petrosalic (and petrogypsic) developmental morphology terminates at a Stage III cementation. The results presented in this study and the proposed model imply that hyperarid soils in the Central Depression

represent soil development beyond Stage III accumulation, similar to petrocalcic horizon morphology which presently consists of six cumulative developmental stages (Gile et al., 1966; Bachman and Machette,1977; Machette, 1985; Monger et al., 1991; Monger and Daugherty, 1991). Specifically, the Bz horizon (~4 cm thick) is likely analogous to a salt-enriched calcium carbonate laminar cap (>1cm) overlying a petrocalcic horizon. Except in this study the laminar cap is composed of thenardite, subsequently too soluble to retain the horizontal laminae associated with perching/ laminar flow of saline meteoric water atop the petrosalic horizon. Since the Bz exceeds a 1 cm thickness, by petrocalcic standards this elevates the OE profile to Stage 5 salt accumulation. However, exposure/ brecciation (i.e. cracks)/ recementation of the indurated horizon during Step 5 (Figure 4.1) of the proposed hyperarid pedogenesis model indicates Stage 6 morphology. Therefore, these features indicate that the OE profile is a Stage VI petrosalic horizon. These studies combined with the proposed hyperarid pedogenesis model could provide an improved temporally constrained morphological model for global hyperarid soil comparison. In the meantime, this study provides a hypothetical pedogenic model that elucidates the effects of salinization as a result of extreme aridity, which supplements desertification studies that predict increase and expansion of drylands as well as increased aridity to presently arid/hyperarid regions given the present trend in climate (Mabutt, 1985; Dregne, 1986).

CHAPTER VI

CONCLUSIONS AND FUTURE WORK

Soil Macro/Micromorphology and Salt Heave

Soil morphology using macro/microscopic techniques indicate that salt minerals are the primary contributors to dynamic soil properties at OE, confirming the dominant pedogenic process termed salt heave by Buck et al., (2006). Salt heave is a composite force consisting of (1) precipitation/dissolution (enhanced by hydration/dehydration), and (2) differential thermal expansion/contraction reactions of salt minerals, which can occur at numerous different time scales diurnally, seasonally, decadal, or geologic. Countless cycles of this composite set of processes incites cumulative volumetric changes and subsequent tensile stresses in the salt-rich soil materials. At OE, these innumerable soil modifications over millions of years have resulted in profile distortion and fracturing. Cracks have supplemented salt retention and in turn enhanced the salt heave mechanism visible in pedofeatures observed macroscopically and microscopically. Macroscopic evidence of salt heave at OE includes (1) shattered and displaced clasts near the surface or within the subsurface, (2) disruption of soil horizonation by stress fractures (vertical and/or horizontal), preserved with laminae of salt/sediment in respective orientations, (3) undulating soil surface where soil (stress) fractures serve as topographic lows that concentrate cobbles/clasts and coordinate into a polygonal network (i.e. patterned ground). SEM/petrographic analyses corroborate field evidence with microscopic

expressions of salt heave as (1) petrosalic peds marbled with salt-infilled soil fractures, (2) shattered parent material grains displaced/offset in a salt matrix, (3) alternating laminae of salt/sediment in soil cracks that disseminate petrosalic peds and parent material grains, (4) cross-cutting/offset cracks, with and without salt infill, propogating through parent material clasts and petrosalic peds, (5) and serrated/embayed parent material clasts interpreted as pressure dissolution caused by salt crystallization in confined soil spaces.

Hyperarid Pedogenesis

The current and persistent hyperarid climate within the Central Depression of the Atacama Desert has produced one of the oldest and driest extant soil profiles on the planet, Oficina Ercilla (OE). Evidence for this comes from the sizeable inventory of soluble pedogenic salt resulting from long-term ($>10^6$ years) retention of eolian/ atmospheric dust. Halite is most prevalent, however other salt minerals include: gypsum, bassanite, anhydrite, nitratine, thenardite, glauberite, eugsterite, darapskite, bloedite, and calcium carbonate. Salts are present at depths correlative to a coarse solubility trend indicating the stochastic infiltration via intermittent rain events over millions of years. Soil morphologies exhibited by these salts range from Stage I coatings/snowballs, Stage II pendants/halans/nodules, incipient Stage III peds, to most commonly Stage VI massive cementation. SEM analyses reveal that these salts frequently occur as small ($\leq 50\mu m$) subhedral to euhedral crystals indicative of in-situ growth and pedogenic origins. However, anhedral to massive (halite/nitratine/ glauberite/thenardite/calcium carbonate) and alabastrine (anhydrite) forms of are present at depth, which facilitate most of the

cementation in indurated alluvial parent material. With the exception of one tiny mass of calcium carbonate (interpreted as dust translocated via soil cracks), these are also considered to be precipitated in-situ and exhibit these crystal forms because of rapid and continuous dissolution/reprecipitation or dessication.

Mineralogical and micromorphological results presented in this study reveal that characteristically indurated Atacama soils are open and dynamic systems that evolve through a self-sustaining feedback loop because of moisture limitations and negligible/nonexistent biological activity. The hyperarid pedogenesis model proposed in this study suggests a combination of soil forming processes (e.g. eolian deposition, accumulation of soluble salts, clast shatter, and pressure solution) that are comparable to those observed in arid soils globally. However, once a threshold is reached in which salt induration with continued salt accumulation occurs, the processes of salt heave become the dominant controls on surface and soil evolution. Only significant and sustained climate change can erase these effects through dissolution of the salt, thus stopping the salt heave engine. Therefore salt heave and its resulting effects is unique to arid/ hyperarid pedogenesis.

Coevolving Av horizons/desert pavements are common to arid soils (McFadden et al., 1998), but at OE they are interpreted to signify a transient yet reoccurring pedogenic marker through the course of soil evolution. In contrast to the Mojave Desert the destruction of the Av horizon/desert pavement is not due to climate change and/or biological processes (Quade et al., 2001), given persistent hyperaridity and lack of flora in the Atacama (Rech et al., 2006). Rather dynamic pedogenic processes (i.e. salt heave), fueled by anomalously high salt content, distort and fracture the petrosalic soil over

geologic time scales. Desert pavement clasts (and certainly some Av material) are subsequently consumed by soil fractures, which leads to eolian deflation/removal of the Av horizon. This in turn enhances salt heave as additional salts are added to the subsurface horizons (the salt heave engine). Additionally, erosion of the overlying Av materials likely aids salt heave and developmental processes in soils downwind as well. Once the overlying unconsolidated materials are removed, the exposed petrosalic horizons begin to dissolve, freeing parent material clasts. Eventually, a new desert pavement is created (i.e. McFadden et al., 1998). With continued deposition of eolian dust, a new generation of Av/ desert pavement forms. Parent material clasts are liberated from aerially exposed petrosalic horizons via salt heave and meteoric water, which coordinate with continuous (likely fluctuating) eolian dust to reform a new generation of Av/desert pavement.

The repetitive construction and destruction of the Av/desert pavement presents a conundrum to profile and landform dating. Lack of datable materials available on arid alluvial surfaces is a common dilemma (Amit and Gerson, 1986) and is echoed at OE as well. Surface and profile ages on a younger, inset geomorphic surface were determined via cosmogenic ^{10}Be dating on surface boulders (Prellwitz, 2007), a current method for dating surfaces/landforms in the Atacama Desert (Amundson et al., 2005; Nishiizumi et al, 2005; Ewing et al., 2006). However, caution is suggested when applying these absolute dates to surfaces ages when soil profiles contain similar surface features attributed to salt heave (i.e. large soil fractures/patterned ground). Empirical ages for surface cobbles/ boulders ages may only represent the last of potentially many stages of Av/desert pavement development. Additionally, exceptionally large cobbles/boulders

could have survived multiple cycles of Av/desert pavement formation/destruction, but have been subject to surficial weathering (e.g. spalling) complicating modern dating techniques. Therefore, dates are inherently less than developmental age of the entire profile and geomorphic surface, thereby making interpretations of hyperarid landform ages and duration of hyperaridity inherently low. As with the OE study location, a detailed geomorphic surface map is needed to supplement the investigation, but used contemporaneously with geologic maps, soil morphology, and available cosmogenic ages to determine landform ages especially in the Atacama Desert, whose hyperarid landforms are notorious for complicating geologic mapping and relative dating techniques (Mortimer et al, 1974).

Patterned Ground

Lastly, the connection between salt heave and hyperarid pedogenesis presented herein leads to implications of paleosol and interplanetary soil processes. Perhaps the most impressive and memorable pedofeatures in the Atacama Desert are the large soil cracks and the patterned ground they define. Similar pedofeatures have been reported in polar and alpine localities globally, but are attributed to frost heave processes (Lachenbruch, 1962; Murton et al., 2000; Hall, 2002). Likewise, interpretations of paleosols with comparable pedofeatures mostly have been used to suggest paleo-frost heave and periglacial conditions (e.g. Retallack, 2001). However, as suggested by Buck et al., (2006b) and indicated by this study, salt can be just as effective in patterned ground formation if parent material is indurated with salt. Therefore, caution is imperative when interpreting vertically-stratified cracks/ polygonal fractures in the rock record since these

features can be preserved even if the salts are removed after burial (Kocurek and Hunter, 1986). Additionally, patterned ground within the Atacama (Buck et al., 2006) and dry polar regions of Antarctica (Marchant et al., 2002; Sletten et al., 2003) have been compared to those prevalent on the surface of Mars (Malin and Edgett, 2000; Seibert and Kargel, 2001). This study supplements previous research in that the results herein reflect an alternative pedogenic process applicable to paleosol interpretations on Earth and patterned ground on Mars. However, future investigation is needed to confirm this hypothesis.

APPENDIX

SOIL PROFILE DATA TABLES

TABLE 9. OE SOIL PROFILE DESCRIPTIONS BY HORIZON

Horizon	Depth (cm)	Boundary	Structure	Color	Texture	Salt Morphology
Avyz	0-2	Abrupt Wavy	Moderate, Medium, Platy/ Strong, Medium, Subangular Blocky	7.5 YR 7/3-7.5 YR 6/3	Loam	no visible salt
Byz	2-11	V.Abrupt Wavy/ Broken	Strong, Medium/Coarse, Columnar	2.5 YR 8/1-7.5 YR 5/4	Silt Loam	Stage I&II,incipient Stage III
Bz	11-15	Abrupt Wavy	Single Grain/Loose	2.5 YR 8/1	N/A, >99% salt	Stage III, when wet
Bzm1	15-38	Clear Wavy	Massive	7.5 YR 6/2-7.5 YR 7/2	Silt Loam/ Sandy Loam	Stage III-VI
Bzm2	38-318	N/A, base not observed	Massive	7.5 YR 6/2-7.5 YR 7/2	Silt Loam/ Loam/ Sandy Loam/ Loamy Sand	Stage III-VI

TABLE 10. POINT COUNT RESULTS FOR OE PROFILE BY HORIZON

Horizon	Depth	Sample ID	Parent Material*			Salt					Clay	Void	Count Total
						Halite	Nitratine	Sulfate					
			MM	V	P			Ca	Na	CaNa			
Avyz	0-2	Avyz	146†	53	69	0	0	0	0	0	0	132	400
Byz	2-11	Byz	28	143	36	0	0	121	0	0	0	72	400
Bz	11-15	ND§	ND	ND	ND	ND	ND	ND	ND	ND	ND	ND	ND
Bzm1	26-34	Bzm1	124	76	12	87	17	0	15	0	0	69	400
Bzm2	75	OE2 2B 75	125	97	2	67	4	0	0	45	0	60	400
Bzm2	80	OE2 80	133	119	5	58	0	0	31	0	0	54	400
Bzm2	153	OE3 1A 153	38	156	10	95	60	5		6	8	22	400
Bzm2	153	OE3 1B 153	0	245	15	58	68	0	2	0	2	10	400
Bzm2	153	OE3 3B 153	173	122	5	58	37	0	0	0	5	0	400
Bzm2	155	OE2 3 155	19	249	14	50	11	24	0	12	11	10	400
Bzm2	174-180	OE1 174-180	58	198	55	21	0	59	0	2	3	4	400
Bzm2	258	OE4 A 258	81	145	61	64	30	5	0	6	6	2	400
Bzm2	292	OE4 B 292	138	173	5	34	0	47	0	1	0	2	400
Bzm2	300-305	OE1 300-305	110	123	138	16	13	0	0	0	0	0	400

* (MM) = Undifferentiated soil matrix/micromass supported/cemented by salt minerals, (V)= volcanic grain, (P)= plutonic grain

† Indicates that (MM) is not cemented by salt minerals

§ Indicates no data, Bz horizon was not prepared for thin section analyses due to >99% salt content

TABLE 11. XRD CLAY MINERALOGY 2-THETA AND D-SPACING DATA FOR OE PROFILE

Horizon	Depth (cm)	Sample ID	Measurement	Treatment				
				K-25	K-350	K-550	Mg-25	Mg-EG
Avyz	0-2	OE Avyz	2 theta (Degrees)	6.3104	6.334	6.4023	6.2519	5.4705
				8.9315	8.9452	8.8862	8.8998	6.2434
				12.4702	12.5702	17.711	12.4315	8.8897
				17.8605	17.9049	26.6616	17.8537	12.4347
				18.844	18.8208	32.0354	18.7931	17.8302
				24.9866	24.9495	35.7166	24.922	18.7984
				25.2591	26.8622		26.7612	24.9588
				26.9268	31.6273		31.5315	26.7465
				31.5383	36.0269			31.4442
				33.2195	37.8113			35.9776
				36.1062				
				37.7803				
			d spacing (Angstroms)	14.00672	13.95462	13.80572	14.13753	16.15497
				9.90122	9.886	9.9516	9.93639	14.15677
				7.09831	7.04205	5.00794	7.12032	9.94763
				4.96634	4.95415	3.34358	4.96822	7.11849
				4.70932	4.71507	2.79391	4.72196	4.97474
				3.56379	3.569	2.51395	3.57287	4.72063
				3.52596	3.31906		3.33136	3.56769
				3.31124	2.82902		2.8374	3.33315
				2.83681	2.493			2.84508
				2.69699	2.37935			2.49631
				2.48771				
				2.38124				

Horizon	Depth (cm)	Sample ID	Measurement	Treatment				
				K-25	K-350	K-550	Mg-25	Mg-EG
Byz	2-11	OE Byz	2 theta (degrees)	6.2722	6.3257	6.3214	6.2789	5.5662
				8.8834	8.9671	8.848	8.9429	6.2528
				12.4243	12.5511	17.7767	12.4887	8.9095
				17.7773	17.8786	20.8822	17.8731	12.4309
				18.7747	18.8827	26.6781	18.8095	17.8
				24.9046	24.9765	27.9423	24.9865	18.8644
				26.8053	25.2352	31.9632	26.8271	24.9553
				27.8934	26.8668	35.7068	31.6622	25.1604
				31.4991	31.573		36.0641	26.8408
				35.9886	36.145		37.9052	31.4731
								36.0677
								37.8665
			d spacing (Angstroms)	14.09194	13.97271	13.98236	14.07674	15.87751
				9.9547	9.86198	9.99442	9.88855	14.13546
				7.12447	7.05276	4.98959	7.08787	9.92553
				4.9894	4.96138	4.25405	4.96288	7.12066
				4.72655	4.69975	3.34154	4.71787	4.9831
				3.57533	3.56519	3.19316	3.56379	4.70426
				3.32598	3.52924	2.80006	3.32332	3.56818
				3.19866	3.31849	2.51462	2.82599	3.53955
				2.84025	2.83377		2.49052	3.32166
				2.49557	2.48513		2.37368	2.84253
								2.49028
								2.37601

Horizon	Depth (cm)	Sample ID	Measurement	Treatment				
				K-25	K-350	K-550	Mg-25	Mg-EG
Bzm1	26-34	OE Bzm1 (Massive)	2 theta (degrees)	6.2874	6.247	6.3847	6.3686	5.2661
				7.6247	8.8809	8.8885	8.8731	8.8858
				8.8655	12.4243	17.713	12.4636	12.4162
				12.4328	17.7841	19.8739	17.8299	15.9768
				17.7824	18.7318	20.8773	18.7449	17.8869
				18.7425	20.8686	23.655	19.9406	18.8788
				19.8198	24.9819	26.6769	20.914	19.8773
				20.8991	26.7013	28.0108	25	25.0244
				22.0568	28.0176	33.2159	26.6969	26.7222
				23.6339	31.6784	35.7637	27.9691	31.5573
				24.9807	33.2124		31.5753	
				26.7101	35.8457		34.777	
				28.0299				
				31.5104				
				33.2293				
				35.8405				

Horizon	Depth (cm)	Sample ID	Measurement	Treatment				
				K-25	K-350	K-550	Mg-25	Mg-EG
Bzm1	26-34	OE Bzm1 (Massive)	d spacing (Angstroms)	14.05786	14.14869	13.84371	13.8787	16.78176
				11.59501	9.95749	9.94901	9.9662	9.95199
				9.97477	7.12443	5.00739	7.10206	7.12909
				7.11957	4.98751	4.46752	4.97481	5.54739
				4.98799	4.73726	4.25503	4.734	4.95909
				4.73459	4.25678	3.7613	4.45274	4.70071
				4.4796	3.56444	3.3417	4.24764	4.46678
				4.25063	3.33869	3.18552	3.5619	3.55849
				4.03008	3.18475	2.69727	3.33924	3.33613
				3.7646	2.82458	2.51075	3.19017	2.83515
				3.56461	2.69755		2.83357	
				3.33761	2.50519		2.57969	
				3.18339				
				2.83925				
				2.69621				
				2.50554				

Horizon	Depth (cm)	Sample ID	Measurement	Treatment				
				K-25	K-350	K-550	Mg-25	Mg-EG
Bzm1	26-34	OE Bzm1 (horizontal crack)	2 theta (degrees)	4.3245	6.2839	6.3811	6.2861	5.2496
				8.8785	8.8903	8.8543	8.899	8.9008
				12.4157	12.55	17.7212	12.4743	12.4326
				17.8429	17.8266	19.8292	17.8198	17.795
				18.6779	19.816	26.7107	18.7443	18.7889
				19.8698	25.0343	35.6789	19.8098	19.8803
				24.9808	26.7535		24.97	25.0588
				26.7128	33.2155		26.7067	26.6834
				27.9361			27.9788	31.6281
				34.9734			31.6125	33.2587
							33.2144	34.9337
							34.822	
			d spacing (Angstroms)	20.43353	14.06568	13.85152	14.06063	16.83454
				9.9602	9.94695	9.98738	9.93722	9.93522
				7.12933	7.05338	5.00508	7.09601	7.11971
				4.97121	4.97572	4.4775	4.97761	4.9845
				4.75082	4.48045	3.33753	4.73414	4.72299
				4.46845	3.55711	2.51652	4.48184	4.4661
				3.5646	3.3323		3.56611	3.55368
				3.33728	2.6973		3.33803	3.34088
				3.19386			3.18909	2.82896
				2.56565			2.83032	2.6939
							2.69739	2.56847
							2.57646	

Horizon	Depth (cm)	Sample ID	Measurement	Treatment				
				K-25	K-350	K-550	Mg-25	Mg-EG
Bzm2	75	OE2-2	2 theta (degrees)	8.8186	8.904	4.228	6.2484	5.3414
				12.4361	12.4178	6.3525	8.8675	8.922
				17.7945	17.772	8.828	12.502	12.368
				19.821	19.7991	17.7935	17.8194	17.8027
				20.8956	20.914	19.7775	18.763	18.7051
				23.6139	22.0749	22.0253	19.8278	19.7469
				25.193	23.6445	23.9418	20.9349	20.9194
				26.7059	25.0545	26.6876	23.5754	24.9471
				27.97	26.6791	27.9858	24.9721	26.7026
				34.9541	27.9726	29.5136	26.7085	27.9926
					33.2276	33.2892	28.0098	33.2298
					34.8641		34.906	34.9916
			d spacing (Angstroms)	10.02763	9.93171	20.89949	14.1456	16.54518
				7.1177	7.12814	13.91387	9.97252	9.91166
				4.98462	4.99088	10.01702	7.08036	7.15672
				4.47933	4.48424	4.9849	4.97772	4.98235
				4.25135	4.24764	4.48908	4.72945	4.74396
				3.76776	4.02682	4.03578	4.47783	4.49598
				3.53505	3.76295	3.71689	4.24345	4.24657
				3.33813	3.55428	3.34038	3.77382	3.56933
				3.19007	3.34142	3.1883	3.56582	3.33853
				2.56702	3.18978	3.02414	3.33781	3.18754
					2.69635	2.69149	3.18563	2.69618
					2.57344		2.57045	2.56435

Horizon	Depth (cm)	Sample ID	Measurement	Treatment				
				K-25	K-350	K-550	Mg-25	Mg-EG
Bzm2	153	OE3-1	2 theta (degrees)	6.2589	6.2445	6.3515	6.2738	5.4121
				8.8511	8.8305	8.8523	8.9419	8.8759
				12.4342	12.4181	17.7233	12.5204	12.4246
				17.7374	17.8014	19.8401	19.9486	19.8763
				19.8109	19.8541	22.0958	21.031	20.9328
				20.93	20.9157	23.633	22.2088	22.0924
				22.0485	22.1007	26.6911	23.7306	23.6375
				23.5748	23.6191	27.9988	24.3214	24.3092
				25.0444	25.0878	33.1699	26.7827	26.7127
				26.7299	26.6726	35.6987	28.0961	28.0086
				27.9993	28		33.2461	33.2258
				33.2121	33.1773		34.9427	
			d spacing (Angstroms)	14.12184	14.15436	13.91605	14.08831	16.32928
				9.99099	10.01415	9.98954	9.88967	9.96307
				7.1188	7.12796	5.0045	7.07	7.12427
				5.00055	4.98271	4.47508	4.45098	4.467
				4.48161	4.47194	4.02305	4.22427	4.24387
				4.24444	4.24731	3.76474	4.00284	4.02367
				4.03157	4.02217	3.33994	3.74948	3.76404
				3.7739	3.76693	3.18685	3.65973	3.66154
				3.55569	3.54964	2.7009	3.32873	3.33729
				3.33519	3.34222	2.51517	3.17604	3.18575
				3.1868	3.18672		2.69489	2.69649
				2.69757	2.70032		2.56783	

Horizon	Depth (cm)	Sample ID	Measurement	Treatment				
				K-25	K-350	K-550	Mg-25	Mg-EG
Bzm2	292	OE4 (vertical crack)	2 theta (degrees)	8.9204	4.2183	4.2644	6.3448	5.3655
				12.4787	8.8753	6.3978	8.497	8.4985
				14.0385	12.4352	8.9928	12.4358	10.6338
				17.9106	17.6541	14.1685	13.8567	12.4147
				19.8764	19.814	17.7137	18.73	13.7824
				25.0092	24.9792	18.0401	19.8771	16.0492
				26.7657	26.698	19.8324	24.9781	19.8258
				28.1262	33.274	23.967	26.6994	21.0551
				33.3341	34.6653	26.6802	28.0523	24.9841
				34.9729		27.3574	32.0385	26.7017
							34.8944	32.181
			d spacing (Angstroms)	9.91349	20.94738	20.72112	13.93087	16.47087
				7.0935	9.9638	13.8155	10.40646	10.4046
				6.30865	7.1182	9.83382	7.1179	8.31969
				4.95258	5.02396	6.25106	6.39104	7.12995
				4.46699	4.48091	5.00718	4.73772	6.42533
				3.56062	3.56482	4.91733	4.46683	5.52256
				3.3308	3.3391	4.47679	3.56498	4.47826
				3.1727	2.69269	3.71303	3.33892	4.2195
				2.68797	2.58774	3.34129	3.1809	3.56414
				2.56568		3.26009	2.79365	3.33865
							2.57127	2.78161

Horizon	Depth (cm)	Sample ID	Measurement	Treatment				
				K-25	K-350	K-550	Mg-25	Mg-EG
Bzm2	300-305	OE1 (300-305)	2 theta (degrees)	7.5674	8.8571	6.4039	6.3036	5.3185
				8.8829	12.4693	8.9299	8.6259	8.7603
				12.4208	17.6799	17.7075	12.3908	10.4756
				17.7112	19.8665	19.8849	18.7211	12.4044
				19.8452	26.7867	26.6543	19.8101	16.0794
				24.9911	34.9768	27.3607	24.9624	19.8488
				26.7209		34.8419	26.7274	26.7272
				28.0721			34.9058	34.8843
				33.2121				
				34.7857				
			d spacing (Angstroms)	11.68264	9.98419	13.80238	14.02181	16.61637
				9.95527	7.09885	9.9029	10.25122	10.09433
				7.12644	5.01668	5.00893	7.14364	8.44498
				5.00789	4.46918	4.4651	4.73996	7.13582
				4.47394	3.32824	3.34447	4.48178	5.51223
				3.56314	2.5654	3.25971	3.56718	4.47313
				3.33629		2.57503	3.33549	3.33551
				3.1787			2.57046	2.57199
				2.69757				
				2.57906				

REFERENCES

Alpers C.N. and Brimhall G.H., 1988, Middle Miocene climatic change in the Atacama Desert, Northern Chile: Evidence from supergene mineralization at La Escondita. Geol.Soc.Amer.Bull. 100, 1640-1656.

Amit R., and Gerson R., 1986, The Evolution of Holocene Reg (Gravelly) Soils in Deserts – An Example from the Dead Sea Region. Catena 13, 59-79.

Amit R., Gerson R., Yaalon D.H., 1993, Stages and Rate of the Gravel Shattering Process by Salts in Desert Reg Soils. Geoderma 57, 295-324.

Amit R., Yaalon D.H., 1996, The Micromorphology of Gypsum and Halite in Reg Soils - The Negev Desert, Israel. Earth Surface Processes and Landforms 21, 1127-1143.

Anderson K., Wells S., Graham R., 2002, Pedogenesis of Vesicular Horizons, Cima Volcanic Field, Mojave Desert, California. Soil Science Society of America Journal 66, 878-887.

Bachman G.O., Machette M.N., 1977, Calcic Soils and Calcretes in the Southwestern United States. U.S. Geological Survey Open-File Report 77-794, 163 p.

Bao H., Jenkins K.A., Khachaturyan M., and Diaz G.C., 2004, Different sulfate sources and their post-depositional migration in Atacama soils. Earth and Planetary Science Letters 224, 577-587.

Bockheim J.G., 2002, Landform and Soil Development in the McMurdo Dry Valleys, Antarctica: A Regional Synthesis. Arctic, Antarctic, and Alpine Research 34, 308-317.

Bohn H.L., McNeal B.L., and O'Connor G.A., 1979, Soil Chemistry. John Wiley & Sons, New York, NY.

Brady N.C. and Weil R.R., 2004, Elements of the Nature and Properties of Soils. Second Edition. Pearson, Prentice Hall, Upper Saddle River, New Jersey 07458.

Brock A.L., and Buck B.J., 2009, Polygenetic development of the Mormon Mesa, NV petrocalcic horizons: Importance for future application of absolute dating techniques, Catena 77, Issue 1, 65-75.

Brüggen J., 1928, La geologia de los yacimientos del slitre de Chile y las teorias que Tartan de explicar su origen, Sociedad Nacional de Mineria, Boletin Minero 40, 394-406.

Brüggen J., 1938, El salitre, Socidad Nacional de Mineria, Boletin Minero 50, 737-754.

Buck B.J., and Monger H.C., 1999, Stable isotopes and soil-geomorphology as indicators of Holocene climate change, northern Chihuahuan Desert, Journal of Arid Environments 43, 357-373.

Buck B.J., Van Hoesen J., 2002, Snowball Morphology and SEM Analysis of Pedogenic Gypsum, Southern New Mexico, USA. Journal of Arid Environments 51, 469-487.

Buck B.J., Wolff K., Merkler D.J., and McMillan N.J., 2006a, Salt Mineralogy of Las Vegas Wash, Nevada, Morphology and Subsurface Evaporation, Soil Science Society of America Journal 70, 1639-1651.

Buck B.J., Rech J., Howell M., Prellwitz J., 2006b, Salt Heave: A New Formation Process for Patterned Ground, Atacama Desert, Chile, Geological Society of America Abstracts with Programs 38, no.7, 520.

Buck B.J., King J., Etyemezian V, Morton J., Howell M., 2008, Micromorphology of Salt Crusts: Implications for Dust Emissions and Air Quality, Salton Sea, California USA, Abstracts of the 13th International Conference on Soil Micromorphology, September 11-16, Chengdu China, p.67.

Buol S.W., Hole F.D., McCracken R.W., 1997, Soil Genesis and Classification. 4th ed. Iowa State University Press, Ames.

Claridge G.G.C., Campbell I.B., 1968, Origin of nitrate deposits, Nature 217, no.5127, 428-430.

Claridge G.G.C., Campbell I.B., 1981, A Comparison between Hot and Cold Desert Soils and Soil Processes. Dan H. Yaalon (Ed.): Aridic Soils and Geomorphic Processes, Catena Supplement 1, 1-28.

Connor J.J. and Shacklette H.T., 1975, Background geochemistry of some rocks, soils, Plants, and vegetables in the conterminous United States, U.S. Geological Survey Professional Paper 574-F, 168 p.

Cooke R.U., 1970, Stone Pavements in Deserts. Annals of the Association of American Geographers 60, 560-577.

Darwin C., 1890, Journal of researches into the natural history and geolog of the Countries visited during the voyage around the world of H.M.S. “Beagle”, New York, D. Appleton, 551 p.

de Kalb C., 1916, Origin of nitrate, Mining and Scientific Press 112, 663-664.

Dregne H.E., 1986, Desertification of Arid Lands. Physics of Desertification, ed. F. El-Baz and M.H.A. Hassan. Dordrecht, The Netherlands: Martinus, Nijhoff.

Dunai T.J., Gonzalez Lopez G.A., Juez-Larre J., 2005, Oligocene-Miocene Age of Aridity in the Atacama Desert revealed by Exposure Dating of Erosion-sensitive Lanforms. Geology 33, 321-324.

Edinger, S.E., 1973, An investigation of the factors which affect the size and growth rates of the habit faces of gypsum: Journal of Crystal Growth, v.18, p. 217-224.

Ericksen G.E., 1961, Rhyolite tuff, a source of the salts of northern Chile, U.S. Geological Survey Professional Paper 424-C, C224-225.

Ericksen G.E., 1963, Geology of the salt deposits and the salt industry of northern Chile, U.S. Geological Survey open file report, 164 p.

Ericksen G.E., 1975, Origin of the Chilean nitrate deposits, Geological Society of America Abstracts with Programs 7, no.7, 1068.

Ericksen G.E., 1979, Origin of the nitrate deposits of northern Chile, Congreso Geologico Chileno, 2d, Arica, 1979, Actas 2, C181-205.

Ericksen G.E., 1981, Geology and Origin of the Chilean Nitrate Deposits. Geological Survey Professional Paper 1188, U.S. Government Printing Office, Washington DC.

Ericksen G.E., 1983, The Chilean Nitrate Deposits. American Scientist 71, no 4, 366-374.

Eswaran H., Zi-Tong G., 1991, Properties, Genesis, Classification, and Distribution of Soils with Gypsum. In: Nettleton W.D. (Ed.), Occurrence, Characteristics, and Genesis of Carbonate, Gypsum, and Silica Accumulations in Soils, SSSA Special Publication 26, 89-119.

Evenari M., Yaalon D.H., Gatterman V., 1974, Note on soils with vesicular structure in Deserts. Zeischrift für Geomorphologie 18, 162-172.

Flagg J.W., 1874, Nitrate of soda, its locality, mode of occurrence and methods of extraction, American Chemist 4, 403-408.

Forbes D., 1861, On the geology of Bolivia and southern Peru, Geological Society of London Quarterly Journal 17, 7-62.

Foth H.D., and Ellis B.G., 1988, Soil Fertility. John Wiley & Sons, New York, NY.

Gabelman J.W., 1995, Localization of Ore Districts by Segmentation of the North Chilean Andes. Geology and Ore Deposits of the American Cordillera; Symposium Proceedings, Geological Society of Nevada, Reno, NV.

Gale H.S., 1912, Nitrate deposits, U.S. Geological Survey Bulletin 523, 36p.

Gale H.S., 1917, Origin of nitrates in cliffs and ledges, Mining and Scientific Press 115, 676-678.

Gautier A., 1894, Sur un gisement de phosphates de chaux et d'alumine contenant des especes rares ou nouvelles et sur la genese des phosphates et niters naturels, Annales des Mines 5, ser.9, 5-53.

Gile L.H., Peterson F.F., Grossman R.B., 1966, Morphological and Genetic Sequences of Carbonate Accumulation. Soil Science 101, 347-360.

Gile L.H., 1975, Holocene Soils and Soil-geomorphic Relations in an Arid Region of Southern New Mexico. Quaternary Research 5, 321-360.

Harden J.W., Taylor E.M., McFadden L.D., Reheis M.C., 1991, Calcic, Gypsic, and Siliceous Soil Chronosequences in Arid and Semiarid Environments. In: Nettleton W.D. (Ed.), Occurrence, Characteristics, and Genesis of Carbonate, Gypsum, and Silica Accumulations in Soils, SSSA Special Publication 26, 1-16.

Harris N., 2003, Atlas of the World's Deserts. Fitzroy Dearborn Publishing, New York 192 p.

Harris, W. and White, G.N., 2008, X-ray diffraction techniques for soil mineral identification. In: A.L. Ulery and L.R. Drees (eds.) Methods of Soil Analysis, Part 5-Mineralogical Methods. Soil Sci. Soc. Am., Inc., Madison, WI, pp. 81-115.

Hartley, A.J., Chong, G., Houston, J., Mather, A.E., 2005, 150 million years of climatic stability; evidence from the Atacama Desert, northern Chile. Journal of the Geologic Society of London 162, Part 3, 421-424.

Hawker H.W., 1927, A Study of the Soils of Hildago County, Texas, and the Stages of their Soil Lime Accumulation. Soil Science 23, 475-485.

Hofseth B., 1931, Origin of Chilean nitrate, Engineering and Mining Journal 131, 468.

Holmgren G.S., Juve R.L., Geschwender R.C., 1977, A mechanically controlled variable rate leaching device. Soil Science Society of America Journal, 41, p. 1207-1208.

Knoche W., 1930, Zur Entstehung des Chile-Salpeters, Forschungen und Fortschritte 6, 196-197.

Knoche W., 1939, Una nota sobre la formacion del salitre chileno, Sociedad Cientifica Argentina Anales 127, no.5, 375-376.

Krauskopf K.B., 1967, Introduction to geochemistry, New York, MacGraw-Hill, 721 p.

Lide D.R., 2008, Physical Constants of Inorganic Compounds. In CRC Handbook of Chemistry and Physics, 88th Edition (Internet Version 2008), David R. Lide, ed., CRC Press/Taylor and Francis, Boca Raton, FL.

McFadden L.D., Wells S.G., Jercinovich M.J., 1987, Influences of Eolian and Pedogenic Processes on the Origin and Evolution of Desert Pavements. Geology 15, 504-508.

McFadden L.D., Wells S.G., Brown W.J., Enzel Y., 1992, Soil Genesis on Beach Ridges of Pluvial Lake Mojave: Implications for Holocene Lacustrine and Eolian Events in the Mojave Desert, Southern California. Catena 19, 77-97.

McFadden L.D., McDonald E.V., Wells S.G., Anderson K., Quade J., Forman S.L., 1998, The Vesicular Layer and Carbonate Collars of Desert Soils and Pavements: Formation, Age and Relation to Climate Change. Geomorphology 24, 101-145.

McKay C.P, Friedmann E.I., Gomez-Silva B., Caceres-Villa-nueva L., Andersen D.T., Landheim, R., 2003, Temperature and Moisture Conditions for Life in the Extreme Arid Region of the Atacama Desert: Four Years of Observations Including the El Nino of 1997-1998. Astrobiology 3, 393-406.

McLean E.O., 1982, Soil pH and lime requirement. p. 199-224. In A.L. Page, R.H. Miller, and D.R. Keeney (eds.) Methods of soil analysis. Part 2. Chemical and microbiological properties. 2nd ed. Agron. Monogr. 9. ASA and SSSA, Madison, WI.

Meunier A. and Velde B. (2004) Illite: Origins, Evolution and Metamorphism. Springer-Verlag, Berlin, Heidelberg, New York.

Michalski G., Böhlke J.K., Thiemens M., 2004, Long Term Atmospheric Deposition as the Source of Nitrate and other Salts in the Atacama Desert, Chile: New Evidence from Mass-independent Oxygen Isotopic Compositions. Geochimica Et Cosmochimica Acta 68, 4023-4038.

Middleton N. and Thomas D., 1997, Atlas of Desertification. John Wiley Publishing, London; New York: Arnold; New York 182 p.

Monger H.C., Daugherty L.A., 1991, Pressure Solution; Possible Mechanism for Silicate Grain Dissolution in a Petrocalcic Horizon. Soil Science Society of America Journal 55, no.6, 1625-1629.

Monger H.C., Daugherty L.A., Lindemann W.C., Liddell C.M., 1991, Microbial Precipitation of Pedogenic Calcite. Geology 19, 997-1000.

Mueller G., 1960, The theory of formation of north Chilean nitrate deposits through "capillary concentration", International Geological Congress, 21st, Copenhagen, 1960, Report, pt.1, 76-86.

Mueller G., 1968, Genetic histories of nitrate deposits from Antarctica and Chile, Nature 219, no.5159, 1131-1134.

Müntz C.A., 1887, Origen de los depositos del nitrato de soda, Sociedad Nacional de Mineria Boletin 4, 719-720 and 727-728.

Müntz C.A., and Marcano V., 1885, Sur la formation des terres nitrees dans les regions tropicales, Academie des Sciences Comptes Rendus 101, 65-68.

Newton W., 1896, The origin of nitrate in Chile, Geological Magazine 3, decade 4, 339-342.

Noellner C.N., 1867, Ueber die Entstehung der Salpeter und Boraxlager in Peru, Journal für praktische Chemie 102, 459-464.

Orris G.J., 2005, Naturally Occurring Perchlorate (and Other Oxyanions) in the Hydrologic Cycle – Origins, Accumulation, Transformations, and Transport. Geologic Society of America Abstracts with Programs 37, no. 7, p. 321.

Ochsenius C., 1887-88, La formacion del nitrato sodico de sales de aguas madres, Socidad Nacional de Mineria Boletin 4, no.94, 752-753.

Ochsenius C., 1888, Einige Angaben über die Natronsalpeter-Lager landeinwärts von Taltal in der Chilenischen Provinz Atacama, Deutche geologische Gessellschaft Zeitschrift 40, 153-165.

Padilla Garza R.A.,Titley S.R., Pimentel B.F., 2001, Geology of the Escondida Porphyry Copper Deposit, Antofagasta Region, Chile. Economic Geology 96, 307-324.

Penrose R.A.F., Jr., 1910, The nitrate deposits of Chile, Journal of Geology 18, no.1, 1-32.

Pissis A., 1878, report upon the Desert of Atacama, its geology and mineral products, in Nitrate and guano deposits in the Desert of Atacama, London, Taylor and Francis, 1-30.

Plagemann A., 1897-1898, Sobre la formacion geologica del salitre bajo el punto de vista De la fermentacion quimica, Sociedad Nacional de Mineria Boletin 9, ser.3, 88-93, 153-156, 245-248, 323-326, 409-412, and 583-589.

Plummer L.N., Böhlke J.K., Doughten M.W., 2006, Perchlorate in Pleistocene and Holocene Groundwater in North-Central New Mexico, Environmental Science and Technology 40, 1757-1763.

Prellwitz J.S., 2007, A Characterization of Hyper-Arid Nitrate Soils in the Baquedano Valley of the Atacama Desert, Northern Chile (MS Thesis): Miami University 56p.

Rajagopalan S., Anderson T.A., Fahlquist L., Rainwater K.A., Ridley M., and Jackson W.A., 2006, Widespread Presence of Naturally Occurring Perchlorate in High Plains of Texas and New Mexico, Environmental Science and Technology 40, 3156-3162.

Ramos V.A., 1988, The birth of southern South America. American Scientist 77, 444-450.

Rankama K.K., and Sahama T.G., 1950, Geochemistry, Chicago, University of Chicago Press, 912 p.

Rech J.A., Quade J., and Hart W.S., 2003, Isotopic evidence for the source of Ca and S in soil Gypsum, anhydrite and calcite in the Atacama Desert, Chile. Geochim.Cosmochim.Acta 67, 575-586.

Rech J.A., Currie B.S., Michalski G., Cowan A.M., 2006, Neogene climate change and Uplift in the Atacama Desert, Chile. Geology 34, no.9, 761-764.

Rhoades J.D., 1982, Soluble salts. p.167-179. In A.L. Page, R.H. Miller, and D.R. Keeney (eds.) Methods of soil analysis. Part 2. Chemical and microbiological properties. 2nd ed. Agron. Monogr. 9. ASA and SSSA Madison, WI.

Schoeneberger P.J., Wysocki D.A., Benham E.C., Broderson W.D., editors, 2002, Field Book for Describing and Sampling Soils. Version 2.0. Natural Resources Conservation Service, USDA, National Soil Survey Center, Lincoln, NE.

Sieveking J.P., 1887, Chilean nitre-beds, in Nitrate and guano deposits in the Desert of Atacama, London, Taylor and Francis, 38-43.

Sillitoe R.H., and McKee E.H., 1996, Age of Supergene Oxidation and Enrichment in the Chilean Porphyry copper province. Economic Geology 91, 164-179.

Singewald J.T., Jr., and Miller B.L., 1916, The genesis of the Chilean nitrate deposits, Economic Geology 11, no.2, 103-114.

Sletten R.S., Hallet B., Fletcher R.C., 2003, Resurfacing Time of Terrestrial Surfaces by the Formation and Maturation of Polygonal Patterned Ground. Journal of Geophysical Research 108, E4, 10 pp.

Soil Survey Staff, 1999, Soil Taxonomy: A basic system of soil classification for making and interpreting soil surveys. USDA-NRCS Agricultural Handbook 436. 2nd ed. U.S. Government Printing Office, Washington, DC.

Soil Survey Staff, 2004, Soil Survey Laboratory Methods Manual, No. 42, v.4.0. USDA-Natural Resoruces Conservation Service, Lincoln, NE.

Soil Survey Staff, 2006, Keys to Soil Taxonomy, 10th ed. USDA-Natural Resources Conservation Service, Washington, DC.

Springer M.E., 1958, Desert Pavements and Vesicular Layers of some Soils of the Deserts of the Lahonton Basin, Nevada. Soil Science of America, Proceedings 22, 63-66.

Steinmann G., 1925, über den Chemismus in der Wüste, Naturhistorischer Verein der Preussischen Rheinlande Sitzungsberichte, 1924a, 8-12.

Sundt L., 1904, Los ajentes atmosfericos I su obra en el desierto de Atacama, Sociedad Nacional de Mineria Boletin 16, no.83, 577-578.

U.S. Salinity Laboratory Staff, 1954, L.A. Richards (ed.) Diagnosis and improvement of saline and alkali soils. 160 p. USDA handbook 60. U.S. Government Print Office, Washington, DC.

Wells S.G., McFadden L.D., Dohrenwend J.C., 1987, Influence of Late Quaternary Climatic Change on Geomorphic and Pedogenic Processes on a Desert Piedmont, Eastern Mohave Desert, California. Quaternary Research 27, 130-146.

Wells S.G., McFadden L.D., Poths J., Olinger C.T., 1995, Cosmogenic He surface-Exposure Dating of Stone Pavements: Implications for Landscape Evolution In Deserts. Geology 23, 613-616.

Wetzel W., 1924, Petrographische Untesuchungen an chilenischen Salpetergesteinen, Zeitschrift für praktische Geologie, Jahrg. 32, 113-120 and 132-142.

Whitehead W.L., 1920, The Chilean nitrate deposits, Economic Geology 15, 187-224.

Winter J.D., 2001, An Introduction to Igneous and Metamorphic Petrology. Prentice Hall, Upper Saddle River, New Jersey 07458.

Yaalon D.H., Ganor E., 1973, The Influence of Dust on Soils in the Quaternary. Soil Science 116, 146-155.

VITA

Graduate College
University of Nevada, Las Vegas

Michael S. Howell

Address:
13711 Kingston River Ln.
Houston, TX 77044

Degrees:
Bachelor of Science, Geology, 2004
Old Dominion University

Master of Science, Geoscience, 2009
University of Nevada, Las Vegas

Special Honors and Awards:
UNLV Graduate and Professional Student Asssocitation Travel Grant, Fall 2005, Spring 2006
Bernada E. French Fund Scholarship, Spring 2006, Spring 2008
James F. Adams Scholarship, Spring 2007
Geological Society of America, Graduate Research Grant, Spring 2007
American Association of Petroleum Geologists, Grant-in-Aid, Spring 2007
Inducted into Phi Kappa Phi, Spring 2007

Publications:
Robins, C., Howell, M., Drohan, P., 2005, High-Intensity Fire Effects on Mineralogy and Pedogenesis of Piñon-Juniper Woodland Soils, Mesa Verde National Park, Co., *Soil Science Society of America Annual Meeting, Abstracts with Programs,* Salt Lake City, UT.

Howell, M., Buck, B.J., Rech, J., Brock, A., Prellwitz, J., 2006, Genesis of the Hyperarid Soils of the Atacama Desert: Analogue for Mars?, *18th World Congress of Soil Science, Abstracts with Programs,* Philadelphia, PA.

Buck, B.J., Rech, J., Howell, M., Prellwitz, J., and Brock A.L., 2006, A New Formation Process for Patterned Ground, Atacama Desert, Chile, *Geological Society of America Abstracts with Programs, v. 38, no.7,* p.520.

Robins, C.R., Buck, B.J., Williams, A.J., Morton, J.L., House, P.K., Howell, M.S., Yonovitz, M.L., 2008, Comparison of Flood Hazard Assessments on Desert Piedmonts and Playas: A Case Study in Ivanpah Valley, Nevada, *Geomorphology*, doi: 10.1016/j.geomorph.2008.07.020.

Buck B.J., King J., Etyemezian V, Morton J., Howell M., 2008, Micromorphology of Salt Crusts: Implications for Dust Emissions and Air Quality, Salton Sea, California USA, *Abstracts of the 13th International Conference on Soil Micromorphology*, September 11-16, Chengdu China, p.67.

Thesis Title:

Mineralogy and Micromorphology of an Atacama Desert Soil, Chile: A Model for Hyperarid Pedogenesis

Thesis Examination Committee:

Chairperson, Dr. Brenda J. Buck, Ph.D.
Committee Member, Dr. Debbie Soukup, Ph.D.
Committee Member, Dr. Henry Sun, Ph.D.
Graduate Faculty Representative, Dr. Brian P. Hedlund, Ph.D.